MICROFLUIDIC CONTINUOUS-FLOW MANIPULATION OF PARTICLES AND CELLS INSIDE FERROFLUIDS

by

TAOTAO ZHU

(Under the Direction of Prof. Leidong Mao & Prof. Jason Locklin)

ABSTRACT

Current technologies for cell enrichment such as fluorescence-activated cell sorting are often labor-intensive and require labeling step to identify cells of interests. Microfluidic sorting techniques based on intrinsic physical properties of cells were exploited for their advantages of portability and low cost. We developed a novel label-free method for continuous sorting of microparticles and cells based on their size difference. The associated devices are inexpensive and simple, only requiring a micro-channel and hand-held permanent magnets. Non-magnetic microparticles and commercial ferrofluids were first used to demonstrate the feasibility of the technology, including particles focusing and sorting. It was then optimized for bacteria and yeast cell separation with increased reproducibility, reduced screening time, and improved screening throughput and accuracy. The ultimate application of the proposed technology relies on the synthesis of biocompatible ferrofluids that meet the stringent requirements of the mammalian cell manipulation. Therefore, a polyethylene glycol (PEG) copolymer stabilized ferrofluid was developed to facilitate the mammlian cell manipulation and enrichment. We characterized the ferrofluids and confirmed the inert influence on the

mammalian cells properties, such as the viability of HeLa cells and mouse red blood cells. Then we demonstrated the separation of these two cell types with high efficiency and throughput. Label free cell manipulation inside biocompatible magnetic medium promised new applications in dealing with other types of cells. Furthermore, we combined positive and negative magnetophoresis to separate particles of different magnetic properties in both commercial and custom-made ferrofluids. Its success extends the capability of the ferrohydrodynamic platform for future development.

INDEX WORDS: microfluidics; lab-on-a-chip; ferrofluids; cell sorting; cervical cancer cell; negative magnetophoresis

MICROFLUIDIC CONTINUOUS-FLOW MANIPULATION OF PARTICLES AND CELLS INSIDE FERROFLUIDS

by

TAOTAO ZHU

BS, Nanjing Forestry University, China, 2006

MS, Nanjing University, China, 2009

A Dissertation Submitted to the Graduate Faculty of the University of Georgia in Partial Fulfillment of the Requirements for the Degree

DOCOTOR OF PHILOSOPHY

ATHENS, GEORGIA

2013

MICROFLUIDIC CONTINUOUS-FLOW MANIPULATION OF PARTICLES AND CELLS INSIDE FERROFLUIDS

by

TAOTAO

Major Professor:	Leidong Mao
Co-Major Professor:	Jason Locklin
Committee:	Richard Dluhy
	Mark Eiteman
	Jin Xie

Electronic Version Approved:

Maureen Grasso
Dean of the Graduate School
The University of Georgia
December 2013

DEDICATION

To my parents Yongxiang Zhu and Shiying Zhang

To my beloved wife, Lixin Wang

To my first born son

To my grandparents, Yongxing Zhu and Zhenxin Liu

ACKNOWLEDGEMENTS

This dissertation was only possible with the help and support of my advisor, committee members and coworkers, as well as my family and friends, to only some of whom it is possible to give particular mention here.

First and foremost, I would like to thank my advisor, Dr. Leidong Mao for his invaluable guidance and financial support over the years. He is one of the most intelligent people I have ever met and his countless insights have helped make this research successful. I deeply appreciate his advice and help on my professional life.

I am forever indebted to my co-advisor Dr. Jason Locklin for everything he has done for me from the graduate school enrollment to constant encouragement and support. I am grateful to Professor Mark Eiteman for serving on my thesis committee and providing great resources for my projects. I would also like to thank Professor Richard Dluhy for his sharp insights into the research proposals and kind career advice. I am lucky to have Professor Jin Xie's help on solving one of the most difficult problems in this work.

I appreciate the collaborators' research groups for their willingness to help and significant contribution in my research endeavors and publications. A special thank you goes to Dr. Troy Querec and Dr. Elizabeth Unger from Centers for Diseases Control. It wouldn't be possible to reach the goal without their good advice, support and feedback.

I am thankful for all the Professors and fellow members in NanoSEC that were always there to provide support and constructive criticism. I would like to thank Rui

Cheng, Zhaojie Deng, Gareth Sheppard, Evan White, Sara Orski, Joe Grubbs, Chunyuan Song, Guojun Cheng, Lina Wang, Yinzhi Lai and Yen-Jun Chuang for all the stimulating conversations and eagerness to share their intellect and friendship.

I want to thank my parents for their endless caring and love. A huge thank you to my wife Lixin Wang for keeping me up in life.

TABLE OF CONTENTS

Page

LIST OF FIGURES

Page

CHAPTER 1

INTRODUCTION

1.1. Background

Microfluidic particle separation has drawn a lot of attentions recently, mainly because of its potential diagnostic and therapeutic applications such as in cancer diagnosis [1, 2], blood cleansing [3, 4], pathogen detection [5, 6], and so on. A range of techniques have been developed to manipulate particles based on their intrinsic physical properties (e.g., size, shape, density, compressibility, polarizability) in microfluidic devices, as detailed in three excellent reviews by Pamme [7], Tsutsui *et al* [8], and Gossett *et al* [9]. These label-free microfluidic techniques are sometimes preferred over conventional ones such as fluorescence-activated cell sorter (FACS) [10] and magnetic-activated cell sorter (MACS) [11] because microfluidic techniques are cost-effective, require little user training for operation, and do not rely on the fluorescent or magnetic labels [9, 12].

Among label-free techniques, those based on channel design (e.g., pinched flow fractionation [13] and hydrodynamic filtration [14]) and deterministic lateral displacement [15, 16] combine laminar flows with microchannel geometries or micropost array to direct particles of different sizes into separate flow streamlines. Deterministic hydrodynamics separation is capable of separating sub-micron particles as well as DNA molecules with 10 nm resolutions [15, 16]. Continuous inertial separation of particles, recently reviewed by Di Carlo *et al.* [17], uses balance between inertial lift force and Dean drag forces in curved microchannel for size-dependent separation of particles and cells. The dimensions of the

channels and obstacles have implications for the applicable separation size range, and a significant amount of fine-tuning is often necessary for the separation of small particles.

In addition to these schemes, researchers are also interested in particle manipulation and sorting using external energy inputs. For example, techniques based on acoustophoresis can separate particles and cells according to their size, density, as well as compressibility at very high throughput [18, 19]. Particles and biological cells can be manipulated with acoustic forces generated from ultrasonic waves. Such waves are typically generated with piezoelectric transducers which increase the complexity and cost of the fabrication process. Dielectrophoretic force (DEP), arising from interactions of a cell's induced dipole and its surrounding spatial gradient of electrical field [20] has potential to realize low-cost and integrated devices for high-throughput manipulation of cells. However, its performance usually depends on the electrical properties of the specific liquid medium, particle shape, and its effective dielectric constant. The alternating electric fields may polarize the cell membranes and lead to cell death. The optical tweezer technique employs the forces exerted by a focused laser beam to manipulate nano- to micro-scale objects [21]. This method is usually applied to move and trap a single object. The heating due to the focused laser beam can potentially damage living systems. Magnetophoresis uses functionalized magnetic beads to label and separate target particles and cells [22-24] except in the cases of manipulation of red blood cells and magnetotactic bacteria, both of which are paramagnetic by themselves [25-28]. However, most applications of magnetophoresis use functionalized magnetic beads for labeling [23, 29, 30]. The label-based methods are manually intensive and time-consuming. The magnetic moments of these beads, even from the same batch, can vary dramatically due to their

manufacturing procedure, making scaling of the method difficult [31-35]. There is also the difficulty of removing the magnetic labels from the target particles or cells prior to further analysis. Automation-assisted cytology, where computer algorithms identify potential abnormal cells for review by a cytologist, is no better or even less sensitive than manual reading [36-38].

1.2. Goals

In an attempt to address some of the aforementioned limitations, we aimed to develop a microfluidic platform to magnetically manipulate and enrich particles and cells inside ferrofluids in a label-free manner. The success of this platform depends on the following two areas (1) to develop ferrofluidic microchips as both a general cell manipulation platform and a fast and low-cost front-end separation method for increased reproducibility, reduced screening time, and improved screening accuracy; (2) to develop a biocompatible ferrofluid with non-toxic magnetic materials, neutral *p*H (~7.4), isotonicity, as well as proper surfactant molecules for live cell manipulation and enrichment.

The platform can be applied in areas in cell biology where understanding of cell behavior requires isolation and manipulation of certain cell subpopulations. It uses magnetic force instead of electric force for enrichment, eliminating potential cell membrane polarization and breakdown. It does not produce significant heating. Chip fabrication and operation are simple and low-cost, compared to flow cytometry, rendering it attractive for future distribution.

Goals of this project are (1) to manipulate non-magnetic polymers, for example polystyrene particles for calibration and testing in microfluidic system. (2) to manipulate

live bacteria and yeast cells for pathogen detection. (3) to enrich abnormal cervical cells from other cellular constituents. It supports the effort for better prevention and control of cervical cancer, which is the second most common cancer in women globally.

1.3. Overview of the Dissertation

Chapter 2 presents the theoretical background of non-magnetic microparticles transportation inside ferrofluids in a microfluidic system. We use analytical solution to model our particle manipulation system and to simulate the magnetic fields in the channel generated by a permanent magnet.

Chapter 3 presents our experimental results on microfluidic manipulation of non-magnetic particles inside ferrofluids. Focusing particles into a narrow stream is usually a critical step prior to counting, detecting and sorting. In this chapter we show particle focusing in a single straight channel by fine tuning the flow rates and particle sizes. Then we compare the experimental results with simulation.

Chapter 4 presents the continuous separation of non-magnetic microparticles inside ferrofluids. We integrate particle separation, collection and distribution analysis processes, demonstrating high throughput binary separation of microparticles.

Chapter 5 presents the biological application of ferrofluidic manipulation techniques for bacteria and yeast separation. Biocompatibility of ferrofluids is tested for these two cell types at first. Then we demonstrate the separation of live yeast from bacteria cells based on the size difference.

Chapter 6 presents the microfluidic platform separating live mouse red blood cells from HeLa cells. Biocompatible ferrofluids are developed to maintain mammalian

cell viability. We show that it is possible to enhance clinical relevant cells enrichment in a low cost and efficient manner.

Chapter 7 presents the separation scheme by combining both positive and negative magnetophoresis based on ferrofluids. It is used for sorting mixtures of particles with different magnetic properties, which extends the feasibility for ferrohyhydrohynamic sorting of microparticles and biological cells.

Chapter 8 summarizes the results and provides an outlook on their impacts on possible future work.

CHAPTER 2

THEORY

2.1. Introduction

2.1.1. Ferrofluids

Ferrofluids are stable suspensions of single domain magnetic nanoparticles, covered by a surfactant as shown in Figure 1, and suspended in a compatible carrier fluid. Most commonly used magnetic nanoparticles are iron oxides, including γ-Fe_2O_3 (maghemite) and Fe_3O_4 (magnetite). Maghemite particles have smaller saturation magnetization than that of magnetite. Typically, magnetic nanoparticles have diameters of 10s nanometers (nm) [39-42]. The surfactant layer helps overcome the Van der Waal's forces by preventing the particles from agglomerating, either via steric or electrostatic repulsions. Ferrofluids can serve as a uniform magnetic environment that surrounds non-magnetic objects in them. Cells and other non-magnetic objects within ferrofluids act as "magnetic holes" [43-47]. An externally applied magnetic field gradient attracts magnetic nanoparticles, which causes cells or

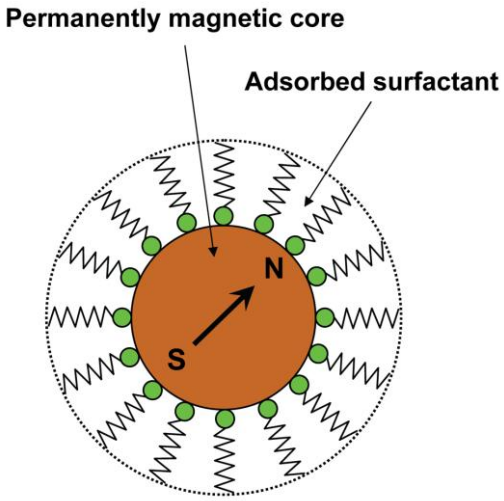

Figure 1. A ferrofluid consists of a carrier fluid, with single domain magnetic nanoparticles and stabilizing surfactant coated to prevent agglomeration.

non-magnetic objects to be effectively pushed away [48, 49]. As such, any non-magnetic object including biological cells inside a ferrofluid can be potentially trapped, manipulated and directed towards a given direction using different magnetic field patterns without "fluorescent tags", as shown in Figure 2. Manipulation of synthetic microparticles has been realized inside ferrofluids through this magnetic buoyancy force [48-51]. Magnitude of the force is proportional to the volume of particles, and depends on the shape and elasticity of particles in a nonlinear manner [39, 48, 49, 52, 53].

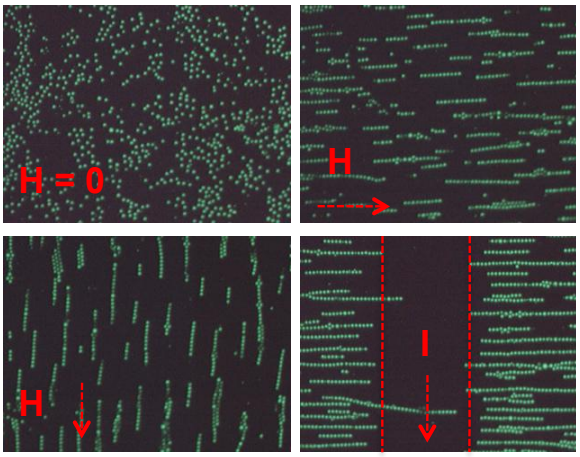

Figure 2. Non-magnetic particles (2 μm) placed inside ferrofluids experience forces when external magnetic fields are applied. **H** is the magnetic field, **I** is the amplitude of current in the electrodes.

2.1.2. Non-magnetic Microparticles Manipulation inside Ferrofluids

This magnetic manipulative technique, termed as "negative magnetophoresis" [53], is label-free and can address the aforementioned problems for cell manipulation [48, 54]. Representative applications of negative magnetophoresis in microfluidics include cell and particle manipulation and separation in either a paramagnetic salt solution or a ferrofluid. The former includes size-based polymer microparticles focusing and separating in a paramagnetic manganese (II) chloride solution under both permanent [55-58] and superconducting magnets [59, 60]. Particles are also separated based on their densities in a gadolinium (III) chloride solution [61, 62]. Jurkat cells can be trapped and arranged in bio-

compatible gadolinium-based salt solutions using microfabricated permanent magnet array [63]. A recent demonstration showed human histolytic lymphoma monocyte cells could be separated from red blood cells in a low-concentration bio-compatible gadolinium diethylenetriamine pentaacetic acid solution using a permanent magnet and a microfabricated ferromagnetic structure to concentrate flux lines [64].

A paramagnetic salt solution generally has low susceptibility and magnetization. For example, manganese (II) chloride's solubility limit in water at room temperature is 1470 kg/m^3, corresponding to a molar concentration of 11.7 M [65]. Its initial magnetic susceptibility is as low as 9×10^{-4} at this solubility limit, while its magnetization is 1.4×10^3 A/m and 1.4×10^4 A/m at magnetic flux densities of 2 T and 20 T, respectively [39]. Practical concentrations of the paramagnetic salt solution in the published literature are in the range of 0.1 – 1 M [55, 56, 58-60]. At this range, its susceptibility and magnetization are lower than the above-mentioned values by at least one order. Recall that the magnitude of magnetic force depends on the difference of magnetizations between cells and salt solution, as well as the magnetic field gradient. In order to compensate for its low susceptibility and magnetization under fields generated by permanent magnets (flux density 0.1 – 1 T), typical applications of a paramagnetic salt solution use either high fields from superconducting magnets [59, 60] or high field gradients from microfabricated ferromagnetic structures [64] to generate sufficient magnetic forces for manipulation. In practice, permanent magnet-based microfluidic devices are preferred over the ones with superconducting magnets or microstructures because they are low-cost, easy-to-operate and do not require power supplies to generate magnetic fields [66-69]. For practical applications, their advantages in cost and operation may outweigh the complications of

integrating either superconducting magnets or microfabricated electromagnets into microfluidic systems.

An ideal magnetic fluid that has relatively high susceptibility and magnetization under fields generated by permanent magnets is the ferrofluid. The susceptibility and magnetization of a ferrofluid are tunable through controlling its concentration of magnetic materials. For example, maximal volume fraction of a water-based magnetite ferrofluid is close to 10%. Given the bulk magnetization of magnetite is 4.46×10^5 A/m, this ferrofluid's initial susceptibility is on the order of 1, and its saturation magnetization is on the order of 10^4 A/m under fields generated from a hand-held permanent magnet, both of which are significantly larger than the values of a paramagnetic salt solution. Better magnetic properties of the ferrofluid enable its applications in a number of areas related to microfluidic manipulation. Recently, Yellen *et al*. demonstrated the transportation and assembly of colloidal particles inside ferrofluids on top of a substrate with microfabricated periodic micromagnets and suggested a particle sorting scheme based on their devices [70]. Kose *et al.* experimentally demonstrated an integrated microfluidic platform for the controlled sorting of micron-sized particles under traveling magnetic fields in static flow conditions [48]. They reported size-based separation of 173 particles of 9.9 μm diameter from 1294 particles of 2.2 μm diameter with 99.3% separation efficiency in less than one minute. Our approach, on the other hand, adopts a continuous flow configuration thus can achieve a higher (e.g., ~10^6 particles/hour) throughput. The device fabrication only needs a simple soft lithography step [71] and doesn't require microfabricated micromagnets or current-carrying electrodes, which significantly increase the cost associated with the device. The proposed microfluidic

platform can continuously separate non-magnetic microparticles based on their sizes inside water-based ferrofluids with the use of a simple permanent magnet.

2.1.3. Challenges

A simple, low-cost cell enrichment platform would benefit biological applications such as pathogen detection and cancer screening. However, these two issues limit applications of ferrohydrodynamic manipulation: cell visibility and biocompatibility of biological cells in ferrofluids. Reason for the opaqueness of ferrofluids can be explained from considerations of magnitude of optical depth $\tau = n\sigma l$ [52], where *n* is concentration of magnetic nanoparticles in the ferrofluid; σ is optical cross-sectional area of a nanoparticle, *i.e.*, geometric projected area of the nanoparticle, and *l* is length of optical path. If we define I_0 as fluorescent intensity of particle, and *I* as observed intensity after a given optical path through ferrofluids, $I/I_0 = e^{-\tau}$. To address this issue, it is clear that ferrofluids with relatively low solid volume fraction, as well as shallow microfluidic channel, are preferred for particle observation because of their small optical depth. In addition, magnetic fields can be used to push cells onto channel surface, increasing visibility of cells in fluorescent mode. We tried a combination of both bright-field and fluorescent modes microscopy to circumvent the opaqueness issue. Cells are readily visible in a shallow channel in bright-field micrographs.

Another critical issue is biocompatibility of ferrofluids. Using water-based ferrofluids with high concentration of magnetic nanoparticles for live cell manipulation and separation has been proven to be difficult in the past [48]. To extend this methodology towards biological cells manipulation, particularly human specimens such as blood and other bodily fluids, exfoliated musical cells, and tumor aspirates, ferrofluids properties

including materials, *p*H value, and surfactants need to be rendered biocompatible. Meanwhile, the overall colloidal system of ferrofluids under strong magnetic field must be maintained. Typically, nanoparticles within ferrofluids for cell applications are made of magnetite [72]. *p*H value of ferrofluids needs to be compatible with cell culture and maintained at 7.4. Salt concentration, tonicity, and surfactant must be carefully chosen close to physiological conditions to reduce cell death. Although these are stringent requirements, progress has been made towards synthesizing biocompatible ferrofluids. For example, Koser's group used citrate to stabilize cobalt-ferrite nanoparticles for live red blood cell and *Escherichia coli* cell sorting [48]. Yellen's group used Bovine Serum Albumin (BSA) to stabilize magnetite nanoparticles for human umbilical vein endothelial cells manipulation [50]. Viability tests from both studies have shown cells were able to retain their viability for up to several hours in ferrofluids.

In this thesis, we will use a commercially available *p*H ~7 magnetite ferrofluid at first for constructing a model system. Then we plan to synthesize a customized biocompatible ferrofluid for sorting mammalian cell specimens since few commercially ferrofluids for live biological cell manipulation are available.

2.2. Analytical model

Here we developed an analytical model to describe transport of non-magnetic particles within ferrofluids in a microfluidic system consisting of a microchannel and a permanent magnet. Numerical models using Finite Element Analysis (FEA) have been developed in the past for magnetophoretic particle transport within microfluidic devices, in which the particles themselves were magnetic, while the surrounding medium was non-magnetic [73-75]. The accuracy of numerical approaches depends heavily on mesh

quality. Therefore numerical simulations are not suitable for parametric studies aimed for quick device design and optimization. Analytical models were developed to enable accurate and fast parametric analysis of large-scale magnetophoretic systems [76, 77]. However, few have considered the opposite case, where the particles were non-magnetic, and the surrounding medium was magnetic (e.g., ferrofluids). We derived the equations of motion for particles in ferrofluids using analytical expressions for dominant magnetic and hydrodynamic forces. The magnetic force is obtained by using an analytical expression of magnetic field distributions in microchannel, in conjunction with a nonlinear magnetization model of ferrofluids. The model developed here can predict the transport of non-magnetic particles in ferrofluids under the influence of a permanent magnet in a microchannel. The model is also able to perform parametric analysis for quick device optimizations.

2.2.1. Force analysis

The system considered in the model consists of a microfluidic channel and a permanent magnet, as illustrated in Figure 3(a). Non-magnetic microparticles and ferrofluid mixture were introduced into the microfluidic channel Inlet 2 and hydrodynamically focused by the ferrofluid sheath flow from Inlet 1.Upon entering the main channel, deflection of microparticles from their flow paths occurred because of non-uniform magnetic fields produced by a long NdFeB permanent magnet embedded into the microfluidic channel. The motion of the particles was imaged through a 5× objective and a CCD camera. Dimensions of the channel and the magnet are labeled in Figures 3(b) and 3(c). The microfluidic channel is filled with ferrofluids. Non-magnetic spherical particles are introduced into the microchannel via inlet at the center point. Without external

magnetic fields, the particles are expected to exit the channel outlet at the center point, too. When a rectangular permanent magnet is placed at the center of channel length with its direction of magnetization perpendicular to channel wall, the bias field magnetizes the ferrofluid within the microchannel and subsequently deflects the particles' trajectories. The trajectories can be analyzed by considering dominant magnetic and hydrodynamic forces in the equations of motion.

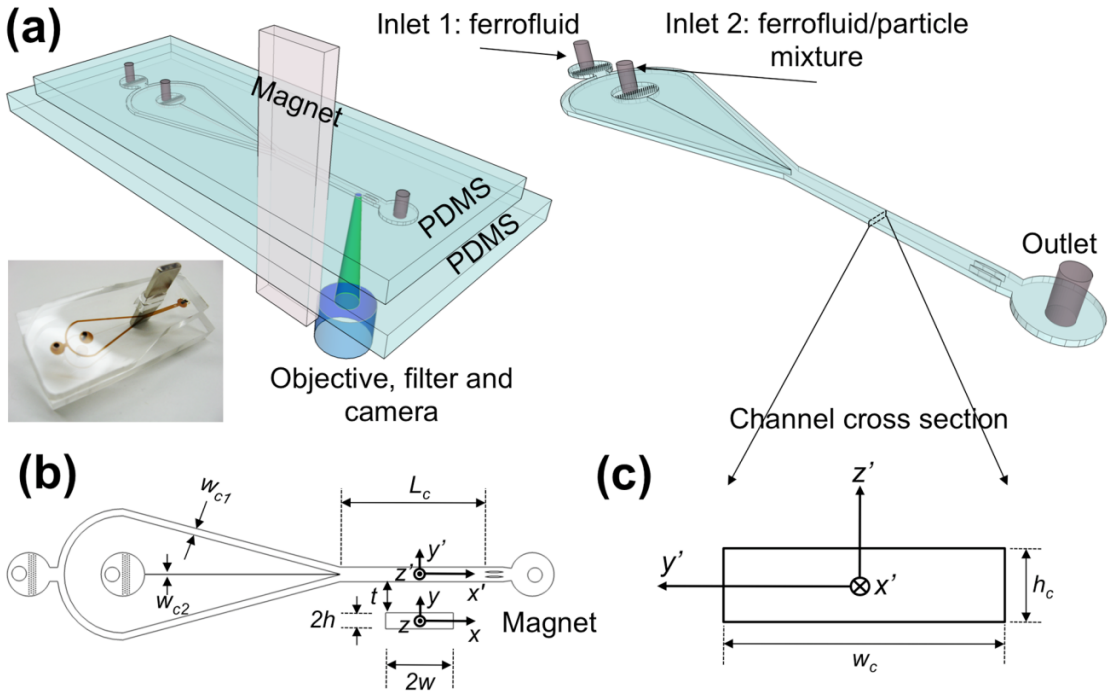

Figure 3. (a) Schematic representation of the microfluidic system with a permanent magnet and a microchannel. Inset shows an image of the fabricated device. (b) The dimensions of the microfluidic channel and the magnets, and their relative locations. L_c = 1 cm, $2w$ = 6.35 mm, $2h$ = 1.59 mm, t = 2.24 mm, w_{c1} = 485 μm, w_{c2} = 30 μm. x-y coordinate system is within the permanent magnet, with its origin at the center of the cross-section of the magnet. x'-y' coordinate system is within the microchannel, with its y' origin at the half width of the microchannel. (c) The cross-section of the microfluidic

channel. h_c = 26 μm and w_c = 1,000 μm.

Typically, particle transport in ferrofluids under external magnetic fields is governed by various forces and interactions including magnetic buoyancy force, hydrodynamic viscous drag force, gravity, buoyancy force, particle and microchannel surface interaction (van der Waal's force, electrostatic force and lubrication force), diffusion due to Brownian motion, particle and fluid interaction, interparticle effects (magnetic dipole-dipole interaction). For micron-sized particles in ferrofluids, only the magnetic and viscous forces are dominant. For example, we compute the gravitational and buoyant forces, $F_g = \frac{4}{3}\rho_p \pi R_p^3 g$, and $F_b = \frac{4}{3}\rho_f \pi R_p^3 g$. For a 2 μm (R_p = 1 μm) polystyrene particle in EMG 408 ferrofluid (ρ_p = 1050 kg/m^3, ρ_f = 1070 kg/m^3, g = 9.8 m/s), we obtain F_g = 4.31×10^{-2} pN, and F_b = 4.39×10^{-2} pN, both of which are more than two orders of magnitude smaller than magnetic buoyancy force (~pN). The molecular and electrical interaction between particles and surfaces of microchannel is referred as *Derjaguin-Landau-Verwey-Overbeek* (DLVO) force. DLVO force is a combination of the van der Waal's force and the electrostatic force. Electrostatic force can be either repulsive or attractive, while the van der Waal's force is always attractive. It is usually beneficial to treat surfaces of microchannel chemically and render the electrostatic force repulsive to avoid problems of particles sticking to channel surfaces [29]. DLVO force can be neglected after the proper surface treatment. The close proximity between particles and channel surface also affects the magnitude of hydrodynamic viscous drag force by introducing a non-dimensional factor accounting for the "wall effect" [78-80], which will be discussed in

details in section 2.2.3. Moreover, hydrodynamic lift force [79, 81], caused by viscous flow over a particle near channel surface, tries to levitate the particle and produces a lifting force, $F_l = 9.22\rho_p R_p^4 \gamma^2$, where γ is shear rate at the channel surface. Magnitude of the lifting force is much smaller than *p*N and is therefore neglected in the following analysis. When non-magnetic particles are sufficiently small, Brownian motion and diffusion start to affect the trajectories of the particles in ferrofluids. To estimate this effect, we obtain the diffusion coefficient *D* of a particle inside ferrofluids according to the Stokes-Einstein relation [82] $D = \frac{k_B T}{6\pi\eta R_p}$. For a 10 μm (R_p = 5 μm) polystyrene particle in a commercially available EMG 408 water based ferrofluid (η = 1.2×10^{-3} kg/m.s), its diffusion coefficient is 3.6×10^{-14} m^2/s at room temperature. After 20 seconds of diffusion, the particle will move an average distance of 0.9 μm. For a 1 μm (R_p = 0.5 μm) polystyrene particle, its diffusion coefficient is about one order larger than that of 10 μm particle, and the average diffusion distance increases to 2.7 μm. Even for 1 μm particles, diffusion effect is second order compared to magnetic and hydrodynamic forces. Concentration of non-magnetic particles in ferrofluids is assumed to be low such that inter-particle effects and particle/fluid interactions can also be neglected.

2.2.2. Magnetic buoyancy force

Commercial ferrofluids typically consist of magnetite (Fe_3O_4) nanoparticles with approximately 10 nm diameter. For example, the mean diameter of nanoparticles of EMG 408 ferrofluids from Ferrotec Co. has been determined from Transmission Electron Microscopy (TEM) images to be 10.2 nm with a standard deviation of 1.25 nm (see Figure 4(a).

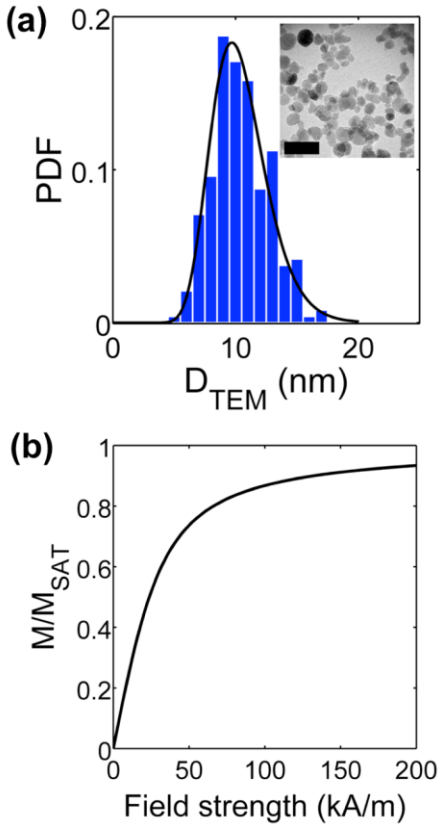

Figure 4. (a) Probability density function (PDF) for magnetic nanoparticle sizes was obtained via Transmission Electron Microscope (TEM) images from 240 individual, randomly selected nanoparticles. Diameter (D_{TEM}) of nanoparticles displays a log-normal distribution (mean, μ = 10.2 nm; standard deviation, σ = 1.25 nm). Inset depicts a typical TEM image of nanoparticles. The scale bar represents 40 nm. (b) The theoretical and normalized Langevin curve as a function of the magnetic field strength. **M** is the magnetization of the ferrofluid and $\mathbf{M_{SAT}}$ is the saturation magnetization. The ferrofluid parameters used to construct this curve matches the properties of EMG 408 water-based ferrofluid used in the experiments. EMG 408 ferrofluid is assumed to be superparamagnetic because of its low solid volume fraction.

This dilute ferrofluids exhibits superparamagnetic behavior illustrated by the magnetization curve shown in Figure 4(b). The saturation magnetization of ferrofluids is

generally low compared to that of ferromagnetic materials. The saturation magnetization of a ferrofluid M_{SAT} equals to ϕM_d, where ϕ is the volume fraction of the magnetic content and M_d is the saturation moment of the bulk material. EMG 408 ferrofluid with a solid volume fraction of 1.1% has a saturation magnetization of 5,252 A/m, given that the saturation moment of Fe_3O_4 is 44,600 A/m [39]. The magnetization curve of a low-concentration ferrofluid can be modeled accurately by considering the magnetic nanoparticles as a collection of individual and non-interacting magnetic dipoles. This approach leads to the Langevin function of ferrofluid magnetization [39],

$$\frac{M}{\phi M_d} = \frac{M}{M_{SAT}} = L(\alpha) = \coth(\alpha) - \frac{1}{\alpha}$$

(1)

where $\alpha = \frac{\pi \mu_0 M_d H d^2}{6 k_B T}$, μ_0 is permeability of free space, H is magnitude of non-uniform magnetic fields, d is mean diameter of nanoparticle, k_B is Boltzmann constant, T is temperature.

Under non-uniform magnetic fields, particles inside ferrofluids experience a magnetic buoyancy force, $\mathbf{F}_m$. The magnitude of force can be calculated from a Maxwell stress tensor (Rosensweig 1985),

$$\mathbf{F}_m = -\oint_S \left(\frac{1}{2} \mu_0 M_n^2 + \mu_0 \int_0^H M dH \right) \hat{\mathbf{n}} dS$$

(2)

where S is surface that just encloses the non-magnetic particle, H is magnitude of non-uniform magnetic fields, $\hat{\mathbf{n}}$ is outward-directed unit normal vector at the particle surface,

and M_n is normal component of ferrofluid magnetization adjacent to the surface S enclosing the particle. In the limit of dilute ferrofluid or intense applied magnetic field, $\frac{1}{2} M_n^2 / \bar{M}H << 1$, where $\bar{M}$ is mean ferrofluid magnetization. Therefore, magnetic buoyancy force on a non-magnetic particle inside ferrofluids can be simply expressed as,

$$\mathbf{F}_m = -V\mu_0(\mathbf{M}\cdot\nabla)\mathbf{H}$$

(3)

where V is volume of the non-magnetic particle, **M** is effective magnetization of the ferrofluid surrounding the particle and **H** is magnetic field strength at the center of the particle. The presence of the minus sign in front of the term indicates non-magnetic particle immersed in ferrofluids experiences a force in the direction of weaker magnetic field. Effective ferrofluid magnetization **M** is related to the magnetization of ferrofluid $\mathbf{M}_f$ through a "demagnetization" factor, which accounts for shape-dependent demagnetization of ferrofluids due to presence of the non-magnetic particle. Equation (3) takes magnetic field **H** to be the field at the center of the particle inside ferrofluid sample. Experimentally, permanent magnet produces an external field $\mathbf{H}_e$ in the place where ferrofluid channel is located. It is necessary to determine the value of field inside ferrofluids sample **H** by relating it to applied field $\mathbf{H}_e$.

$$\mathbf{H} = \mathbf{H}_e - c\cdot\mathbf{M}_f$$

(4)

where c is "demagnetization" factor of rectangular ferrofluid-filled microchannel. Ferrofluid magnetization $\mathbf{M}_f$ in our case is much smaller than the external field $\mathbf{H}_e$

produced by a Neodymium-Iron-Boron (NdFeB) magnet. As a result, magnetic field at the center of the particle **H** can be approximated as external field $\mathbf{H}_e$.

In order to calculate the magnitude of magnetic buoyancy force, we need to know the effective magnetization of ferrofluid **M** adjacent to the particle. The nonlinearity of ferrofluid magnetization makes the identification of the effective magnetization **M** complicated. In a very weak magnetic field ($H << H_{SAT}$, where H_{SAT} is magnitude of the minimal magnetic field strength to saturate ferrofluids), we can linearize the Langevin curve to define an initial magnetic susceptibility χ and form an effective dipole moment $-V\chi H$ for the particle. Shape dependent "demagnetization" field needs to be considered under this assumption. In a large magnetic field that saturates ferrofluids, effective magnetic moment of a particle immersed in ferrofluids can be extracted as $-VM_{SAT}$, and particle shape has virtually no influence on this force expression because demagnetization is not significant when $M_{SAT} << H$ [53]. When applied magnetic fields fall in between the above-mentioned extreme cases, we can obtain magnetization of the ferrofluid $\mathbf{M}_f$ from the Langevin curve and decide whether or not to apply "demagnetization" factor depending on the magnitude of external magnetic fields. In this paper, EMG 408 ferrofluid used in our experiment is dilute, and external magnetic field is much larger than saturation magnetization of this ferrofluid. Therefore, we can assume "demagnetization" field is small enough so that **M** equals to $\mathbf{M}_f$. The value of $\mathbf{M}_f$ can be calculated from the Langevin function.

The magnetic buoyancy force can be expressed in both *x* and *y* components,

$$\mathbf{F}_m(x,y) = F_{mx}(x,y)\hat{\mathbf{x}} + F_{my}(x,y)\hat{\mathbf{y}}$$

(5)

where

$$F_{mx}(x,y) = -V\mu_0\left[M_x \frac{\partial H_x(x,y)}{\partial x} + M_y \frac{\partial H_x(x,y)}{\partial y} \right]$$

(6)

$$F_{my}(x,y) = -V\mu_0\left[M_x \frac{\partial H_y(x,y)}{\partial x} + M_y \frac{\partial H_y(x,y)}{\partial y} \right]$$

(7)

where

$$M = \phi M_d \times \left[\coth(\alpha) - \frac{1}{\alpha} \right]$$

(8)

$$M_x = M \times \cos\left[\tan^{-1} \frac{H_y}{H_x} \right]$$

(9)

$$M_y = M \times \sin\left[\tan^{-1} \frac{H_y}{H_x} \right]$$

(10)

Analytical solutions for magnetic fields of a single long rectangular permanent magnet of width 2*w* and height 2*h* that is centered with respect to the origin in the *x* – *y* plane can be derived as following [76]. Assume the magnet has a residual magnetization M_S,

$$H_x(x,y)=\frac{M_S}{4\pi}\left\{\ln\left[\frac{(x+w)^2+(y-h)^2}{(x+w)^2+(y+h)^2}\right]-\ln\left[\frac{(x-w)^2+(y-h)^2}{(x-w)^2+(y+h)^2}\right]\right\}$$

(11)

$$H_y(x,y)=\frac{M_S}{2\pi}\left\{\tan^{-1}\left[\frac{2h(x+w)}{(x+w)^2+y^2-h^2}\right]-\tan^{-1}\left[\frac{2h(x-w)}{(x-w)^2+y^2-h^2}\right]\right\}$$

(12)

The expressions for the magnetic field gradients are,

$$\frac{\partial H_x(x,y)}{\partial x}=\frac{M_S}{2\pi}\left[\frac{x+w}{(x+w)^2+(y-h)^2}-\frac{x+w}{(x+w)^2+(y+h)^2}-\frac{x-w}{(x-w)^2+(y-h)^2}+\frac{x-w}{(x-w)^2+(y+h)^2}\right]$$

(13)

$$\frac{\partial H_x(x,y)}{\partial y}=\frac{M_S}{2\pi}\left[\frac{y-h}{(x+w)^2+(y-h)^2}-\frac{y-h}{(x-w)^2+(y-h)^2}-\frac{y+h}{(x+w)^2+(y+h)^2}+\frac{y+h}{(x-w)^2+(y+h)^2}\right]$$

(14)

$$\frac{\partial H_y(x,y)}{\partial x}=\frac{M_S}{\pi}\left\{\frac{h\left[y^2-(x+w)^2-h^2\right]}{\left[(x+w)^2+y^2-h^2\right]+4h^2(x+w)^2}-\frac{h\left[y^2-(x-w)^2-h^2\right]}{\left[(x-w)^2+y^2-h^2\right]+4h^2(x-w)^2}\right\}$$

(15)

$$\frac{\partial H_y(x,y)}{\partial y} = \frac{M_S}{\pi}\left\{\frac{hy(x-w)}{\left[(x-w)^2+y^2-h^2\right]+4h^2(x-w)^2} - \frac{hy(x+w)}{\left[(x+w)^2+y^2-h^2\right]+4h^2(x+w)^2}\right\}$$

(16)

2.2.3. Hydrodynamic drag force

When a non-magnetic particle is driven by magnetic buoyancy force and moves in ferrofluids, the resistance from ferrofluids is named hydrodynamic drag force. The force is caused by the viscosity of medium and can be calculated for a spherical particle in a low Reynolds number flow [83],

$$\mathbf{F}_d = 3\pi\eta D_p(\mathbf{v}_f - \mathbf{v}_p) f_D$$

(17)

where η is viscosity of ferrofluids, D_p is diameter of spherical particle, and $\mathbf{v}_f$ and $\mathbf{v}_p$ are velocity vectors of ferrofluids and the particle, respectively. f_D is hydrodynamic drag force coefficient of the particle and incorporates the influence of a solid surface in the vicinity of the moving particle ("wall effect"). It is a resistance function of the hydrodynamic interaction between the particle and surface. Its appearance indicates increased fluid viscosity the large particle experiences as it moves close to the microfluidic channel surface [78, 80],

$$f_D = \left[1 - \frac{9}{16}\left(\frac{D_p}{D_p+2z_p}\right) + \frac{1}{8}\left(\frac{D_p}{D_p+2z_p}\right)^3 - \frac{45}{256}\left(\frac{D_p}{D_p+2z_p}\right)^4 - \frac{1}{16}\left(\frac{D_p}{D_p+2z_p}\right)^5\right]^{-1}$$

(18)

where z_p is distance between surface of the particle and channel wall.

To evaluate the drag force, we need an expression for the fluid velocity $\mathbf{v}_f$ in the rectangular microfluidic channel depicted in Figure 3. Let L_c denote length of the channel and h_c and w_c denote height and width of its rectangular cross section. The laminar nature of flow is estimated from the Reynolds number $\mathrm{Re} = \frac{\rho U_0 L_0}{\eta}$, where U_0 is characteristic velocity of the flow, L_0 is characteristic dimension of the microchannel, ρ and η are density and viscosity of the fluid, respectively. Typically, $U_0 \approx 0.001$ m/s, $L_0 \approx 20$ μm, $\rho \approx 1000$ kg/m^3, $\eta \approx 0.001$ kg/m·s. Therefore, Re ≈ 0.02, indicating laminar flow. We assume fully developed laminar flow with the flow velocity parallel to the x'-axis, and varying across its cross section,

$$\mathbf{v}_f = v_f(y', z')\hat{\mathbf{x}}$$

(19)

We choose to use coordinates y' and z' centered with respect to the cross-section of the channel, and this coordinate system differs from the coordinate system used for magnetic field analysis [77]. The velocity profile for fully developed laminar flow is expressed as [84, 85],

$$v_f = \left(\frac{\Delta P}{L_c}\right)\left(\frac{4h_c^2}{\eta\pi^3}\right)\sum_{n=0}^{\infty}\frac{(-1)^n}{(2n+1)^3} \times \left\{1 - \frac{\cosh\frac{(2n+1)\pi y'}{h_c}}{\cosh\frac{(2n+1)\pi w_c}{2h_c}}\right\} \times \cos\frac{(2n+1)\pi z'}{2h_c}$$

(20)

where ΔP is change in pressure across the length L_c of the channel. Channel aspect ratio is defined as $\varepsilon = h_c / w_c$. Under the condition of $0 < \varepsilon < 2$, calculation error is found to be less than 1% when only $n = 0$ and 1 terms are used to represent the flow profile in microchannels [85].

$$v_f = \left(\frac{\Delta P}{L_c}\right)\left(\frac{4h_c^2}{\eta\pi^3}\right)\left\{\left[1-\frac{\cosh\frac{\pi y'}{h_c}}{\cosh\frac{\pi w_c}{2h_c}}\right]\times\cos\frac{\pi z'}{h_c}-\frac{1}{27}\left[1-\frac{\cosh\frac{3\pi y'}{h_c}}{\cosh\frac{3\pi w_c}{2h_c}}\right]\times\cos\frac{3\pi z'}{h_c}\right\} \tag{21}$$

In a typical microfluidic experiment setup, volumetric flow rate Q, instead of pressure drop across the channel, is available to the experimenter. Therefore, we rewrite the pressure drop in terms of the flow rate,

$$\Delta P = \frac{QL_c\eta\pi^4}{8w_c h_c^3}\times\left\{\left[1-\frac{2h_c}{\pi w_c}\tanh\left(\frac{\pi w_c}{2h_c}\right)\right]+\frac{1}{81}\left[1-\frac{2h_c}{3\pi w_c}\tanh\left(\frac{3\pi w_c}{2h_c}\right)\right]\right\}^{-1} \tag{22}$$

Finally, the expression for fluid velocity $\mathbf{v}_f$ in the rectangular microfluidic channel is,

$$v_f = \frac{Q\pi}{2w_c h_c}\times\left\{\left[1-\frac{2h_c}{\pi w_c}\tanh\left(\frac{\pi w_c}{2h_c}\right)\right]+\frac{1}{81}\left[1-\frac{2h_c}{3\pi w_c}\tanh\left(\frac{3\pi w_c}{2h_c}\right)\right]\right\}^{-1} \times\left\{\left[1-\frac{\cosh\frac{\pi y'}{h_c}}{\cosh\frac{\pi w_c}{2h_c}}\right]\times\cos\frac{\pi z'}{2h_c}-\frac{1}{27}\left[1-\frac{\cosh\frac{3\pi y'}{h_c}}{\cosh\frac{3\pi w_c}{2h_c}}\right]\times\cos\frac{3\pi z'}{h_c}\right\} \tag{23}$$

2.2.4. Equations of motion

The equations of motion for a non-magnetic particle in the microchannel are,

$$m\frac{dv_{p,x}}{dt} = F_{mx}(x,y) + 3\pi\eta D_p(v_f - v_{p,x})f_D$$

(24)

$$m\frac{dv_{p,y}}{dt} = F_{my}(x,y) - 3\pi\eta D_p v_{p,y} f_D$$

(25)

Since the Reynolds number in microfluidic channels is very small, normally on the order of 0.01, viscous effect often dominates over inertial effect. As a result, the left hand side terms of Equations (24) and (25) reduce to zero, which leads to,

$$v_{p,x} = \frac{dx}{dt} = \frac{F_{mx} + 3\pi\eta D_p v_f f_D}{3\pi\eta D_p f_D}$$

(26)

$$v_{p,y} = \frac{dy}{dt} = \frac{F_{my}}{3\pi\eta D_p f_D}$$

(27)

With initial conditions $x(0)$ and $y(0)$, these two ordinary differential equations can be solved numerically using Runge-Kutta method. We solved them in MATLAB (Version R2007a, Mathworks Inc., Natick, MA) using ode45 function, which is an automatic step-size Runge-Kutta integration method using a fourth and fifth order pair.

2.3. Materials and Methods

A microfluidic device with one NdFeB permanent magnet was fabricated to experimentally study the trajectories of particles, as shown in the inset of Figure 5(a). EMG 408 ferrofluid was used in the experiments. The volume fraction of the magnetite particles for this ferrofluid is 1.1%, corresponding to a saturation magnetization of 5,252 A/m. The viscosity of the ferrofluid was measured to be 1.2 $N \cdot s/m^2$ by a Rheometer (DV-III+, Brookfield Engineering Laboratories Inc., Middleboro, MA). Two different sizes (4.8 μm and 7.3 μm in diameters) of green fluorescent polystyrene spherical particles (Thermo Fisher Scientific Inc., Waltham, MA) with a density of 1.05 g/cm^3 were used. The coefficient of variation (the ratio of the standard deviation to the mean) of the particle diameters was less than 5%. Fluorescent particles suspension was first diluted with DI water containing 0.1% Tween 20 to prevent particle aggregation, then mixed with ferrofluids for flow experiments. PDMS microfluidic channel was fabricated through a standard soft-lithography approach and attached to the flat surface of another piece of PDMS (Xia and Whitesides 1998). The mask was created using AutoCAD 2008 (Autodesk Inc., San Rafael, CA) and printed by a commercial photo-plotting company (CAD/Art Services Inc, Bandon, Oregon). Dimensions of the microfluidic channel are listed in Figure 3. The thickness of the channel was measured to be 26 μm by a profilometer (Dektak 150, Veeco Instruments Inc., Chadds Ford, PA). PDMS surfaces were treated before attachment with plasma (PDC-32G plasma cleaner, Harrick Plasma, Ithaca, NY) at 11.2 Pa O_2 partial pressure with 18 W power for 1 minute. The flow experiment was conducted on the stage of an inverted microscope (Zeiss Axio Observer, Carl Zeiss Inc., Germany). Before liquid injection, completed device was exposed again to plasma for 10 minutes to keep the surfaces hydrophilic. Triton X-100 solution was

injected into the channel. The solution was kept in the channel for 20 minutes then purged with N_2 gas. This step ensured that the polystyrene particles would not attach to PDMS surfaces during experiments. The microfluidic channel was afterwards filled with air-bubble free EMG 408 ferrofluid. During experiments, ferrofluid injection into Inlet 1 was maintained at variable flow rates using a syringe pump (KDS 101, KD Scientific, Holliston, MA). Ferrofluid and particles mixture was injected into Inlet 2 using a second syringe pump (Nexus 3000, Chemyx Inc., Stafford, TX). Non-uniform magnetic field was generated by one NdFeB permanent magnet with the magnetization directed across its thickness. The magnet is 6.35 mm in width, 1.59 mm in thickness and 25.4 mm in length, and was placed 2.24 mm away from microfluidic channel. The magnetic flux density at the center of the magnets' pole surface was measured to be 159.9 mT by a Gauss meter (Model 5080, Sypris, Orlando, FL) and an axial probe with 0.381 mm diameter of circular active area. The images of fluorescent particles were recorded through a fluorescent filter set (41001 FITC, Chroma Technology Corp., Rockingham, VT) and a 5× objective with a CCD camera (SPOT RT3, Diagnostic Instruments, Inc., Sterling Heights, MI). ImageJ® software was used to record the trajectories and deflections of the particles inside ferrofluids.

2.4. Results and Discussion

We obtained the theoretical trajectories of non-magnetic particles in a microfluidic system depicted in Figure 3(a) by solving Equations (26) and (27) numerically using ode45 function in MATLAB. Specifically, we studied the spherical particles with variable diameters from 1 to 10 μm in a microfluidic system that consists of a microchannel that is 26 μm high, 1,000 μm wide, and 1 cm long (L_c = 1 cm, h_c = 26

μm and w_c = 1,000 μm). Total flow rate Q at the inlet of the microchannel was varied between 5 to 25 μl/min. The ferrofluid in the microchannel had a viscosity of 1.2 N·s/m^2 and a saturation magnetization of 5,252 A/m. The volume fraction of the ferrofluid was 1.1%. The mean diameter of nanoparticles was 10 nm. The permanent magnet was placed at the center of the length of the microchannel with its direction of magnetization perpendicular to the flow. The distance between the magnet and the channel was 2.24 mm (edge to edge). Throughout the analysis we assumed that the residual flux density ($\mu_0 M_S$) of the permanent NdFeB magnet was 1.13 T. The magnet was 6.35 mm in width (2w), 1.59 mm in height (2h) and 25.4 mm in length. These simulation parameters were chosen to match the experimental conditions.

Magnitude of magnetic buoyancy force depends on both the external magnetic fields and the field gradient. It is thus important to model magnetic fields from a permanent magnet with great precision. We chose to use an analytical approach instead of numerical Finite Element Analysis (FEA) approach to calculate magnetic fields. Analytical solution provides exact values of field and its gradient at each point of interest, while solutions from FEA depends heavily on the mesh quality, which will likely introduce error into magnetic buoyancy force calculation. Equations (11) – (16) are analytical solutions of magnetic field and field gradient for an infinitely long permanent magnet with 2w width and 2h height. The direction of the magnetization is across the magnet's thickness. Analytical solutions, numerical FEA solutions, as well as measurement data from a Gauss meter of magnetic fields were compared for the permanent magnet. FEA solution of the permanent magnet was calculated by magnetostatics solvers in COMSOL Multiphysics (Version 3.5a, COMSOL Inc.,

Burlington, MA). A 2D solver was used to compute the field in a 0.5 m × 0.2 m region containing the permanent magnet's cross-section (6.35 mm × 1.59 mm) at center. A 3D solver was used to compute the field in a 0.5 m × 0.2 m × 2 m region containing the permanent magnet (6.35 mm × 1.59 mm × 25.4 mm). The magnetic field component perpendicular to the region boundary all went to zero at the boundaries. Figure 5(a) shows that analytical solutions of magnetic field match both FEA solutions and experimental results reasonably well. Figure 5(b) depicts the distribution of magnetic fields inside the microfluidic channel using analytical solutions. Figure 5(c) shows the normalized ferrofluid magnetization inside the microfluidic channel. We concluded that EMG 408 ferrofluid in the microchannel was not fully saturated under the permanent magnet. However, magnetic fields produced by the magnet (40,000 – 80,000 A/m) were approximately one order larger than saturation magnetization of the ferrofluid (5,252 A/m), thus "demagnetization" field of the non-magnetic particle can still be neglected in the following analysis. Figure 5(d) shows computed x and y components of the magnetic buoyancy force on a 5 μm particle along line of symmetry ($y' = 0$) of the microchannel. The magnitude of force is on the order of pN. The horizontal component (x) of force changes its polarity at the center of the magnet ($x = 0$). Particles to the left of the magnet experience x-direction deceleration and move slower than the speed of ferrofluids; particles to the right of the magnet experience x-direction acceleration and move faster than the speed of ferrofluids. The vertical y-component of magnetic buoyancy force is always positive. A particle entering the microchannel acquires a non-zero y-direction speed, which leads to its deflection in y-direction as it moves across the channel.

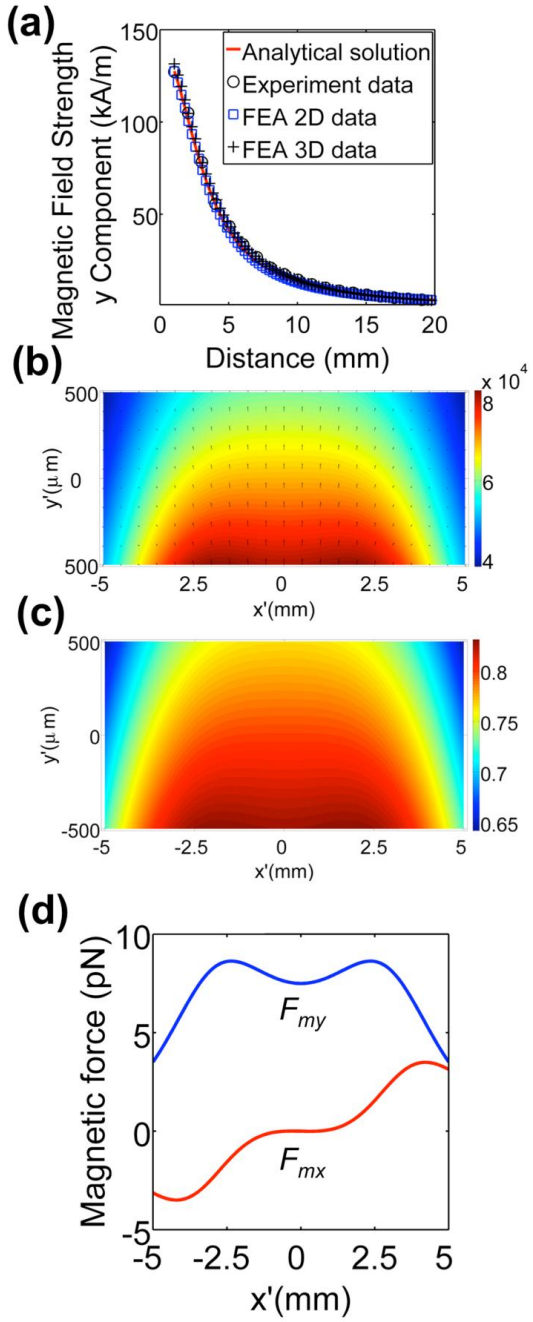

Figure 5. (a) Comparison of simulated (analytical model and FEA) and measured magnetic field strength produced by the permanent magnet. The magnetization and geometry of the permanent magnet are described in the main text. The plot shows the *y*-component of the magnetic field strength at the center of the magnet ($z = 0$) decreases as the distance between the surface of the magnet and Hall sensor inside the Gauss meter

probe increases. (b) Simulated magnetic field distribution in the microchannel (unit of surface plot: A/m). (c) Simulated normalized ferrofluid magnetization in the microchannel. (d) Simulated *x* and *y* components of the magnetic buoyancy force on a 5 μm particle along the line of symmetry ($y' = 0$) in the microchannel.

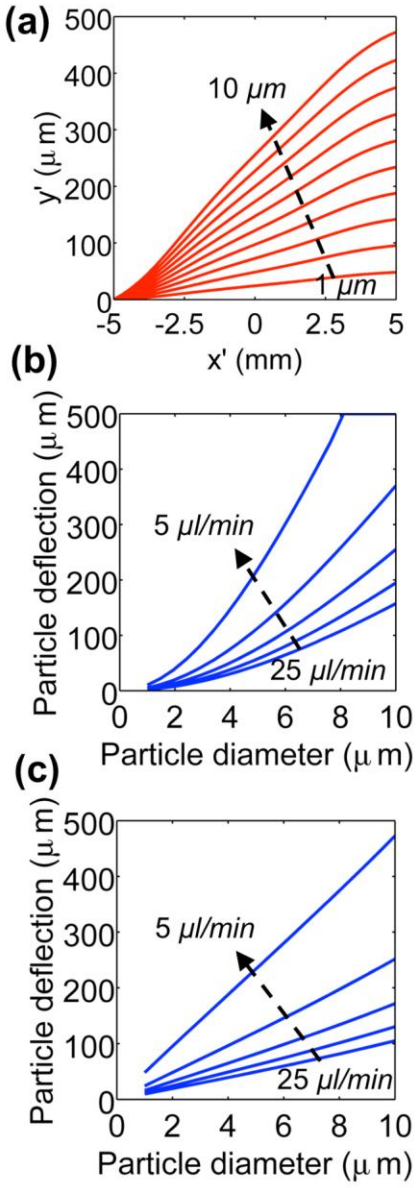

Figure 6. (a) Simulated trajectories of particles (1 μm to 10 μm in diameter) in the

microchannel at a constant flow rate of 5 μl/min. (b) Simulated deflections of particles from the inlet to the outlet (1 cm distance) at different flow rates (5 μl/min to 25 μl/min) when the particles are at the center-plane in the *z*-direction of the microchannel. (c) Simulated deflections of particles from the inlet to the outlet (1 cm distance) at different flow rates (5 μl/min to 25 μl/min) when the particles are in contact with the channel surface (z_p = 0).

Figure 6(a) shows simulated trajectories of particles with their diameters ranging from 1 to 10 μm. Flow rate *Q* at the inlet was constant at 5 μl/min. Particles were assumed to enter the microchannel at the center point (y' = 0). We found that there was a monotonic increment in the particle deflection (calculated from $|y'(\text{inlet}) - y'(\text{outlet})|$) with increasing particle size. Figure 6(b) depicts a quadratic relationship between deflections and sizes of particles at different flow rates. Particles of different diameters were assumed to be flowing at the center-plane in the *z*-direction of the microchannel, where flow speed of ferrofluids in the *x*-direction was maximal and constant. Under such condition, the time it takes for particles of different sizes to travel across the microchannel is also constant. The quadratic relationship can then be explained through a simple force analysis. Magnetic buoyancy force is proportional to the volume of the particle (D_p^3), while hydrodynamic viscous drag scales only with the diameter of the particle D_p . Therefore, particle velocity in the *y*-direction balanced by both magnetic buoyancy and hydrodynamic drag force depends on D_p^2, which explains the quadratic relationship between particle deflections and sizes in theory.In experiments, however, the particles were not flowing at the center-plane in the *z*-direction of the channel. In fact,

virtually all particles were pushed into contact with the bottom surface of the channel to help the experimenter visualize fluorescence from the particles. Due to the opaqueness of ferrofluids, fluorescent particles are only visible when they are very close to surfaces of the microfluidic channel. In our experiments, to ensure that all particles were close to the bottom surface of the microchannel, we moved the permanent magnet slightly in the positive *z*-direction. This in turn created a negative *z*-direction component of magnetic buoyancy force that can push particles towards the bottom surface of the channel. Magnitude of the force is on the order of 1 *p*N for 2 μm particles, which is much larger than the net force due to gravity and fluid buoyancy of particles. As a result, the particles were quickly pushed towards the bottom surface of the channel, balanced by hydrodynamic viscous drag force, with a mean speed of ~100 μm/s. We observed in the experiments that all particles were pushed onto bottom surface of the channel as soon as they entered the channel. It should be noted that both *x* and *y* components of magnetic fields were affected by less than 1% with the permanent magnet being off-centered by 1 mm. In the subsequent simulation, we assumed all particles are at the bottom surface of the channel, which makes $z_p = 0$. In this limit, $f_D \approx 3$ according to Equation (18), so that hydrodynamic drag of a particle is three times larger than that when no solid surface was in the vicinity of that particle (Liu et al. 2009; Gijs et al. 2010). Under this condition, the time it takes for particles of different sizes to travel across the microchannel is not constant any more. When a particle is in contact with the surface of the channel, its diameter directly determines the *z*-location of the particle center and its corresponding flow plane in the *z*-direction. As a result, larger particles travel faster than smaller ones when $z_p = 0$ in a rectangular microchannel channel. Therefore, larger particles have a

shorter residual time in the microchannel compared to small ones, resulting in overall smaller deflections compared to the results obtained in Figure 6(b) under the assumption that all particles travel at the same speed. Figure 6(c) depicts such relationship between deflections and sizes of the particles when z_p = 0.

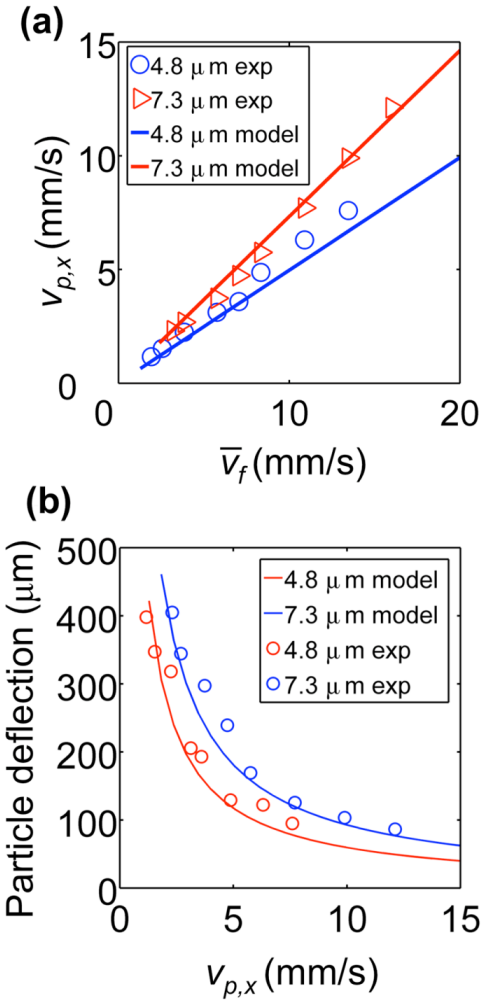

Figure 7. (a) Simulated and measured speed ($v_{p,x}$) of particles (4.8 μm and 7.3 μm in diameter) when the particles are in contact of the channel surface as a function of the mean flow rate ($\overline{v}_f$) in the microchannel. (b) Simulated and measured deflections of the particles (4.8 μm and 7.3 μm in diameter) when the particles are in contact of the channel surface.

Figure 7(a) compares measured speeds of the particles (4.8 μm and 7.3 μm in diameters) in experiments extracted from sequential fluorescent images to the simulated particle speeds using the analytical model under $z_p = 0$ condition. These two speeds agreed reasonably well, indicating that particles in the experiments were indeed in contact with the channel surface. Figure 7(b) shows the comparison between theoretically and experimentally obtained deflections of both 4.8 μm and 7.3 μm particles at different particle velocities. Theoretical deflections were calculated from $|y'(\text{inlet}) - y'(\text{outlet})|$, where y'(inlet) and y'(outlet) were y-locations of particles in the microchannel at the inlet and outlet, respectively. Experimental deflections were extracted from the sequential fluorescent images. Both values again agreed reasonably well, confirming the validity of our analytical model in predicating the trajectories of the particles.

CHAPTER 3

FOCUSING NON-MAGNETIC PARTICLES IN A MICROFLUIDIC CHANNEL

3.1. Introduction

Over the past decade, microfluidic devices have been increasingly used to manipulate particles and cells owing to their reduced sample consumption, low cost, small footprints and other advantages [8, 9, 86, 87]. Among various manipulation operations, focusing microparticles into a narrow stream becomes a critical step in these devices in order to enable downstream analytical procedures. For example, in miniaturized flow cytometry schemes, fluorescently or magnetically labeled microparticles (both synthetic and biological) need to be focused into a tiny volume to permit accurate counting and sorting. Many microfluidic particle-focusing techniques have been developed for such application, including the ones using hydrodynamic sheath flow [88, 89], electrokinetic sheath flow [90], optical force [91], dielectrophoretic force [92, 93], and acoustic force [94, 95], as detailed in three excellent reviews by Huh *et al.* [96], Chung and Kim [97], and Xuan *et al.* [98].

Using magnetic force for microparticles focusing [99] provides an attractive alternative to the above-mentioned techniques. Functionalized magnetic beads of various different sizes (typically several microns in diameter) can be used to specifically transport particles and cells from solution using a simple magnetic setup with great controllability and reliability [30, 100, 101]. It is estimated that magnitude of magnetic forces on microparticles can be as high as nanoNewtons [30, 101]. Commonly used magnetic materials, for example, iron oxides have minimal interferences with biological and chemical

processes of samples [72, 102-104]. Furthermore, magnetic manipulation can be implemented with the aid of simple permanent magnets or electromagnets, rendering the cost and integration effort of systems lower.

In chapter 2, we have introduced the principle of microparticles manipulation methods by using magnetic fluids, including paramagnetic solution and ferrofluids [48, 105]. The purpose of using magnetic fluids is to induce an effective magnetic dipole moment within a non-magnetic object. Under non-uniform magnetic field, particle will experience a magnetic buoyancy force, analogous to buoyancy force, as magnitude of the force is proportional to volume of the particle. Since low susceptibility of paramagnetic salt solutions often translates to slower focusing speed and lower throughput [39], we aim to develop a novel microfluidic particle-focusing scheme based ferrofluids.

3.2. Working Mechanism

A schematic of the prototype device using a PDMS channel fabricated by standard soft lithography is shown in Figure 8(a). A pair of Neodymium-Iron-Boron (NdFeB) magnets, with their magnetizations facing each other, is embedded in opposite sides of the PDMS channel, creating a large magnetic field gradient between edges of the magnets and center of the microfluidic channel. Microparticles and ferrofluid mixture solutions are injected into the microfluidic channel by a pressure-driven flow. Once entering the region between magnets, deflections of non-magnetic particles from their laminar flow paths occur because of the magnetic buoyancy forces. Magnitudes of the force are proportional to the volume of particles. Counter-acting hydrodynamic drag force, on the other hand, scales with the diameter of the particles. This observation was

used to continuously focus non-magnetic particles in a microfluidic channel with ferrofluids.

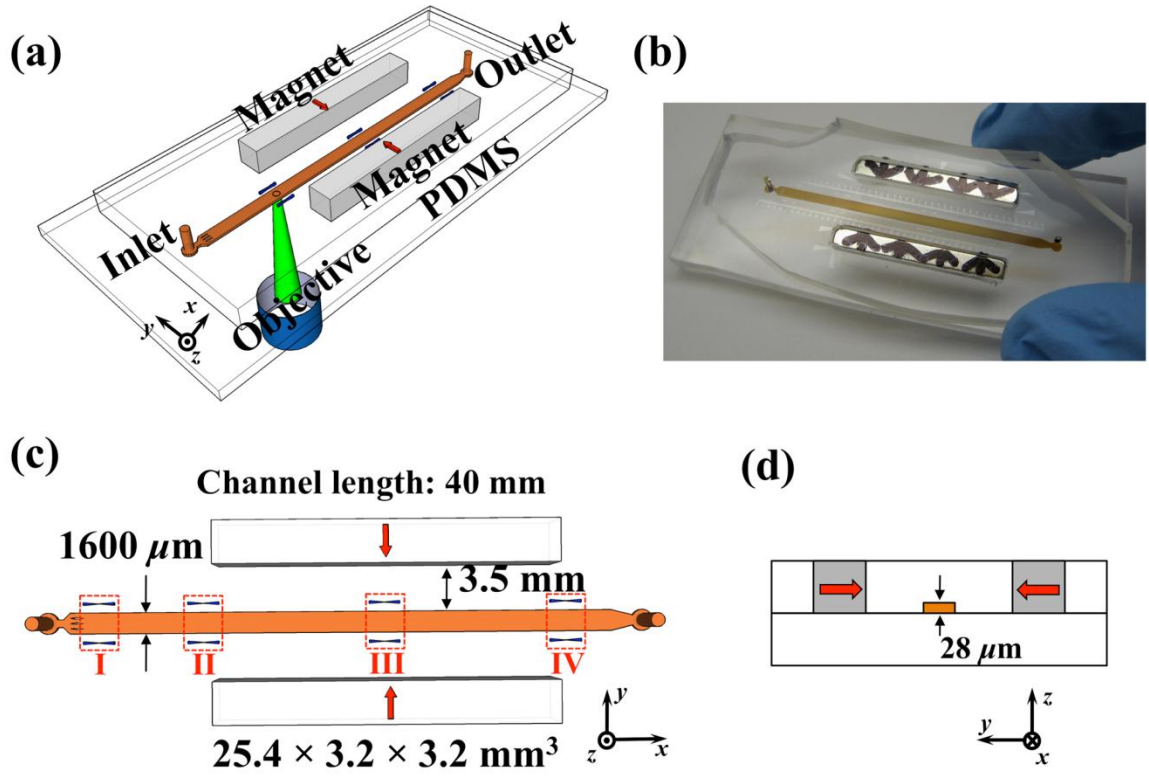

Figure 8 . (a) Schematic representation of the focusing device with permanent magnets and a microfluidic channel. (b) An image of the fabricated device. (c) Topview of the system and locations of the observation windows. Red arrows indicate the direction of magnet's magnetization. The origin of coordinate system is at the center of the microchannel. (d) Cross-section of the system.

In chapter 2, a 2D "negative magnetophoresis" model was developed to investigate the transport of non-magnetic particles in magnetic fluids and its validity has been confirmed by experimental results. In this work, we extend our analytical model to enable fast and accurate predictions of microparticle trajectories in all three dimensions.

We choose analytical model over numerical ones due to the consideration of simulation speed and accuracy. The accuracy of numerical approaches depends heavily on their mesh quality. They are time-consuming and not suitable for parametric studies aimed for quick device design and optimization. The 2D model developed before only considers particle transport in the plane that is perpendicular to the channel depth, and assume the particle is fixed at a specific position along the channel depth. This assumption is not valid in most of realistic experimental setups, where particles are free to flow along the channel depth, on which its velocity closely depends. Our new model on the other hand provides comprehensive information of particles' trajectory in 3D and is much closer to real experimental conditions. It takes into account important optimization parameters including fluid properties, magnet dimensions and relative positions of the magnet to the channel, and provides crucial information such as magnetic fields distribution, forces, particle velocity and trajectory in 3D. Briefly, we obtain 3D microparticle trajectories in microchannels by (1) calculating magnetic buoyancy force on particles using a 3D analytical model of magnetic field distribution and a nonlinear magnetization model of ferrofluids inside microchannel, (2) deriving and solving governing equations of motion for particles in laminar flow condition using analytical expressions of dominant magnetic buoyancy and hydrodynamic drag forces. Experimental measurements using a Gauss meter confirm the validity of our analytical model of magnetic field distributions.

3.3. Materials and Methods

PDMS microfluidic channel was fabricated through a standard soft-lithography approach as adopted in chapter 2. Figure 8(b) shows a fabricated device used in our study. We used the commercial water-based magnetite ferrofluid (EMG 408, Ferrotec

Co., NH) in our experiments. This ferrofluid was mixed with 0.1% Tween 20 (5% w/w) to prevent potential particles aggregation during experiments. Fluorescent spherical microparticles (4.8 μm, 5.8 μm and 7.3 μm in diameter, Thermo Fisher Scientific Inc., Waltham, MA) were mixed with ferrofluids to observe focusing effects. Flow experiment was conducted on the stage of an inverted microscope (Zeiss Axio Observer, Carl Zeiss Inc., Germany). During experiments, ferrofluid and microparticles mixture into microchannel were maintained at tunable flow rates using a syringe pump (Nexus 3000, Chemyx Inc., Stafford, TX). Two NdFeB permanent magnets were used to produce required magnetic fields for focusing. Saturation magnetizations of both magnets were measured to be 0.8 T by a Gauss meter (Model 5080, Sypris, Orlando, FL) and an axial probe with 0.381 mm diameter of circular active area. The images of particles stream were recorded using a CCD camera (SPOT RT3, Diagnostic Instruments, Inc., Sterling Heights, MI) and analyzed in ImageJ software.

3.4. Results and Discussions

Figure 9 depicts simulation results of distributions of magnetic field and magnetic force within the microchannel, as well as representative trajectories of 4.8 μm microparticles at different flow rates in all three dimensions. For example, surface plot in Figure 9(a) shows magnitude of magnetic fields of x-y plane at $z = 0$ within the channel. From boundaries to center of the channel, magnitude of magnetic fields decays quickly, eventually forming a local magnetic field minimum at center of the channel. Consequently, microparticles experience magnetic buoyancy forces pointing towards the field minimum direction once entering the channel, as shown in Figure 9(b). The force is

computed on a 4.8 μm particle and magnitude of the force is on the order of 1 picoNewton.

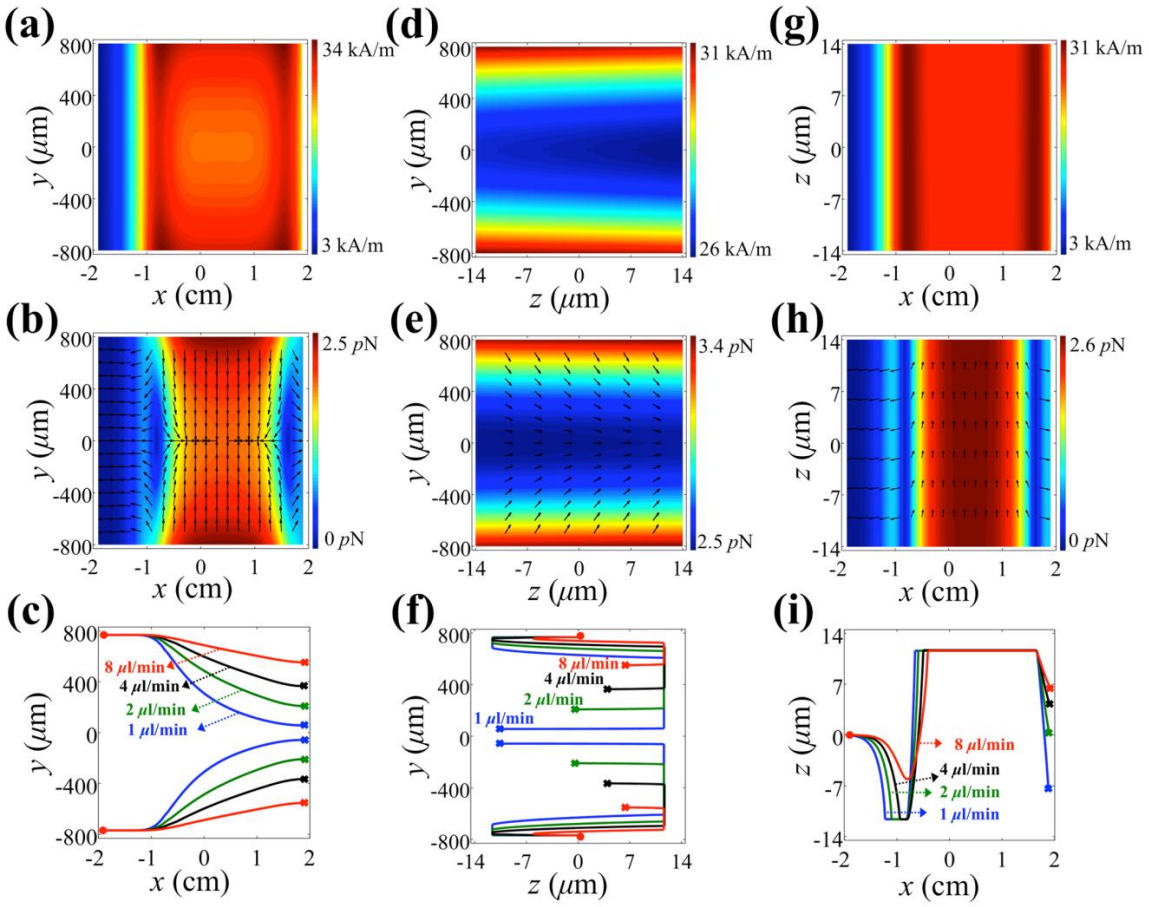

Figure 9. Analytical simulation of magnetic field and force distributions in the microfluidic channel, and trajectories of microparticles (4.8 μm in diameter) at different flow rates. Simulation parameters match experimental conditions. (a)-(c) *x*-*y* plane (z = 0), (d)-(f) *y*-*z* plane (*x* = 0), (g)-(i) *x*-*z* plane (*y* = 0) of magnetic field strength (surface plot) (a, d, g), magnetic force (surface plot: force magnitude; arrow plot: force direction) (b, e, h), and particles' trajectories at different flow rates (c, f, i). Dots indicate starting points, while crosses indicate ending points of particles' trajectories.

Note that magnitude of magnetic buoyancy force can be further increased to nanoNewtons range by replacing current ferrofluids with more concentrated ones, using microparticles with larger diameters, and creating a greater magnetic field gradient. Streams of microparticles can be quickly focused by magnetic buoyancy force towards center of the channel, balanced by hydrodynamic drag force, with a mean speed depending on the applicable flow rates. Figure 9(c) shows relationship between the focusing effect and particle flow rates. Naturally, microparticles are much more focused with slower flow rate, which corresponds to a longer residual time within the channel. The *x*-component of magnetic buoyancy force changes its polarity around the edges of magnets. Microparticles to the left of magnets experience *x*-direction deceleration and move slower than the speed of fluids; particles to the right of the magnet experience *x*-direction acceleration and move faster than the speed of fluids. Figures 9(d)-(f) illustrate distributions of magnetic field and force, as well as trajectories of microparticles of *y*-z plane at $x = 0$ within the channel; Figures 9(g)-(i) illustrate the cases of *x*-z plane at $y = 0$. We extend our previous 2D analytical model into 3D in this work, in part due to the opaqueness of ferrofluids [52] and its negative impact on observation of particles motion. It is a less of a problem when diluted ferrofluids (~1% v/v) and thin microchannel are used. However, with a concentrated ferrofluid (~10% v/v) in a thick microchannel, fluorescent microparticles are visible only when they are very close (~1 μm) to surfaces of the channel. For that reason, we are interested in knowing the motion of microparticles in *z*-direction. It becomes obvious that the relative position of magnets and channel play a dominant role in determining vertical displacements (*z*) of particles. Simulation results from Figures 9(f) and (i) indicate in our current experimental setup all particles were

quickly pushed towards one of the channel surfaces, depending on their locations in *x*-direction. We observed in flow experiments that most of the particles were pushed onto bottom surface of the channel as soon as they entered the channel. Furthermore, our analytical model can enable fast and accurate study of 3D particle focusing effects in microchannels.

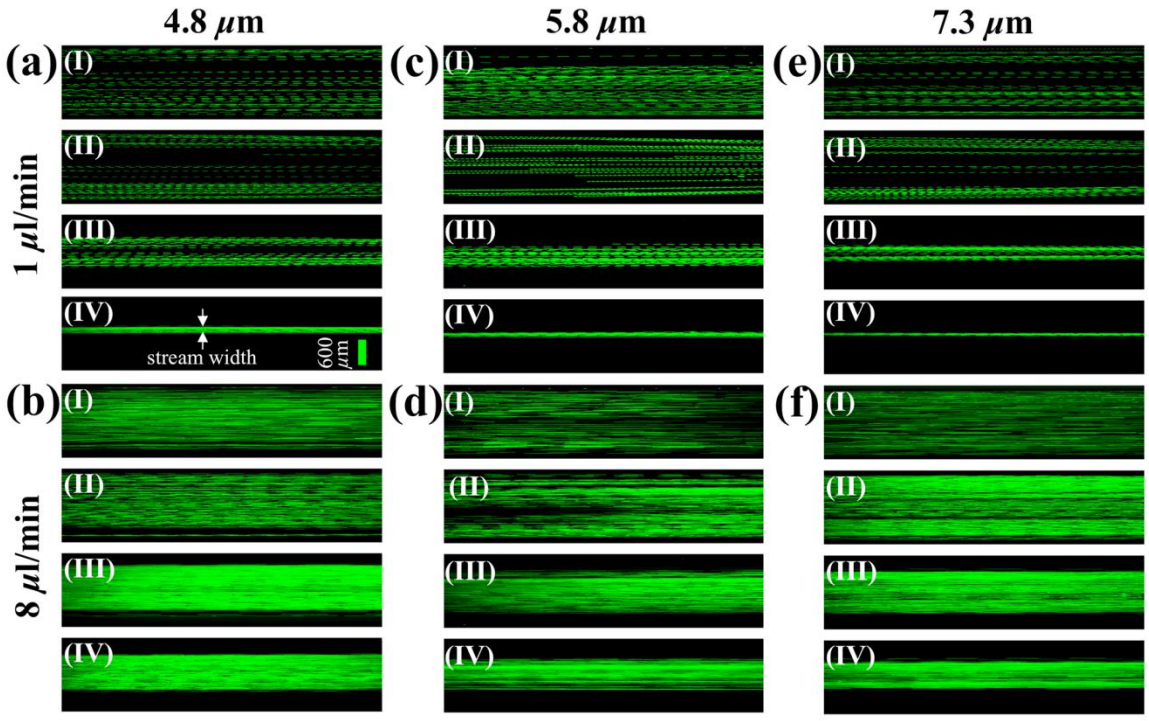

Figure 10. Experimental composite fluorescent images of observation windows (I-IV) for 4.8 μm (a-b), 5.8 μm (c-d), 7.3 μm (e-f) particles at 1 μl/min (a, c, e) and 8 μl/min (b, d, f) flow rates. Widths of particles stream are used to calculate the contraction ratios depicted in Figure 11.

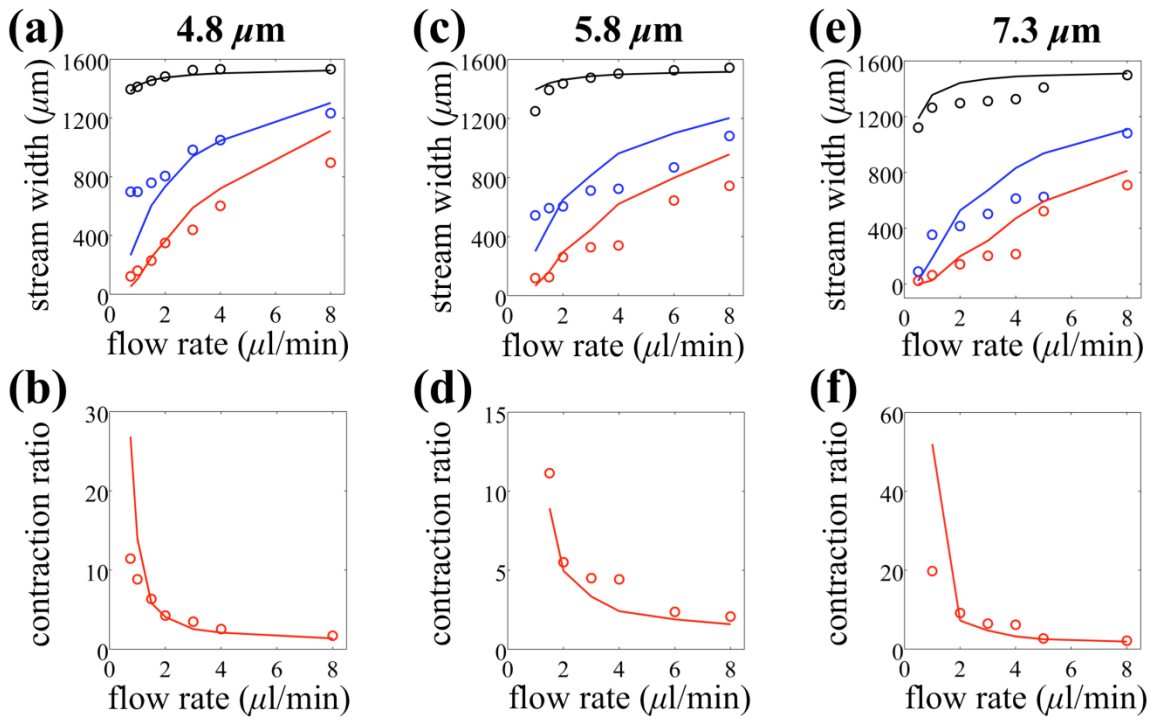

Figure 11. Comparisons of theoretical (solid lines) and experimental (circular marks) stream widths (a, c, e) and contraction ratios (b, d, f) of 4.8 μm (a, b), 5.8 μm (c, d) and 7.3 μm (e, f) particles at various flow rates. Black lines and circles in (a, c, e) correspond to observation region II; blue ones region III; and red ones region IV. The width of particles stream decreases as the particle diameter increases, and as the flow rate decreases. As a result, contraction ratio increases as particle diameter increases, and as flow rate decreases. Discrepancy between theoretical and experimental results may be attributed to combinations of "wall" effect and finite experimental width of particles stream.

Figure 10 shows distributions of fluorescent microparticles (4.8 μm, 5.8 μm and 7.3 μm) that were recorded during the focusing process at two different flow rates (1 μl/min and 8 μl/min) in four different observation windows marked as I, II, III and IV in

Figure 8(c). For example, Figure 10(a) depicts the focusing of 4.8 μm particles at 1 μl/min flow rate. Window I was to the left of permanent magnets, therefore microparticles barely experienced magnetic buoyancy forces in this area, as evident in simulation results of Figure 11(b). Consequently, the distribution of microparticles in this area was uniform across the width of the channel. As microparticles entered the area in which the magnetic buoyancy force becomes dominant (window II), the force exerted on the particles drove them toward the centerline of the channel, where magnetic field minimum existed. As the particles entered window III, they were focused into a narrow stream in the middle of the channel. At window IV, the width of the particle stream was measured to be approximately 200 μm, about one-eighth of the channel width.

As we mentioned earlier, the focusing effect of microparticles is greater with slower flow rate, as demonstrated by experimental comparisons between 1 μl/min and 8 μl/min in Figure 9. We also observed that the focusing effect was dependent upon diameter of the microparticles – the larger the particles, the greater the focusing effect. This dependence can be explained through a simple force analysis. Magnetic buoyancy force is proportional to the volume of the particle, while hydrodynamic viscous drag scales only with the diameter. Therefore, particle migration in the *y*-direction balanced by both magnetic buoyancy and hydrodynamic drag force depends on the square of particle diameter. In order to compare simulation and experimental results, we obtained trajectories of microparticles in a microfluidic system depicted in Figure 11(a) using the 3D analytical model described in previous section. Specifically, we simulated spherical particles with 4.8 μm, 5.8 μm and 7.3 μm diameters in a channel with flow rate varied from 1 to 8 μl/min. Other simulation parameters, including dimensions of channel and

magnets, saturation magnetization of magnets, properties of fluids, were chosen to match the exact experimental conditions. Experimental stream widths were obtained by measuring the width particle stream at windows II, III, and IV in Figure 8(c). Contraction ratio is defined as the width of particles stream in window II over the one in window IV. In Figure 11, predicted stream width and contraction ratio show a reasonable agreement with experimental data, confirming the validity of our analytical model. We do observe slight discrepancy between theoretical and experimental results, which may be attributed to reasons including "wall" effect [106] on motions of the particles and finite width of particles stream obtained from record images.

CHAPTER 4

CONTINUOUS SEPARATION OF NON-MAGNETIC PARTICLES INSIDE FERROFLUIDS

4.1. Introduction

In this chapter, we demonstrate the development of a novel microfluidic device that can continuously separate non-magnetic microparticles based on their sizes inside water-based ferrofluids with the use of a simple permanent magnet. Our approach adopts a continuous flow configuration thus can achieve a higher (e.g, ~10^5 particles/hour) throughput. The device fabrication only needs a simple soft lithography step [71] and doesn't require microfabricated micromagnets or current-carrying electrodes, which significantly increase the cost associated with the device. The operation of the device is straightforward and the resulting separation efficiency of large particles from poly-dispersed particles mixture is 100%.

4.2. Working Mechanism

The dynamics of a non-magnetic microparticle inside a ferrofluid-filled microfluidic channel is determined primarily by the balance of the hydrodynamic viscous drag and the magnetic buoyancy force on that particle as analyzed in chapter 2. Given the magnitude of the magnetic fields in our experiments, gravitational force and buoyancy force are second order and therefore not important. When the non-magnetic particles are sufficiently small, Brownian motion and diffusion will start to affect the motion of the particles. A criterion developed by Gerber *et al.* [107] can be used to estimated the critical

diameter, which in our case is on the order of 10 nm, much smaller than the diameters of large particles used in our experiments. Therefore, diffusion effect of large particles inside ferrofluids can be neglected. For small particles (< 1 μm diameter) in ferrofluids, diffusion needs to be considered.

When an external magnetic field gradient is applied, the non-magnetic particles inside ferrofluids experience both magnetic and hydrodynamic drag forces, $\mathbf{F}_m$ and $\mathbf{F}_d$. In the cases of diluted ferrofluids or an intense applied magnetic field, the magnetic buoyancy force on a non-magnetic particle inside ferrofluids can be expressed as [52]

$$\mathbf{F}_m = -V\mu_0(\mathbf{M}\cdot\nabla)\mathbf{H}$$

where V is the volume of the non-magnetic particle and μ_0 is the permeability of free space. **M** is the effective magnetization of the ferrofluid and **H** is the applied magnetic field. The presence of the minus sign in front of the term indicates the non-magnetic particle immersed in ferrofluids experiences a force in the direction of the weaker magnetic field. The effective magnetization of ferrofluid **M** is related to the magnetization of ferrofluid $\mathbf{M}_f$ through a "demagnetization" factor, which accounts for the shape-dependent demagnetization of the concentrated ferrofluid by the presence of the non-magnetic particle. EMG 408 ferrofluid used in our experiments is very diluted, therefore we assume the "demagnetization" field is small enough so that **M** equals to $\mathbf{M}_f$.

We take the hydrodynamic drag on a non-magnetic particle in ferrofluids to be the Stokes drag,

$$\mathbf{F}_d = 3\pi\eta D(\mathbf{v}_f - \mathbf{v}_p)f_D$$

where η is the viscosity of the ferrofluid, D is the diameter of the spherical particle, and $\mathbf{v}_f$ and $\mathbf{v}_p$ are the velocity vectors of the ferrofluid and the particle, respectively. f_D is the hydrodynamic drag force coefficient. Its appearance indicates the increased fluid viscosity the large non-magnetic particle experiences as it moves near the microfluidic channel surface [78, 79, 106].

$$f_D = \left[1 - 0.6526\left(\frac{D}{D+2z}\right) + 0.1475\left(\frac{D}{D+2z}\right)^3 - 0.131\left(\frac{D}{D+2z}\right)^4 - 0.0644\left(\frac{D}{D+2z}\right)^5\right]^{-1}$$

where z is the distance between the bottom of the particle and the channel surface.

4.3. Materials and Methods

We used the commercial ferrofluid (EMG 408, Ferrotec Co., Bedford, NH) for the separation experiments. Different sizes (1 μm, 1.9 μm, 3.1 μm and 9.9 μm diameters) of green fluorescent polystyrene spherical microparticles (Thermo Fisher Scientific Inc., Waltham, MA) with a density of 1.05 g/cm^3 were used. The coefficient of variation (the ratio of the standard deviation to the mean) of the microparticle diameters was less than 5%. In order to obtain the target particle concentrations (~10^6 particles/cm^3) in ferrofluids, the fluorescent particles suspension was first diluted with DI water containing 0.1% Tween 20 to prevent particle aggregation. For 1 μm and 1.9 μm particles, the initial concentrations were relatively high; the diluted particle suspensions were diluted again with EMG 408 ferrofluids to achieve target concentrations (1 μm, 1.8×10^6 particles/cm^3; 1.9 μm, 2.6×10^6 particles/cm^3). For 3.1 μm and 9.9 μm particles, the initial concentrations were relatively low; the diluted particle suspensions were centrifuged, decanted then mixed with EMG 408 ferrofluids to achieve target concentrations (3.1 μm, 6.0×10^6 particles/cm^3; 9.9 μm, 1.9×10^6 particles/cm^3).

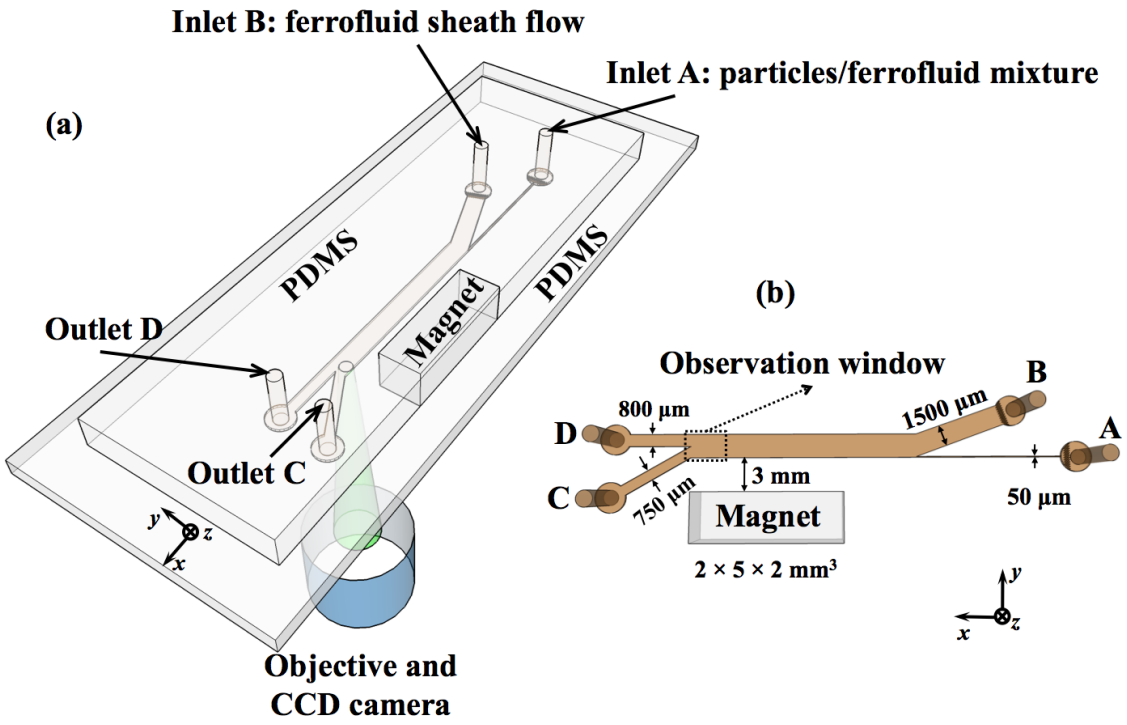

Figure 12. (a) Schematic representation of the separation mechanism and the experimental setup. Non-magnetic microparticles and ferrofluid mixture were introduced into the microfluidic channel (20 µm in thickness) Inlet A and hydrodynamically focused by the ferrofluid sheath flow from Inlet B. Upon entering the separation region (near the permanent magnets), deflection of microparticles from their flow paths occurred because of the non-uniform magnetic field produced by permanent magnets. We used a stack of four magnets in our experiments. Here we only drew one for simplicity. The motion of the microparticles was imaged from the observation window through a 5× objective and a CCD camera. Particle samples collected from outlets C and D were analyzed for size distribution. (b) The dimensions of the microfluidic channel and the magnets, and the location of the observation window.

A schematic of a prototype microfluidic separation device is shown in Figure 12(a). Non-magnetic microparticles mixed with water-based ferrofluids were introduced into the microfluidic channel and hydrodynamically focused by the ferrofluid sheath flow. Once entering the separation region, deflections of non-magnetic particles from their flow paths occurred because of the magnetic buoyancy forces on them under non-uniform magnetic fields. Particles of larger size experienced more magnetic forces than smaller ones. This is because magnetic buoyancy forces are proportional to the volume of the particles. The hydrodynamic drag force, on the other hand, scales with the diameter of the particles. As a result, larger particles were deflected more than small ones. This phenomenon can be used to continuously separate non-magnetic particles inside ferrofluid based on their sizes.

The PDMS microfluidic device was fabricated and operated through the same procedure as described previously. Before liquid injection, the completed device was exposed again to plasma for 10 minutes to keep the surfaces hydrophilic. Triton X-100 solution was injected into the channel using a syringe pump (KDS 101, KD Scientific, Holliston, MA). The solution was kept in the channel for 20 minutes then purged with N_2 gas. This step ensured that the polystyrene particles would not attach to PDMS surfaces during experiment. The microfluidic channel was afterwards filled with air-bubble free EMG 408 ferrofluid. During experiments, ferrofluid injection into Inlet B was maintained at 10 µL/minute using a syringe pump (KDS 101, KD Scientific, Holliston, MA). Ferrofluid and particles mixture was injected into Inlet A at 3 µL/min using a second syringe pump (Nexus 3000, Chemyx Inc., Stafford, TX). The ferrofluid and particles mixture stream was focused before entering the separation region. A non-uniform

magnetic field was generated by a stack of four NdFeB permanent magnets. Each magnet is 2 mm in width, 5 mm in length and 2 mm in thickness. The magnet stack was placed 3 mm away from microfluidic channel as indicated in Figure 12(b). The magnetic flux density at the center of the magnets' pole surface was measured to be 0.47 T by a Gauss meter (Model 5080, Sypris, Orlando, FL) and an axial probe with 0.381 mm diameter of circular active area. The images of fluorescent particles were recorded through a fluorescent filter set (41001 FITC, Chroma Technology Corp., Rockingham, VT) and a 5× objective with a CCD camera (SPOT RT3, Diagnostic Instruments, Inc., Sterling Heights, MI). Particle samples collected from Outlets C and D (see Figure 12(b)) were analyzed for size distribution in order to quantitatively evaluate the separation efficiency of this approach. ImageJ® software was used to count the particles.

4.4. Results and Discussion

In the experiment with 1 μm diameter and 9.9 μm diameter fluorescent microparticles, we introduced the microparticles mixture (~10^6 particles/cm^3 concentration for both particles) into the microfluidic channel Inlet A at a constant flow rate of 3 μl/min. The mixture was hydrodynamically focused into a very narrow stream by the sheath flows from Inlet B at a constant flow rate of 10 μl/min. Before the non-uniform magnetic field was applied, small particles and large particles were observed to flow together near the sidewall of the channel, as shown in Figure 13(a). Due to the opaqueness of the ferrofluid, the particles were only visible when they were very close to the bottom surface of the channel. Because the thickness of the microfluidic channel was 20 μm, large particles (9.9 μm diameter) became more visible than small particles (1 μm diameter) in fluorescent mode. The particles appeared to be line segments instead of dots

because of the CCD camera's exposure time and high flow speed (2.1 mm/s) in the channel.

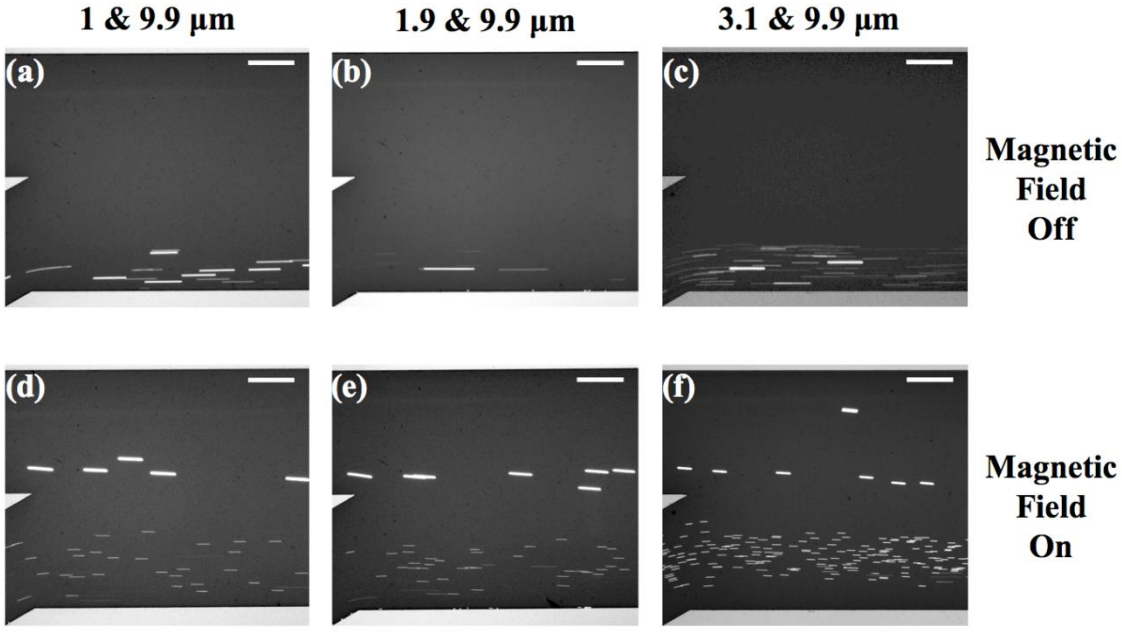

Figure 13. Experimental top view of the observation window. (a) – (c) were the recorded fluorescent images of particles mixture motions ((a): 1 µm and 9.9 µm particles; (b): 1.9 µm and 9.9 µm particles; (c): 3.1 µm and 9.9 µm particles) before the magnetic field is applied. (d) – (f) were the images after the magnetic field was applied. The scale bars represent 300 µm.

Once the magnetic field was applied, magnetic buoyancy forces deflected the microparticles from their flow paths, as shown in Figure 13(d). The magnetic buoyancy force on large particles was greater than those acting on the small particles, deflecting the large particles out of the particles mixture and toward Outlet D. The magnetic buoyancy forces on small particles were inadequate to deflect them into Outlet D; therefore they

exited the channel through Outlet C. This resulted in the spatial separation of these two particles at the end of the separation region. Both small and large particles were visible in fluorescent mode after the magnetic field was applied. This was because the permanent magnets produced a weak but non-zero *z*-direction magnetic field, which effectively pushed all non-magnetic particles in ferrofluid down to the bottom surface of the microfluidic channel. We were able to separate ~10^5 9.9 μm particles from ~10^5 1 μm particles per hour with the aforementioned flow rates. Figure 13(b) and Figure 13(e) depicts the separation of 1.9 μm diameter and 9.9 μm diameter particles. Figure 13(c) and Figure 13(f) depicts the separation of 3.1 μm diameter and 9.9 μm diameter particles. The separation throughputs were both on the order of 10^5 particles/hour. Noted that the separation throughput can be further increased by tuning the experimental parameters (increasing the flow rates of the particles/ferrofluid mixture and magnetic field strength, gradient). Given a range of particle sizes, the resolution of this separation approach is directly related to the difference in the particles' *y*-direction deflection (see Figure 12(b)) towards the Outlets. Ideally, the resolution of separation could be arbitrarily small. However, particle streams have a finite width in the separation region of the channel due to the device design and their small but non-zero diffusions in ferrofluids. The difference in the particles' *y*-direction deflections needs to be larger than the width of the small particles' stream in order for the separation approach to be useful. A future work for this study is to optimize the microfluidic channel design such that the width of the particles' stream inside ferrofluids is much smaller compared to the current design. The separation resolution of this approach can be further increased as a result. Non-magnetic particle separation within ferrofluids works as long as particles are much larger than the magnetic

nanoparticles and the average spacing between them. Non-magnetic particles with the diameter on the order of 10 nm will tend to get lodged between the magnetite nanoparticles instead of being pushed when an external field is applied. Therefore the size of target non-magnetic particles for this separation method to work needs to be much larger than 10 nm. Currently, the smallest particles' diameter we can separate using this approach is 1 μm. Non-magnetic particles inside ferrofluid without any flow are prone to chaining and clustering under magnetic fields [43]. However, the chaining and clustering effects appeared to be minimal in our separation device, possibly due to the fact the flow speed in our device was high enough so that the shear force was able to prevent the particles aggregate from forming.

To precisely evaluate the separation efficiency of this approach, the separated particle samples were collected from the Outlet C and D and analyzed for size distribution off chip. ImageJ® software was used to count the number of the particles from both outlets. In our experiments, a mixture of particles with different sizes was eventually separated into Outlet C and D. We defined the remaining efficiency as the ratio of the number of the particles (e.g., 1 μm particles) exiting from Outlet C after magnetic field application to their corresponding number before magnetic field application. Similarly, separation efficiency was defined as the ratio of the number of the particles (e.g., 9.9 μm particles) exiting from Outlet D after magnetic field application to their corresponding number before magnetic field application. Figure 14(a) shows a representative fluorescent image of the polydispersed particles mixture (1 μm and 9.9 μm) collected from Inlet A before separation. When the focused particles stream was introduced into the separation region of our device, virtually all

small particles remained close to the sidewall of the channel and exited the device through Outlet C (see Figure 14(b), particle sample collected from Outlet C after magnetic field application), and virtually all large particles were observed to migrate into Outlet D (see Figure 14(c), particle sample collected from Outlet D after magnetic field application). The remaining and separation efficiencies for both particles are shown in Figure 14(d). 100% of small particles exited through Outlet C, and 100% of large particles migrated into Outlet D. Figure 14(e) – 14(h) and Figure 14(i) – 14(l) depict the images and efficiencies for 1.9 μm/9.9 μm mixture separation and 3.1 μm/9.9 μm mixture separation, respectively. The separation efficiencies of large particles for both mixtures were 100%, while the remaining efficiencies of small particles were 98.9% for 1.9 μm particles and 97.2% for 3.1 μm particles. As the difference between particle sizes becomes smaller, the difference in the magnitude of the magnetic buoyancy forces on the particles will decrease accordingly, which leads to smaller difference in the spatial separation.

Compared to the existing ferrofluid based [48, 70] or magnetic aqueous solution based [61] particle separation technique, our approach offers the following advantages: (i) the particle separation throughout (~10^5 particles/hour) is high, and it is possible to increase the throughput further by increasing the flow rates and magnetic fields; (ii) the separation efficiency of our approach is comparable or higher than the efficiencies of existing techniques; (iii) the device fabrication is low cost and does not require microfabricated electrodes or micromagnets; (iv) the separation system is simple and only requires the microfluidic device and a stack of permanent magnets. Some of the limitations of this approach include: (i) ferrofluids are opaque, thus making the particle

motion recording and sample analysis difficult; (ii) high flow rates within the device may have a negative effect on the biological entities such as cells if this approach is adopted for biological applications.

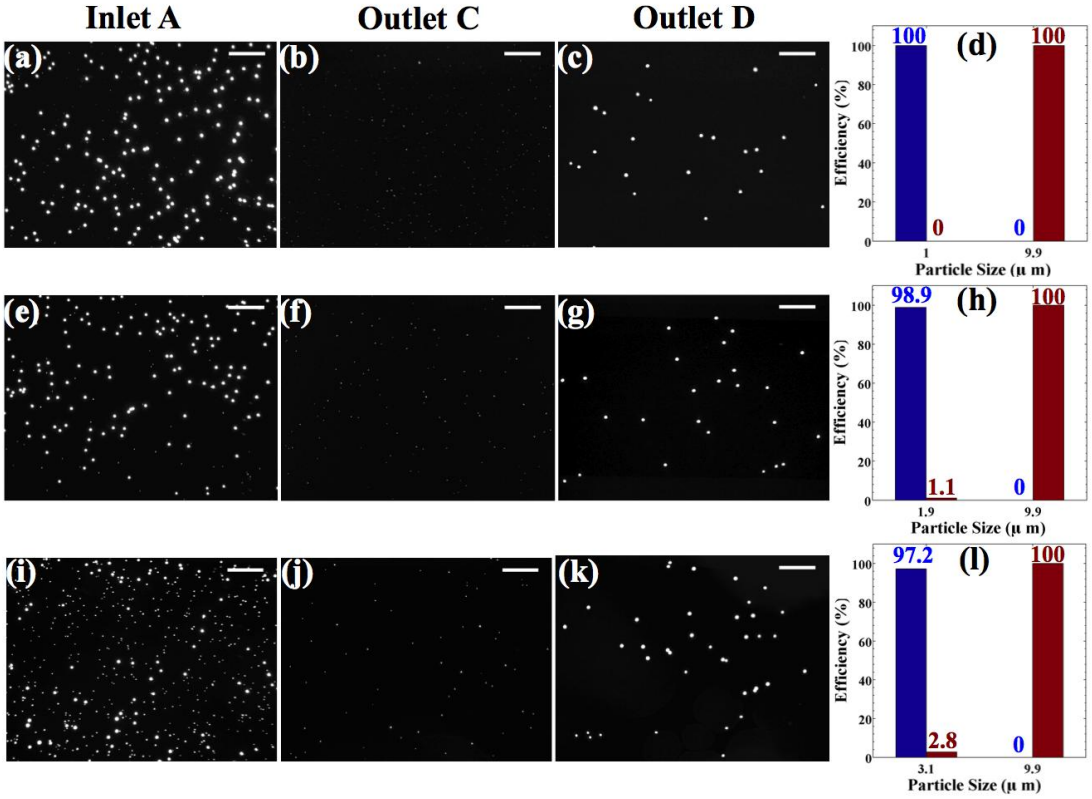

Figure 14. Representative fluorescent images of particles mixture collected before separation (at Inlet A) and after separation (at Outlets C and D), and the particles remaining and separation efficiencies. (a) – (d) were for 1 μm and 9.9 μm particles mixture; (e) – (h) were for 1.9 μm and 9.9 μm particles mixture; (i) – (l) were for 3.1 μm and 9.9 μm particles mixture. Blue bar indicates the remaining efficiency, while the red bar indicates the separation efficiency of particles after passing through the separation region. The scale bars represent 300 μm.

CHAPTER 5

CONTINUOUS SEPARATION OF BACTERIA AND YEAST CELLS

5.1. Introduction

In applications of cell manipulation, the purpose of using ferrofluids is to induce effective magnetic dipole moments within cells. Under non-uniform magnetic fields, cells will experience in the weaker field direction a magnetic buoyancy force, analogous to buoyancy force, as the magnitude of the force is proportional to the volume of the cell [39]. Many groups have been working on adapting this principle to particles and cells sorting. For example, Whitesides' group separated synthetic particles according to their densities' difference using paramagnetic salt solutions [61, 62]. Pamme's group demonstrated continuous particle and cell manipulation using paramagnetic salt solution in microfluidic devices [55, 108]. Xuan's group studied the transport of particles in both paramagnetic solutions and ferrofluids through a rectangular microchannel embedded with permanent magnets [57, 109]. Park's group recently sorted human histolytic lymphoma monocytes cells from red blood cells using gadolinium diethylenetriamine pentaacetic acid (Gd-DTPA) solution [110]. Koser's group was able to use an integrated microfluidic platform for sorting microparticles and live cells within a citrate stabilized cobalt-ferrite ferrofluid in static flow conditions [48]. The same device was also applied to continuous-flow frequency-adjustable particles separation [111]. Our group developed high-efficiency and high-throughput continuous-flow particle separation and focusing devices using commercial ferrofluids and hand-held permanent magnets [66, 69, 112]. Permanent magnet based devices

are low-cost and easy to operate; their operations do not generate heat. Magnetic fields produced by permanent magnets are substantially larger than the ones by current-carrying electrodes.

High throughput, label-free and selective cell sorting realized in a single automated device can have profound impacts on environmental monitoring, diagnostics and therapeutics. Although continuous-flow ferrohydrodynamic sorting has been demonstrated with microparticles, it has not previously been reported with live cells [66]. The potential for live cell applications of continuous-flow ferrohydrodynamic sorting motivates the study presented here. We developed a microfluidic device that could continuously sort cells of different sizes based on ferrohydrodynamics, which involved manipulation of cells within ferrofluids via external non-uniform magnetic fields. When cell mixtures and ferrofluids were injected into the channel by a pressure-driven flow, deflections of cells from their laminar flow paths would occur because of the magnetic field gradient and resulting magnetic buoyance force. This deflection will lead to spatial separation of cells of different sizes at the end of channel.

In the following sections, we first summarize results from a three-dimensional theoretical study of cells' transport in the microfluidic device, followed by materials and methods used in this study. Cell viabilities of *Escherichia coli* and *Saccharomyces cerevisiae* in the commercial ferrofluid are then discussed. Afterwards, calibration of the sorting device with fluorescent polystyrene microparticles is performed. *Escherichia coli* and *Saccharomyces cerevisiae* are sorted in the device, and cells distribution is analyzed on samples collected from channel outlets. We also address the cell visibility issues by applying both bright field and fluorescent microscopy.

5.2. Theory and Simulation

In previous Chapters, we reported both two-dimensional (2D) and three-dimensional (3D) analytical models for microfluidic transports of microparticles in ferrofluids [69, 112]. In this work, we applied the 3D analytical model to predict cells' sorting in permanent magnet based device. We obtained cells' trajectories by first calculating magnetic buoyancy force on cells using a 3D analytical model of magnetic fields [77] and a nonlinear magnetization model of ferrofluids [39], and then solving governing equations of motion for cells in laminar flow condition [84]. All relevant parameters used in our simulation are listed in Figure 15 and Materials and Methods section. In addition, we calculated volume of a single rod-shape *Escherichia coli* cell with short axis of 0.5 – 1 μm and long axis of 2 – 4 μm to be 2.1 – 16.7 μm^3 [113], and volume of a single sphere-shape *Saccharomyces cerevisiae* cell with diameter of 7 – 9 μm to be 180 – 382 μm^3 [114].

Figure 15 summarizes simulated distribution of magnetic fields and magnetic buoyance forces in the sorting channel, as well as 3D trajectories of *Escherichia coli* and *Saccharomyces cerevisiae* cells. The surface plot in Figure 15(a) shows magnitude of magnetic fields of *x*-*y* plane at $z = 0$. Magnetic fields decayed rather quickly from the surface of the magnet and formed a gradient that resulted in magnetic buoyance force on cells in both *x* and *y* directions, as indicated in Figure 15(b). Consequently, cells experiencing such force when entering the sorting channel would decelerate in *x* direction and accelerate in *y* direction. Force computed on a spherical microparticle of 7.3 μm diameter, with its total volume (~200 μm^3) close to that of a single *Saccharomyces cerevisiae* cell, is on the order of 10 *p*N.

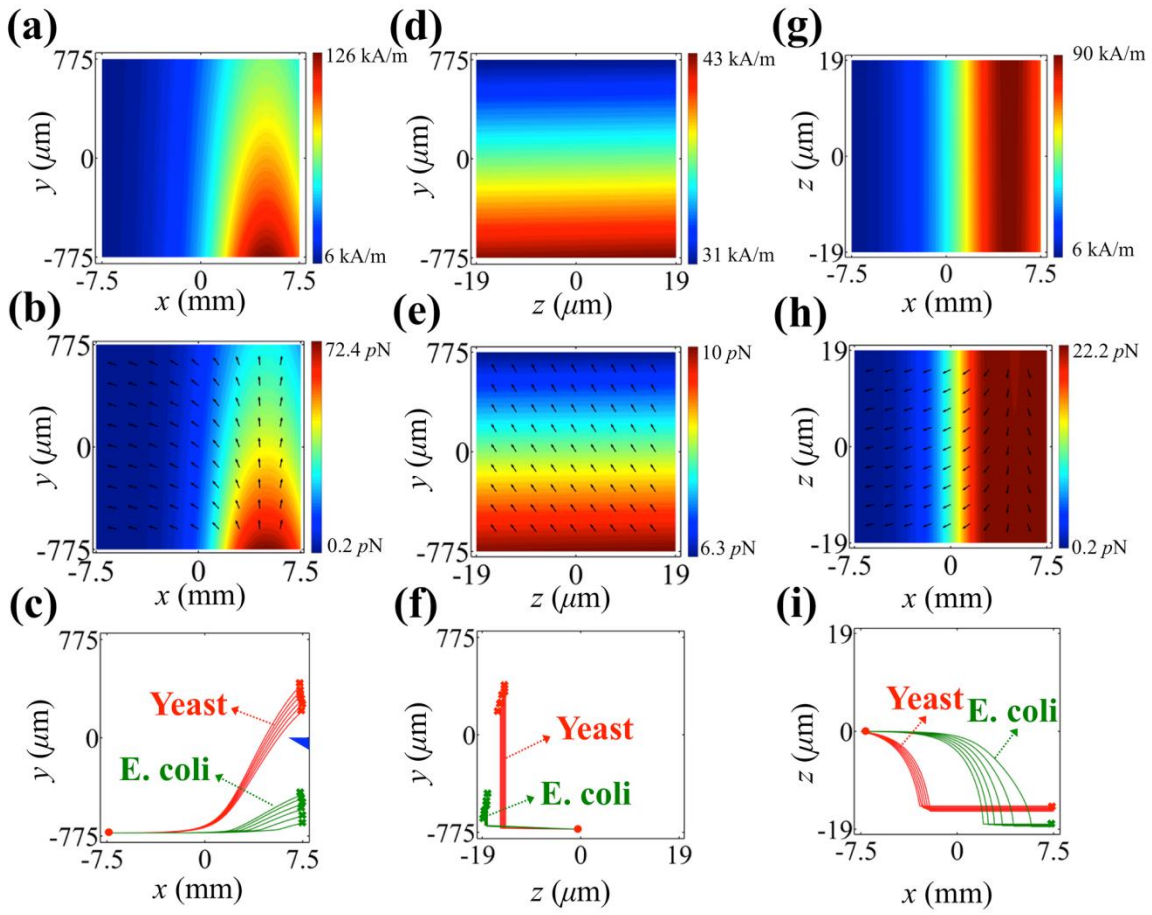

Figure 15. Analytical three-dimensional simulation of magnetic field and force distributions in microfluidic channel, and trajectories of cells. Simulation parameters match exact experimental conditions. (a)-(c) *x*-*y* plane ($z = 0$), (d)-(f) *y*-*z* plane ($x = 0$), (g)-(i) *x*-*z* plane ($y = 0$) of magnetic field strength (surface plot) (a, d, g), magnetic force (surface plot: force magnitude; arrow plot: force direction) (b, e, h), and particles' trajectories (c, f, i). Dots indicate starting points, while crosses indicate ending points of cells' trajectories. *E.coli* cell has volume range of 2.1 – 16.7 μm^3 and Yeast cell has volume range of 180 – 382 μm^3, resulting in a distribution of trajectories for each type of cell. Blue triangle in (c) indicates boundary between Outlets C and D. Dots indicate starting points, while crosses indicate ending points of cells' trajectories.

For comparison, buoyant force on the same particle is calculated to be 0.04 *p*N, considering the difference between particle and ferrofluid densities (particle: 1050 kg/m^3, ferrofluid: 1070 kg/m^3). Its magnitude is about 1000 times smaller than magnetic buoyance force. Cell mixtures were quickly sorted by magnetic buoyancy force towards the end of channel, as shown in Figure 15(c) with simulated cells' trajectories considering their natural size variations. All *Escherichia coli* cells, having much smaller size and volume compared to *Saccharomyces cerevisiae* cells, exited the channel through Outlet D, while all *Saccharomyces cerevisiae* cells migrated towards Outlet C. Figures 15(d)-(f) illustrate distribution of magnetic fields and forces, as well as trajectories of cells of *y*-z plane at $x = 0$; Figures 15(g)-(i) depict the cases of *x*-z plane at $y = 0$. We are interested in 3D trajectories of cells, in part due to the opaqueness of ferrofluids and difficulty in recording cells' weak fluorescence in the channel, especially the red fluorescent from *Saccharomyces cerevisiae* cells, as shown later in the results. In a concentrated ferrofluid (~10% v/v), particles and cells are visible only when they are very close (~1 μm) to the surface of channel [69]. Visibility was a less of a problem when diluted ferrofluids (~1% v/v) and thin microchannel were used in our device. Simulation results from Figures 15(f) and (i) indicated in our current setup all cells were pushed towards the channel bottom surface, which would enhance visibility of stained cells.

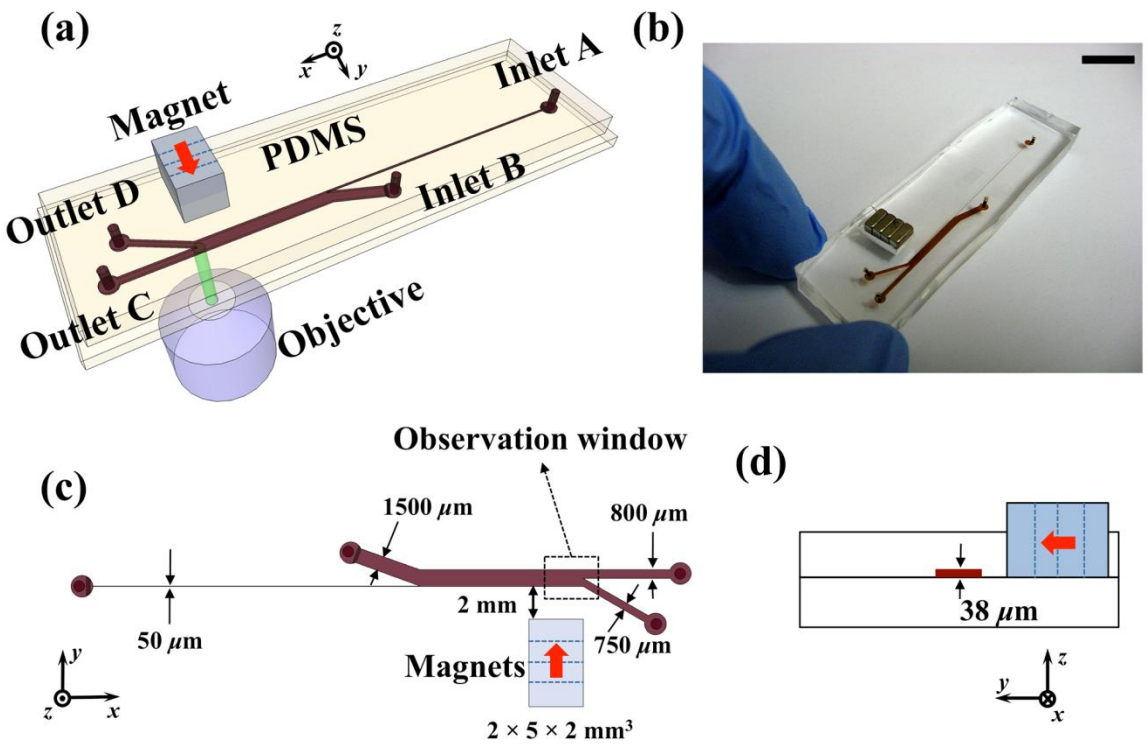

Figure 16. (a) Schematic representation of the sorting device with permanent magnets and a microfluidic channel. (b) An image of prototype device. Scale bar is 10 mm. (c) Topview of the device and relevant dimensions. Red arrows indicate direction of magnets' magnetization. (d) Cross-section of the device.

5.3. Materials and Methods

The prototype polydimethylsiloxane (PDMS) microfluidic device was illustrated in Figures 16(a) and (b). A stack of four NdFeB permanent magnets was embedded into PDMS channel with their magnetization direction vertical to the channel during curing stage. Each magnet is 5 mm in width, 5 mm in length and 2 mm in thickness. The magnet stack was placed 2 mm away from the channel. Flux density at the center of magnet stack's surface was measured to be 470 mT by a Gauss meter (Model 5080, Sypris, Orlando, FL) and an axial probe with 0.381 mm diameter of circular active area. Before

liquid injection, the device was treated with plasma for 10 minutes to render PDMS surfaces hydrophilic. This step ensured both cells and microparticles would not attach onto PDMS surfaces during sorting.

We chose to use EMG 408 ferrofluid in live cells sorting, because of its balance between good biocompatibility, reasonable transparency under both fluorescent and bright-field modes microscopy, and moderate magnetic properties. *Escherichia coli* (strain MG1655) and *Saccharomyces cerevisiae* (Baker's yeast), and two fluorescent microparticles (green 1.0 μm diameter, Thermo Fisher Scientific Inc., Waltham, MA, and red 7.3 μm diameter, Bangs Laboratories Inc., Fishers, IN) were used in sorting. Ferrofluid and particles/cells mixture injected into microchannel were maintained at tunable flow rates using a syringe pump (Nexus 3000, Chemyx Inc., Stafford, TX). Sorting was conducted on the stage of an inverted microscope (Zeiss Axio Observer, Carl Zeiss Inc., Germany). Micrographs of cells and particles were recorded through either a green fluorescent filter set (41001 FITC, Chroma Technology Corp., Rockingham, VT), or a red filter set (43HE, Carl Zeiss Inc., Germany), and a CCD camera (SPOT RT3, Diagnostic Instruments, Inc., Sterling Heights, MI). Cell samples collected from channel outlets were pipetted onto microscope slides and analyzed using a high-resolution CCD camera (AxioCam HR, Carl Zeiss Inc., Germany) for size distributions to quantitatively evaluate efficiency of this approach. ImageJ® software was used to count the number of cells.

Saccharomyces cerevisiae (Baker's yeast) cells were first grown in a 10 ml test tube containing 2 ml of YPG medium (10 g/l yeast extract, 20 g/l glucose, 20 g/l glucose) overnight. They were then transferred into a 100 ml shake flask containing 20 ml of YPG

medium. After 4 h growth at 30°C and 250 rpm, cells in the flask were stained with fluorophores. *Escherichia coli* (strain MG1655) cells were first grown in a 10 ml test tube containing 2 ml of Luria-Bertani (LB) medium overnight. They were then transferred into a 100 ml shake flask containing 20 ml of LB medium (25 g/l LB). After 4 h growth at 37°C and 250 rpm, cells were stained with fluorophores. Nucleic acid stains SYTO9 (green) and SYTO17 (red) (Molecular Probes Inc., Eugene, OR) were used in cell staining.

To study of viability of *Escherichia coli* and *Saccharomyces cerevisiae* cells exposed to EMG 408 ferrofluids, nominally 2×10^9 cells *Escherichia coli* and 2×10^7 cells *Saccharomyces cerevisiae* grown as described above were centrifuged twice at 4°C and washed in defined M9 medium (6.78 g/l Na_2HPO_4, 3.0 g/l KH_2PO_4, 0.5 g/l NaCl, 1.0 g/l NH_4Cl) without carbon source. For either cell type in duplicate, the washed cell pellet from centrifugation was combined with either 2 ml of EMG 408 ferrofluid or 2 ml M9 medium as a control. After 2 hours of incubation at room temperature in these fluids, cell density was determined in triplicate using standard microbial serial dilutions (10^6 dilution for *Escherichia coli*, and 10^4 dilution for *Saccharomyces cerevisiae*), with the transferring of known volumes to Petri plates and counting of Colony Forming Units (CFU) after 24 hours.

5.4. Results and Discussions

5.4.1. Cell Viability

Figure 17(a) shows the CFU in both M9 medium and EMG 408 ferrofluids after incubation. Counts of CFU for each case were averaged over 3 plates and plotted in Figure 17(b). We observed a slight increase in cell density after 2 hours of incubation in

the ferrofluid compared to the M9 medium control for both cell types, suggesting a possibility that either the EMG 408 ferrofluid acted as a cell protectant or the cells continued to grow in this ferrofluid during incubation. Nonetheless, this ferrofluid was not detrimental to the viability of both cell types after 2 hours of exposure, which allowed enough time to carry out the sorting procedure.

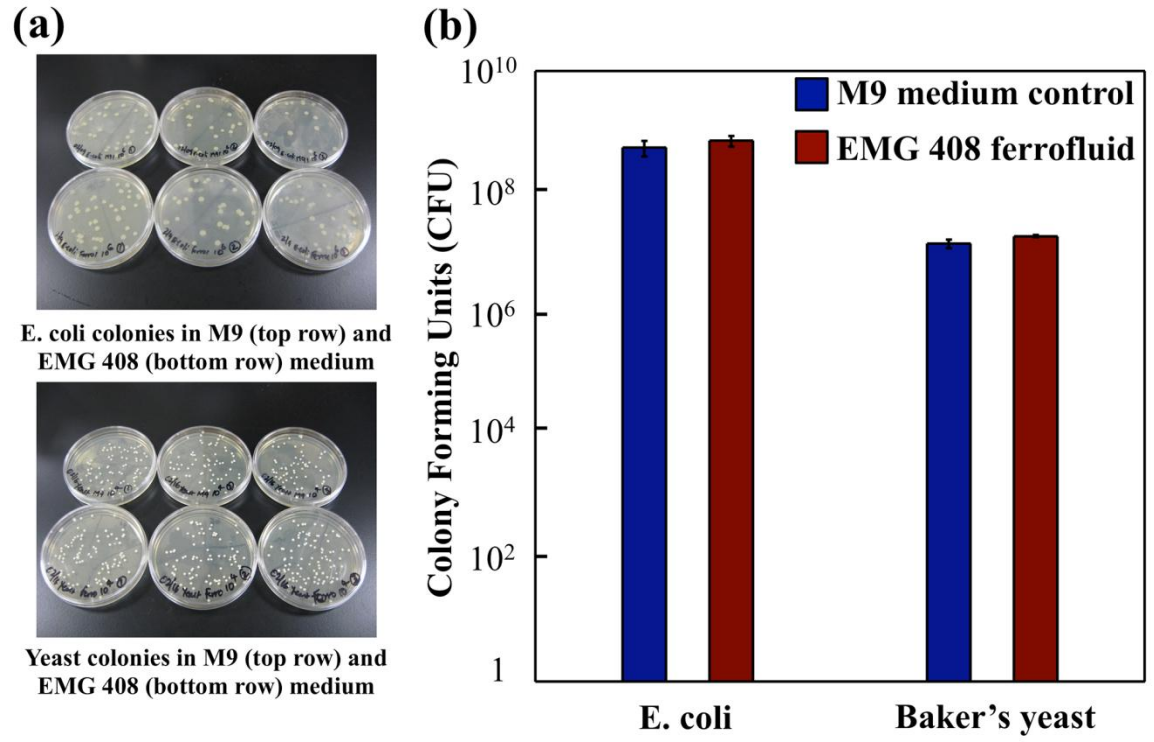

Figure 17. Cell viability test of *Escherichia coli* and *Saccharomyces cerevisiae*. (a) Top and bottom photos show *Escherichia coli* and Yeast colonies formed in M9 medium and EMG 408 ferrofluids after 10^6 dilution from initial growth, respectively. (b) Colony Forming Units (CFU) count of *Escherichia coli* and *Saccharomyces cerevisiae* using initial growth cell concentration.

5.4.2 Cells Sorting

We first calibrated the sorting device using a mixture of *Escherichia coli* cells and red fluorescent 7.3 μm particles, which have similar total volume of *Saccharomyces cerevisiae* cells. Washed *Escherichia coli* cell pellet from centrifugation as described above was stained with 1 μl of green nucleic acid stain SYTO9. Both particles and cells have concentrations of ~10^7 counts/ml. We introduced microparticles/cells mixture into microfluidic channel Inlet A at a constant flow rate of 1.5 μl/min. The mixture was hydrodynamically focused into a narrow stream by sheath flow from Inlet B at a flow rate of 6 μl/min. The observation window was located right before the channel outlets, as indicated in Figure 16(c). When magnetic fields were not present, particles and cells were observed in fluorescent mode flowing together near sidewall of the channel and exiting through Outlet D, as shown in composite micrograph of Figure 18(a). When magnetic fields were present, magnetic buoyancy forces deflected particles from their laminar flow paths towards Outlet C, as shown in Figure 18(b). On the other hand, forces on smaller *Escherichia coli* cells were inadequate to deflect them to Outlet C; therefore they exited the channel through Outlet D still, as shown in Figure 18(c). This resulted in spatial separation of particles/cells mixture at the end of channel. We were able to separate ~10^6 particles from ~10^6 cells per hour with 1.5 μl/min flow rate. Simply increasing the flow rate can further increase sorting throughput. Current microfluidic sorting schemes use flow rates ranging between ~10 μl/min and ~1 ml/min [9]. With such flow rates and 10^7 – 10^8 cells/ml concentration, maximum sorting throughput of our device in theory can go up to 10^9 cells per hour. Increasing the flow rate will increase overall cell sorting throughput, at the same time it will decrease cell sorting efficiency if same device

geometry is used. It is because now cells of large sizes do not have enough time in the channel to be fully deflected and separated from cells of smaller sizes. A possible way to increase both cell sorting throughput and efficiency is to apply high flow rates and use longer channels.

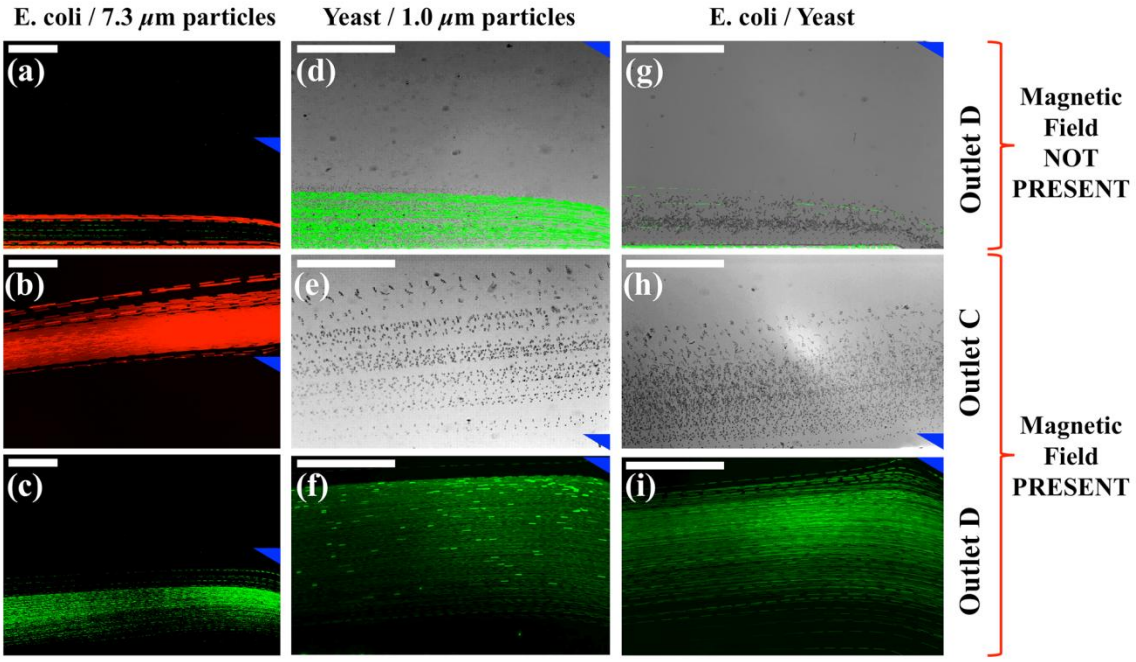

Figure 18. Experimental composite micrographs of sorting process. (a), (d), (g) were particles/cells mixture ((a): *Escherichia coli* (green) and 7.3 μm particles (red); (d): *Saccharomyces cerevisiae* (red and bright-field) and 1.0 μm particles (green); (g): *Escherichia coli* (green) and *Saccharomyces cerevisiae* (red and bright-field) before magnetic fields were applied. (b), (e), (h) were micrographs of Outlet C after magnetic fields were applied, and (c), (f), (i) were micrographs of Outlet D. Blue triangles indicate boundary between Outlets C and D. Scale bars represent 200 μm.

Secondly, we calibrated the device using a mixture of *Saccharomyces cerevisiae* cells and green fluorescent 1.0 μm particles, which have similar volume as *Escherichia coli* cells. *Saccharomyces cerevisiae* were stained with red nucleic acid stain SYTO17. Both particles and cells again have concentrations of ~10^7 counts/ml. Due to weak red fluorescence from SYTO17 in our setup, we chose to use a combination of bright-field and fluorescent modes microscopy to record the sorting process. Figure 18(d) shows merged composite micrograph of green fluorescent 1.0 μm particles and bright-field particles/*Saccharomyces cerevisiae* mixture, both of which exited channel through Outlet D when magnetic fields were off. Sorting of this mixture was achieved as soon as magnetic fields were on, as depicted in Figures 18(e) and 18(f). Cells distribution analysis presented in the following section confirmed a close to 100% sorting efficiency. Sorting throughput was ~10^6 cells per hour. Here we demonstrated that combination of bright-field and fluorescent microscopy can successfully circumvent recording issues originating from opaqueness of ferrofluids and weak fluorescence from stained live cells.

Finally, sorting of *Escherichia coli* and *Saccharomyces cerevisiae* cells were carried out in the same device at the same time. *Escherichia coli* cells were stained with green fluorescence while *Saccharomyces cerevisiae* were stained with red fluorescence. Both types of cells were adjusted to ~10^7 cells/ml concentration in initial mixture. It is clearly shown in Figure 18(g) that all cells exited from the channel through Outlet D when there was no magnetic field. Both bright-field and fluorescent mode micrographs of cells were recorded and merged to form Figure 18(g). *Saccharomyces cerevisiae* cells were successfully sorted from the initial cell mixture with the application of magnetic fields, as demonstrated in Figures 18(h) and 18(i).

5.4.3 Cell Sorting Efficiency

In order to precisely evaluate sorting efficiency, we collected samples from both Outlets C and D and analyzed them for size distributions off chip. We stained cells in distinctive fluorescence and counted them using ImageJ® software. Specifically, in first calibration, *Escherichia coli* cells were green and 7.3 μm particles were red; in second calibration, *Saccharomyces cerevisiae* cells were red and 1.0 μm particles were green; in cells sorting, *Saccharomyces cerevisiae* cells were red and *Escherichia coli* cells were green. Fluorescent mode was chosen for distribution analysis to avoid miscounting of cell types in bright-field micrographs. A magnetic field was applied to push all particles and cells onto a surface of glass slide to increase visibility. We define remaining efficiency as ratio of number of particles or cells exiting from Outlet D after magnetic field application to their initial number before magnetic field application. Similarly, sorting efficiency is defined as the ratio of number of particles or cells exiting from Outlet C after magnetic field application to their initial number before magnetic field application. Figure 19(a) shows a representative composite micrograph of *Escherichia coli* cells and 7.3 μm particles collected from Inlet A before sorting. 100% of 7.3 μm particles migrated to Outlet C and 98.8% *Escherichia coli* cells remained in Outlet D, as depicted in Figures 19(b) and 19(c). Remaining and separation efficiencies for both particles are plotted in Figure 19(d). Figures 19(e) – 19(h) and Figures 19(i) – 19(l) show micrographs and efficiencies for *Saccharomyces cerevisiae* cells/1.0 μm particles mixture sorting and *Saccharomyces cerevisiae* cells/*Escherichia coli* cells mixture sorting, respectively. Both cases have 100% efficiencies. It should be noted that samples collected from Outlets C and D were greatly diluted by ferrofluid sheath flow from Inlet B, rendering much lower

particles and cells concentration for distribution analysis. A possible solution to this problem is integration of cell focusing [112] and sorting steps on one chip. The resolution of ferrohydrodynamic sorting depends on the difference in the cells' deflections towards the outlets. There is more deflection if cells stay longer in the channel. Cells stream typically

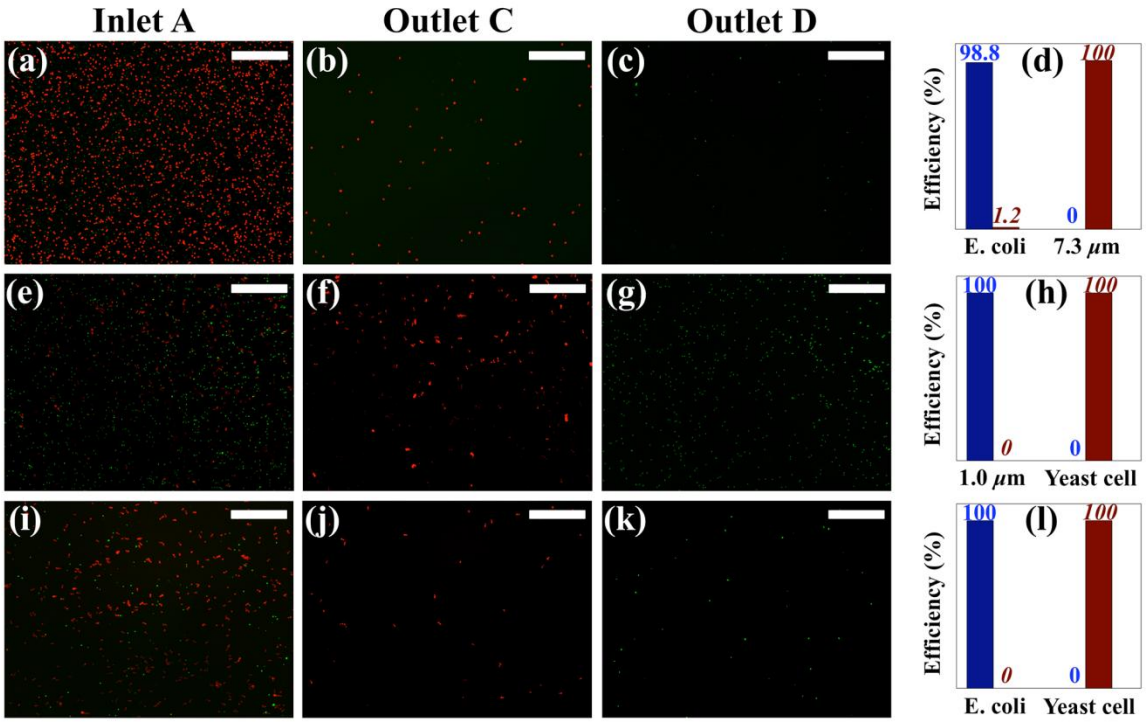

Figure 19. Experimental composite micrographs of size distribution analysis, including micrographs of particles/cells mixture collected before sorting at Inlet A and after separation at Outlets C and D, and remaining and separation efficiencies. (a) – (d) were for *Escherichia coli* and 7.3 μm particles mixture; (e) – (h) were for *Saccharomyces cerevisiae* and 1.0 μm particles mixture; (i) – (l) were for *Escherichia coli* and *Saccharomyces cerevisiae* mixture. Blue bar with normal number on top shows remaining efficiency, while red bar with italic number on top shows separation efficiency. Scale bars represent 200 μm.

has a finite width in the channel due to device design and their diffusions. In order to separate two types of cells, the difference in the cells' deflections needs to be larger than the width of cells stream at outlets. In the case of small size difference between two types of cells, a longer channel may help enhance sorting efficiency. Ferrohydrodynamic cell sorting throughput and effiencyi greatly depend on device parameters and fluid properties. Device parameters including dimensions of magnets and channel, flux density of magnets, relative positions of magnets with respect to channel, as well as fluid properties including ferrofluid concentration, viscosity, and susceptibility have significant effects on sorting performance. Optimizations of these parameters are needed in order to extend this approach into manipulations and sorting of different types of cells.

CHAPTER 6

CONTINUOUS SEPARATION OF HELA AND MOUSE RED BLOOD CELLS

6.1. Introduction

Cancer prevention and control in low resource settings is hampered by the high cost of introducing a comprehensive cancer control program involving vaccination, screening and treatment. Easy to use objective screening tests are urgently needed to improve the efficiency of cancer diagnostics. Exfoliated cervical cytology, the Pap test, has been the basis of effective cervical cancer screening [115]. However, substantial interobserver variability exists in interpreting cervical cytology [116]. Cytology screening also require an expensive infrastructure and highly trained cytotechnologists, limiting their implementation in low resource settings with the highest burden of disease [115]. High-risk human papillomavirus (HR-HPV) testing increases the sensitivity of screening, but specificity remains relatively low, especially in younger women with high HPV prevalence [117, 118]. Biomarkers based on molecular changes in response to HPV infection and neoplastic progression identified in biopsies are difficult to apply in exfoliated samples because of its heterogeneous nature; abnormal cells comprise a very small portion of the total and the contribution of local inflammatory cells can be hidden by bleeding during sample collection [119-122]. False-negative rates are greatest when abnormal cervical cells are a small proportion of total cells [123-125]. Unsatisfactory samples have a greater association with abnormal cytology, including cancer, than those with a negative index Pap test [126]. Frequent causes of unsatisfactory liquid-based cervical cytology (LBC)

slides include obscuration by erythrocytes, leukocytes, and mucin [127]. Such factors can also compete for space on LBC slides and result in reduced cervical epithelial slide cellularity. Misinterpreted cervical cytology ranks third among causes of medical negligence claims against pathologist [128]. The assay platforms that are not affected by dilution require a large amount of time and expertise to screen for the rare neoplastic cells. Cervical cancer screening would greatly benefit first from elimination of blood, mucin, and debris from cervical epithelial cells as shown in Figure 20 and secondly from enrichment of abnormal cells within the epithelial fraction.

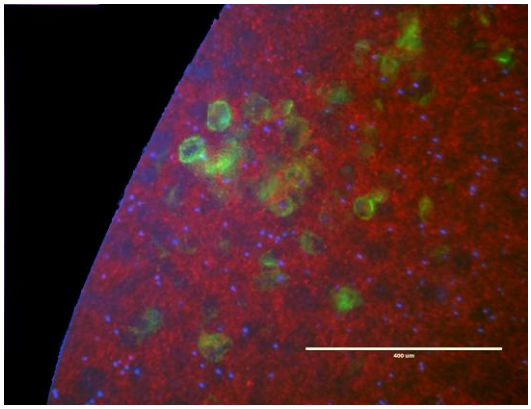

Figure 20. Mixture of cervical epithelial cells (green), red blood cells (red), and Peripheral blood mononuclear cells (blue). Scale bar: 400 µm

The properties of mammalian cells differ from *Escherichia coli* and *Saccharomyces cerevisiae*. For cell manipulation, materials, *p*H value, and surfactants of ferrofluids need to be rendered biocompatible, at the same time the overall colloidal system of ferrofluids must be maintained. Typically, nanoparticles within ferrofluids for cell applications are made of magnetite [72]. *p*H value of ferrofluids needs to be compatible with cell culture and maintained at 7.4. Salt concentration, tonicity, and surfactant must be carefully chosen close to physiological conditions to reduce cell death. Although these are stringent requirements, progress has been made towards synthesizing biocompatible ferrofluids. For example, Koser's group used citrate to stabilize cobalt-ferrite nanoparticles for live red blood cell and *Escherichia coli* cell sorting [48]. Yellen's group

used Bovine Serum Albumin (BSA) to stabilize magnetite nanoparticles for human umbilical vein endothelial cells manipulation [50]. Viability tests from both studies have shown that cells were able to retain their viability for up to several hours in ferrofluids. In chapter 5, a commercially available *p*H ~7 magnetite ferrofluid was able to sustain viability of both *Escherichia coli* and *Saccharomyces cerevisiae* cells for at least 2 hours. However，it doesn't facilitate the manipulation of mammalian cells as revealed in the experimental section. Here we demonstrate the optimization of the ferrohydrodynamic platform including chip design and ferrofluids development for mammalian cell separation using mouse red blood cells and HeLa cell (average diameter ~ 13 μm) as example [129]. Red blood cells are discoid, anucleate cells with diameter around 8 μm and thickness around 2.5 μm [130].

6.2. Simulation

In previous Chapters, we applied both two-dimensional (2D) and three-dimensional (3D) analytical models for simulating microfluidic transports of microparticles and biological cells in ferrofluids [69, 112]. In this work, we continue the simulation work to predict mammalian cells' sorting in an optimized permanent magnet based device as illustrated in Figure 24. All relevant parameters used in our simulation are listed in Figure 21 and Materials and Methods section. Briefly, we first calculate magnetic buoyancy force on particles in the rectangular microfluidic channel using a 3D analytical model of magnetic fields [77] and a nonlinear magnetization model of ferrofluids [39], and then solving governing equations of motion for particles in laminar flow condition [84]. We use nonmagnetic spherical polystyrene beads (diameters of 5.8 μm and 15.5 μm) as close approximation to represent mouse red blood cells and HeLa cells. The initial y-

axis position is located at the upper side of the inlet A. We also simulate particle trajectories corresponding to diameters of 1 μm, 10 μm and 20 μm for comparison.

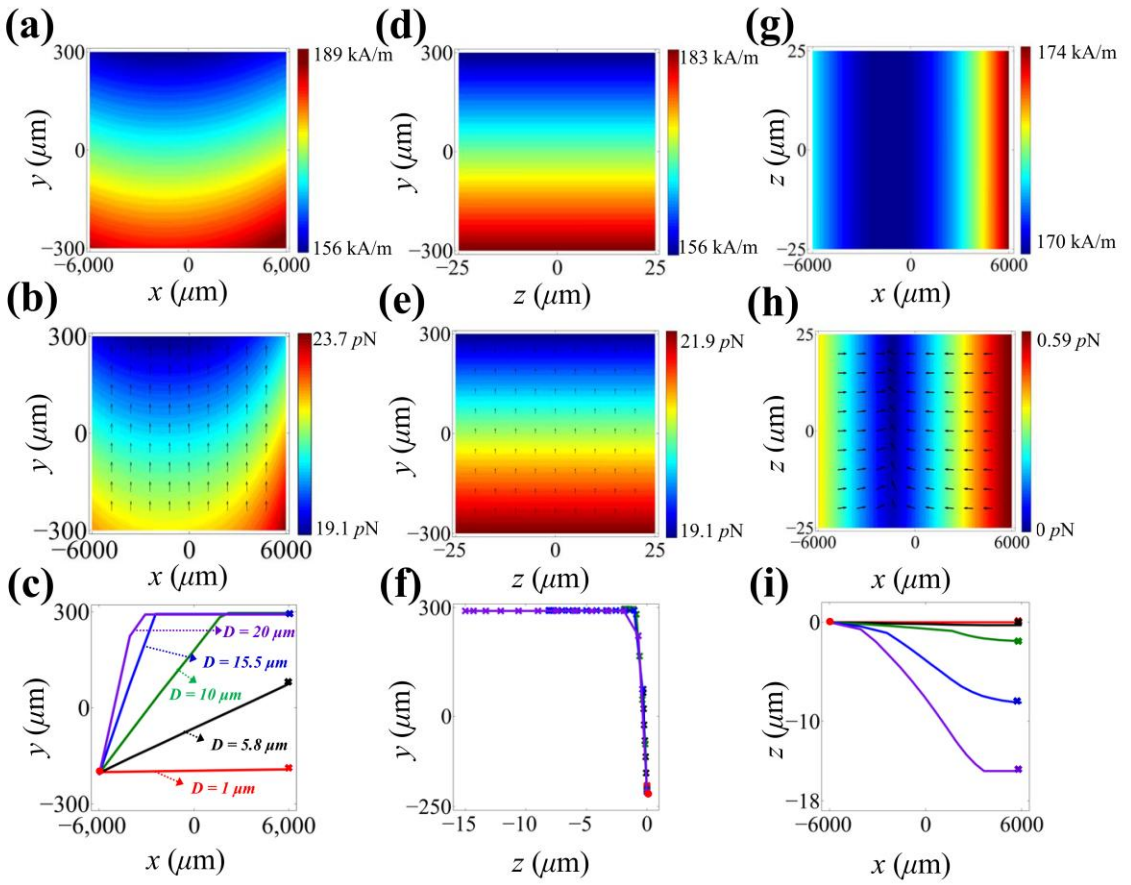

Figure 21. Analytical three-dimensional simulation of magnetic field and force distributions in microfluidic channel, and trajectories of cells. Simulation parameters match exact experimental conditions. (a)-(c) *x*-*y* plane (*z* = 0), (d)-(f) *y*-*z* plane (*x* = 0), (g)-(i) *x*-*z* plane (*y* = 0) of magnetic field strength (surface plot) (a, d, g), magnetic force (surface plot: force magnitude; arrow plot: force direction) (b, e, h), and particles' trajectories (c, f, i). Dots indicate starting points, while crosses indicate trajectories or ending points of cells motion. Mouse red blood cell has diameter ~ 6 μm and HeLa cell has a diameter ~ 15 μm^3, resulting in a spatial separation of these two types of cell in this configuration.

Figure 21 summarizes simulated distribution of magnetic fields and magnetic buoyance forces in the sorting channel, as well as 3D trajectories of mouse red blood cells and HeLa cells. The surface plot in Figure 21(a) shows magnitude of magnetic fields of *x*-*y* plane at $z = 0$. Magnetic fields decayed from the surface of the magnet and formed a gradient that resulted in magnetic buoyance force on cells in both *x* and *y* directions, as indicated in Figure 21(b). Consequently, cells experiencing such force when entering the sorting channel would decelerate in *x* direction and accelerate in *y* direction. Force computed on a spherical microparticle of 5.8 μm diameter, with its total volume (~102 μm^3) close to that of a single mouse red blood cell, is on the order of 20 *p*N. Buoyant force on the same particle is about 1000 times smaller than magnetic buoyance force. Cell mixtures were quickly sorted by magnetic buoyancy force towards the end of channel, as shown in Figure 21(c) with simulated trajectories. Figures 21(d)-(f) illustrate distribution of magnetic fields and forces, as well as trajectories of cells of *y*-z plane at $x = 0$; Figures 21(g)-(i) depict the cases of *x*-z plane at $y = 0$. Particles and cells are visible in bright field when diluted ferrofluids (~1% v/v) and thin microchannel were used in our device.

6.3. Materials and Methods

6.3.1. Ferrofluids synthesis

Nanoparticles were synthesized by chemical co-precipitation [131]. In a typical reaction, magnetite nanoparticles were precipitated out of 36mL aqueous Ammonia solution(28% (w/w)) by adding a mixture of 50 mL 0.4 M iron (II) chloride tetrahydrate and 0.8M iron (III) chloride hexahydrate. The magnetic nanoparticles suspension was centrifuged at 1000 RCF for 2 minutes, the supernatant was removed and the pellet re-

suspended in a solution of 2 M nitric acid and 0.35 M iron (III) nitrate. The mixture was then stirred at 90 ^{0}C for about 25 minutes. The color of the suspension changed from black to reddish brown. The suspension was then centrifuged at 1000 RCF for 2 minutes, the pellet was dispersed in water, yield a stable dispersion. The pH of the dispersion was between 1.5 and 1.8, which was then raised to 3.5 by adding 1 M NaOH solution. 20 mL acrylic copolymer solution ATLOX 4913 was then added and stirred for 5 minutes before raising the pH to 6.8. The mixture was vigorously stirred for 1 h at room temperature, and the resulting ferrofluid was dialyzed against water for one week. Water was refreshed on a daily basis. After dialysis, excess water was vaporized in a 90 ^{0}C oven to reach a final volume around 50 mL. 10X HBSS was added into the ferrofluid with a volume ratio of 1:9 to render the liquid isotonic to mammalian cells.

Fe(II) chloride tetrahydrate (99%), Fe(III) chloride hexahydrate (98%), Fe(III) nitrate nonahydrate (99%), nitric acid(70%), ammonium hydroxide (28% NH_3 in water, w/w) and ten time concentrated Hank's balanced salt solution (10X HBSS) were purchased from Sigma-Aldrich and used as supplied. DI water was used throughout the work. The polymeric surfactant ATLOX 4913 was kindly donated by Croda Inc., NJ and used without further purification.

6.3.2. Ferrofluids characterization

a. Size determination by TEM

TEM images were taken using a Tecnai 20 electron microscope from Philips (200 keV). A copper/rhodium grid (from Electron Microscopy Sciences) was covered with a thin carbon film and dipped into a ferrofluid sample diluted with water. After TEM images were captured, particle sizes in the images were characterized using ImageJ®

software. The distribution of magnetic nanoparticle core sizes was obtained from the TEM images (around 300 particles counted).

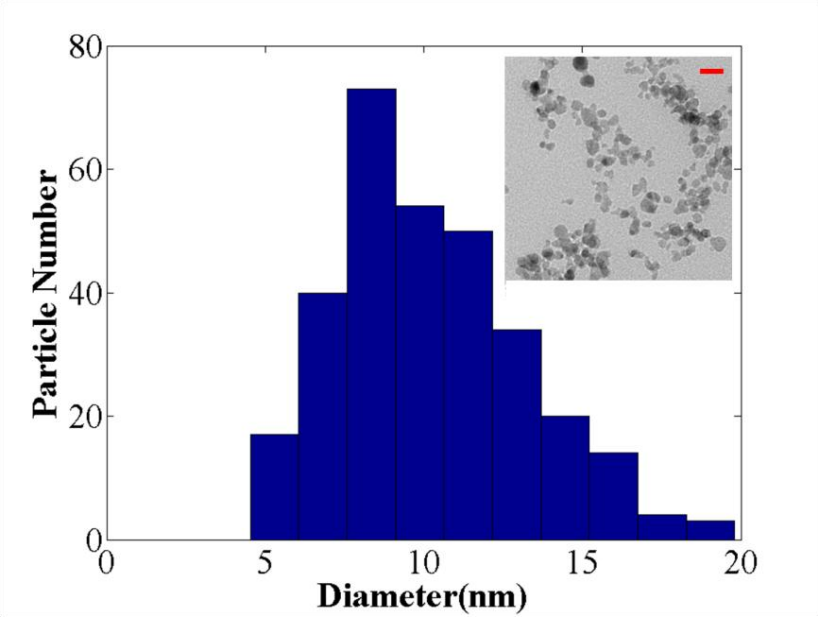

Figure 22. Distribution of maghemite nanoparticle sizes as obtained by TEM. Mean nanoparticle core diameter is: 10.25 ± 2.95 nm. (Scale bar: 20 nm).

b. Magnetic properties (VSM)

We measured the field dependent DC magnetization of the ferrofluid samples using a P525 vibrating sample magnetometer (VSM) on a Quantum Design Physical Property Measurement System (PPMS). The ferrofluid sample was injected into a plastic cylindrical capsule with the aid of a syringe, sealed by a small amount of super glue, and then sealing tested in vacuum. The sample mass was determined by differentiating the mass before and after filling the capsule. The sample mass was chosen to be between 10-15 mg to ensure both the intensity of signal and a small vertical sample size. The total masses of the ferrofluid samples and super glue were also checked before and after the sealing test. The magnetic signals of the empty capsule and super glue were confirmed to

be negligible. Typically, 2-3 samples of the same nominal composition were prepared and measured to check the reproducibility. The measurements were conducted at 300 K and at a vibrating frequency of 40 Hz; the applied field sweeps between +/- 3000 Oe at 20 Oe/sec and between +/- 40000 Oe at 40 Oe/sec., respectively. Results are plotted in Figure 23.

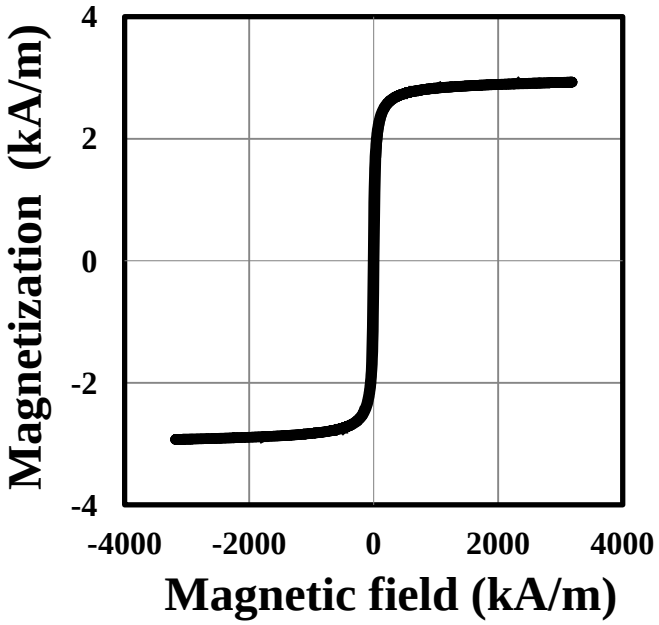

Figure 23. Direct current (DC) magnetization curve (quasistatic) of the ferrofluid. Volume fraction of a stock ferrofluid was calculated to be 0.71%. PEG ferrofluids with volume fraction 0.92% was used for the separation experiments.

6.3.3. Cell handling

HeLa cells were cultured in culture flasks (BD Falcon) containing 12 mL of DMEM medium with 10% (v/v) fetal bovine serum, 100 U/mL penicillin, and 100 μg/mL streptomycin. Cells were incubated (5% CO2, 90% humidified) at 37 °C in an incubator (Innova-Co 170; New Brunswick Scientific, U.K.) prior to use. Cells were sub-cultured at

a ratio of 1:5 every 3 days to maintain cells in the exponential growth phase. Cells were detached from the flask with the treatment of 0.25% (w/v) trypsin–EDTA solution (GIBCO) for 3 min before harvest. Cells were then suspended in the HBSS at a concentration ~2×10^6 cells/mL before use.

The mouse blood was retro-orbitally collected into a tube (BD microtainer™) coated with K2EDTA and stored at 4 degree for future use. Cells were then suspended in the HBSS at a concentration ~ 2×10^6 cells/mL before use.

6.3.4. Cell Viability

Viability of HeLa, red blood cells are exposed to HBSS or ferrofluids. Nominally 2×10^6 cells were centrifuged twice at 4°C and washed in Hank's buffer solution (HBSS). For either cell type in duplicate, the washed cell pellet from centrifugation was combined with either 1 ml of ferrofluids or 1 ml HBSS as a control. After 2 hours of incubation at room temperature in these fluids, cell viability was determined with Trypan blue exclusion assay and counted with a haemocytometer.

6.3.5. Microfluidic device design and fabrication

The prototype polydimethylsiloxane (PDMS) microfluidic device as in Figure 24 was fabricated through the standard soft-lithography method. A NdFeB permanent magnet was embedded into PDMS channel with their magnetization direction vertical to the channel during curing stage. The magnet is 2.54 mm in width, 0.635 mm in both length and thickness. The magnet was placed 1 mm away from the channel. Flux density at the center of magnet stack's surface was measured to be 470 mT by a Gauss meter (Model 5080, Sypris, Orlando, FL) and an axial probe with 0.381 mm diameter of circular active area. Before liquid injection, the device was treated with plasma for 10

minutes to render PDMS surfaces hydrophilic. This step ensured both cells and microparticles would not attach onto PDMS surfaces during sorting.

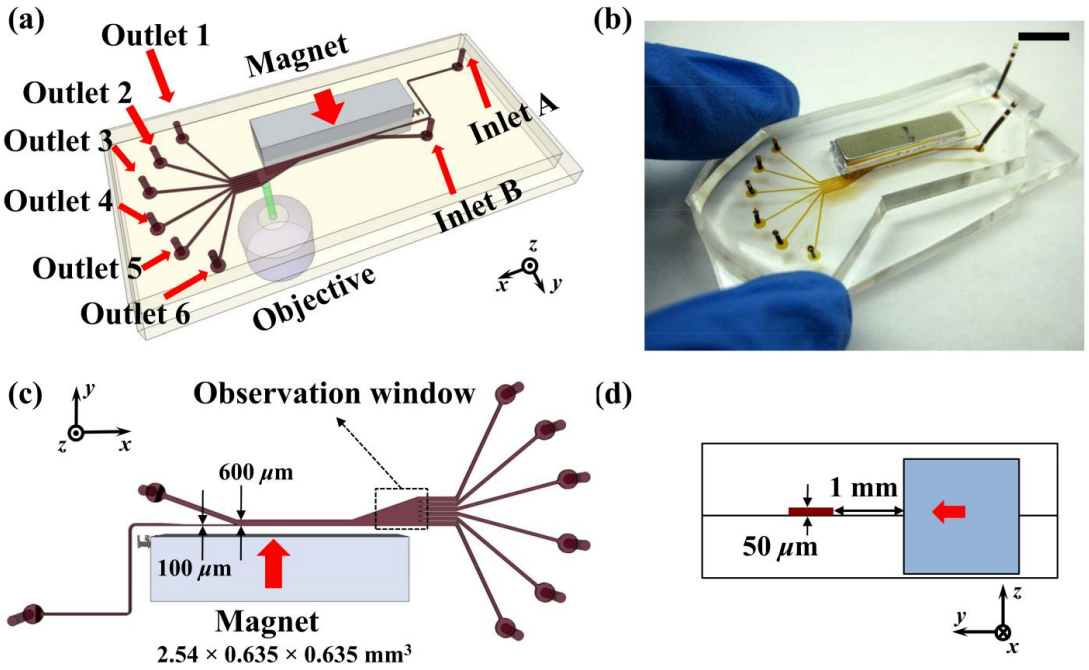

Figure 24. (a) Schematic representation of the sorting device with permanent magnets and a microfluidic channel. (b) An image of prototype device. Scale bar is 10 mm. (c) Topview of the device and relevant dimensions. Red arrows indicate direction of magnets' magnetization. (d) Cross-section of the device.

6.3.6. Microfluidic experiments setup

A water-based, pH ~ 7 maghemite ferrofluid was developed for mammalian cell sorting. Magnetic nanoparticles were stabilized with a neutral polyethylene glycol copolymer surfactant then suspended in 1X HBSS. Volume fraction of magnetic nanoparticles in this ferrofluid is 0.91%. HeLa cells, mouse red blood cells, and polystyrene microparticles (Bangs Laboratories Inc., Fishers, IN) with diameter of 5.8 μm were used in sorting. Ferrofluid and particles/cells mixture injected into microchannel

were maintained at tunable flow rates using a syringe pump (Nexus 3000, Chemyx Inc., Stafford, TX). Sorting was conducted on the stage of an inverted microscope (Zeiss Axio Observer, Carl Zeiss Inc., Germany). Micrographs of cells and particles were recorded with a high-resolution CCD camera (AxioCam HR, Carl Zeiss Inc., Germany). Cell samples collected from channel outlets were pipetted onto a haemocytometer and analyzed for size distributions to quantitatively evaluate efficiency of this approach. ImageJ® software was used to count the number of cells. After separation, cells from each outlet were also observed after a standard Cytospin and staining procedure, ~100,000 cells were cytocentrifuged at 2,000 rpm for 2 minutes on a glass slides. Cytospins were dried up and then stained with eosin Y and methylene blue.

6.4. Results and Discussion

6.4.1. Ferrfluids synthesis

Iron oxides such as magnetite (Fe_3O_4) or maghemite (γ-Fe_2O_3) were used for live cell experiments. They have been approved for use in MRI contrast agents by FDA [132, 133]. Iron oxide based ferrofluids with neutral pH and isotonicity have been rendered biocompatible for cell manipulation in the past [48, 50, 103, 134, 135]. Co-precipitation is the simplest and most widely used synthetic method for magnetite particles. Briefly, magnetite can be prepared by mixing ferrous and ferric salts in aqueous media under basic conditions in the absence of oxygen. This oxidation state is not stable and can quickly be oxidized to maghemite in air or under acidic conditions in the absence of oxygen. This approach produces a large amount of material quickly with polydispersed particles (2-20 nm) [136]. For our applications, we need to obtain magnetic nanoparticles with tunable sizes, in order to minimize the magnetic dipole-dipole interactions and

resulting particles chaining or clustering under external magnetic fields. Thermal decomposition method developed by Sun *et al.* [137] afforded nanoparticles with high monodispersity. However, it is difficult to synthesize hydrophilic nanoparticles suspended in aqueous suspension through this method. In this study, we adopted the co-precipitation method to synthesize iron oxide particles for subsequent tasks.

Colloidal stability is important for cell manipulation in ferrofluids. Ferrofluids provide a uniform magnetic environment for cells; any aggregation of particles will likely increase the non-uniformity and reduce the overall magnetic property of ferrofluids. There are two mechanisms through which magnetic nanoparticles aggregate. Firstly, when particles are getting too close to each other, van der Waals force will attract them and form agglomerations. This is typically solved by attaching surfactants to the surfaces of particles. Secondly, particles have dipole-dipole interactions in external magnetic fields. This interaction, if larger than the thermal agitation energy at room temperature, will also lead to particles aggregation. Typically, larger particles have larger magnetic moments and therefore are more prone to magnetic aggregation. In our initial effort, we have used PEG (MW300) and Dextran (MW10000) as surfactants to stabilize iron oxide particles from aggregation. Macroscopically, ferrofluids didn't exhibit particles settling under the influence of a permanent magnet. However, magnetic aggregates were formed, disrupting the uniformity of the liquid. Therefore, we need to engineer the ferrofluid to maintain its stability against van der Waals force and magnetic attraction. Under typical magnetic fields from a permanent magnet in our experimental setting, the largest size of iron oxide particles needs to be less than 10 nm for the resulting fluid to be stable against magnetic attraction.

Therefore, we developed a novel biocompatible ferrofluid stabilized by a PEG graft copolymer. Mean nanoparticle core diameter is measured to be 10.25 nm by TEM, standard deviation is 2.95 nm as shown in Figure 19. The magnetization curve for the ferrofluid is characterized using a VSM, as shown in Figure 22. The saturation magnetization of the ferrofluid is 2980 A/m, corresponding to a 0.71% magnetic material content within the ferrofluid, given the saturation magnetization of bulk magnetite is 4.2×10^5 A/m. We use the ferrofluid with volume fraction of 0.91% for the cell sorting experiments.

6.4.2. Cell viability

Figure 25 shows the HeLa cell viability in both PEG ferrofluids and EMG 408 ferrofluids after incubation. We observed a significant decrease in cell viability after 2 hours of incubation in the commercial EMG408 ferrofluid compared to the HBSS medium control, suggesting that the conditions of EMG 408 ferrofluid were not optimal for maintaining mammalian cell viability during incubation. Nonetheless, we observed the customized PEG ferrofluids were not detrimental to the viability HeLa cells after 2 hours of exposure, which allowed enough time to carry out the sorting procedure. Figure 26 shows the viability results for both HeLa and Blood cells in HBSS medium and PEG ferrofluids with three nanoparticles concentrations. For all the customized PEG ferrofluids, viabilities were maintained at the same level after 2 hours of incubation compared to the HBSS medium control for both cell types, which allowed enough time to carry out the sorting procedure. It also suggests the possibility of using more concentrated PEG ferrofluids to increase the magnetic buoyancy force in the same magnetic field condition.

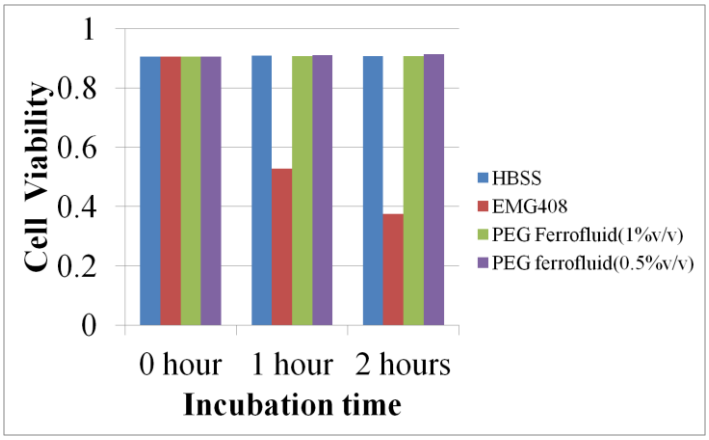

Figure 25. Cell viability test of HeLa cell in different ferrofluids. Medium 1: Hank's Balanced Salt Solution (1X HBSS), 2: EMG408 ferrofluid, 3: PEG ferrofluids (0.5% v/v) 4: PEG ferrofluids(1% v/v). After 0, 1, and 2 hours incubation, HeLa cell viability was counted with Trypan blue staining.

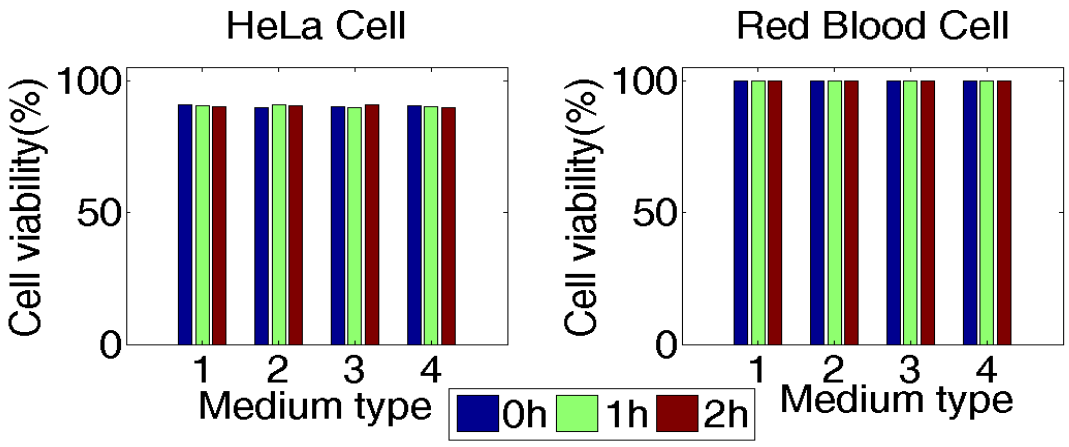

Figure 26. Cell viability test of HeLa cell and red blood cell in the PEG ferrofluid of different concentrations, medium 1: Hank's Balanced Salt Solution (1X HBSS), medium 2-3: PEG ferrofluids with nanoparticle volume fraction of 0.36%, 0.71%, 0.92% respectively. After 0, 1, and 2 hours incubation, HeLa cell and red blood cell viability counted with Trypan blue staining.

6.4.3. Cell sorting

We first calibrated the sorting device using a mixture of 15.5 μm and 5.8 μm beads as a model system before separating biological cells. For the microfluidic channel configuration as shown in device schematic Figure 24, particles in inlet A were first pushed towards the upper channel wall then hydrodynamically focused by a sheath flow from inlet B. Once entering the separation channel, particles of different sizes can be separated. Expansion channel with multiple outlets allow the collection of components to analyze the separation efficiency.

Microparticles and/or cells mixture were introduced into the microfluidic channel Inlet A at a constant flow rate of 8 μL/min, the flow rate from inlet B was 14 μL/min. When the magnetic fields were off, particles and cells were flowing near side wall of channel and exiting through Outlet 1 and 2, as shown in micrograph of Figure 27(a)-(d). When magnetic fields were on, particles in inlet A were first pushed towards the upper channel wall as shown in Figure 27(e). Once entering the rectangular area with coflow, particles were focused into a narrow stream. Magnetic buoyancy forces eventually deflected larger particles/cells from their laminar flow paths towards Outlet 5 and 6 as shown in Figure 27(g) and Figure 27(j). Meanwhile, forces on smaller particles/cells were insufficient to deflect them to Outlets 5 and 6; therefore they exited the channel through Outlet 1 to 4. This resulted in spatial separation of particles mixture at the end of channel. With the same configuration, we were also able to separate HeLa cells from either 5.8 μm beads or mouse red blood cells as manifested in Figure 28 and Figure 29. Visibility was enhanced by using phase contrast microscopy, HeLa cell and mouse red blood can be either brighter in Figure 28 or darker in Figure 29 compared with the ferrofluids flow

background. Small variations between experiments with same settings were not significant on the separation effect based on the size differences. HeLa cells were consistently separated into Outlet 5 and 6 as shown in Figure 28(j) and Figure 29(j). Compared with 5.8 μm beads, mouse red blood cells flow had a wider stream when the magnetic field is present, which suggested the effect of size variation. However, all the mouse red blood cells were constrained in Outlet 1- 4, yielding high separation efficiency against larger HeLa cells. We expect this procedure can also be applied for isolating circulating tumor cells(CTCs) from blood cells simply based on the size [119, 138].

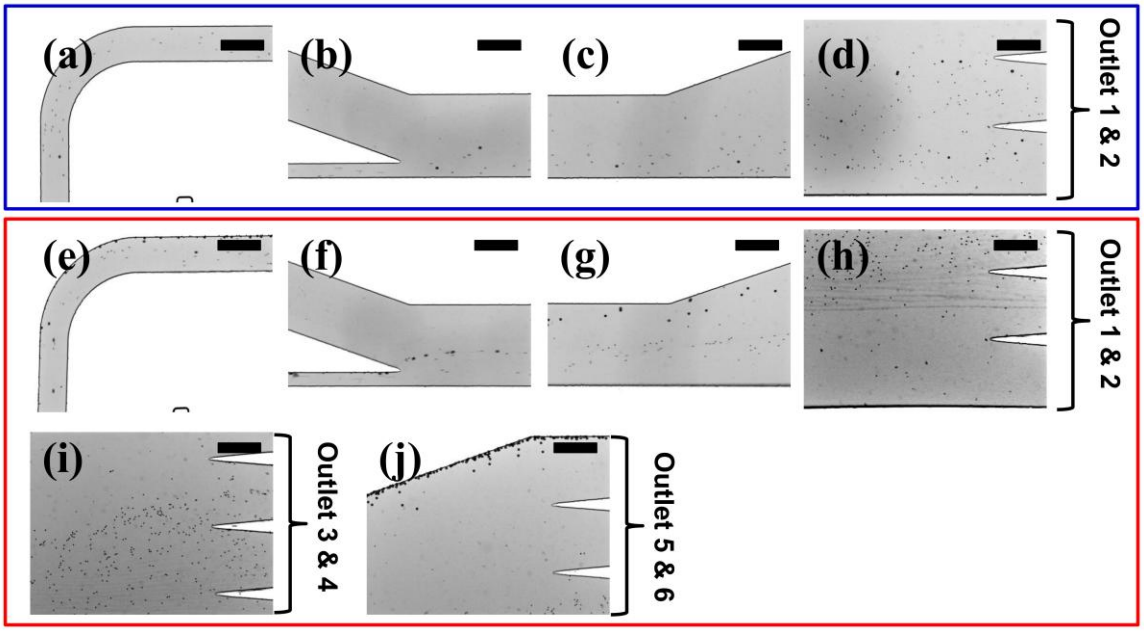

Figure 27. Micrographs of focusing and sorting process: (a)-(d) were micrographs of 15.5 μm and 5.8 μm particles in channel before magnetic field were applied ; (e)-(h) were micrographs after magnetic fields were applied. (h),(i),(j) illustrate micrographs of outlet 1-6. Scale bars represent 200 μm.

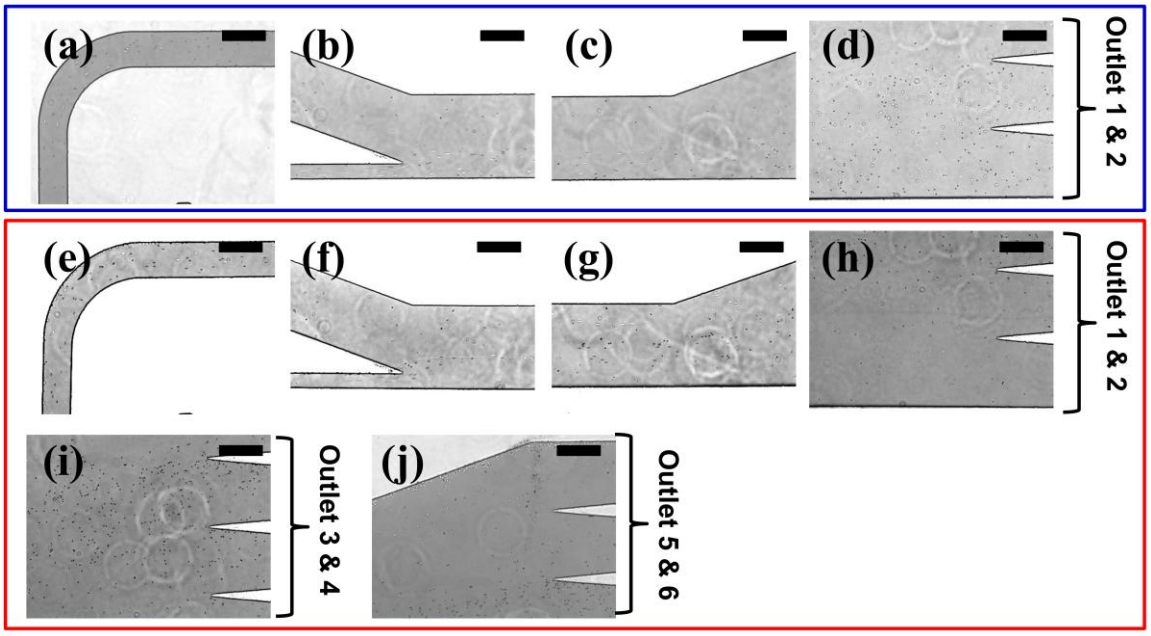

Figure 28. Micrographs of focusing and sorting process: (a)-(d) were micrographs of HeLa cells(white dots) and 5.8 μm particles (black dots) in channel before magnetic field were applied; (e)-(h) were micrographs after magnetic fields were applied. (h)-(j) illustrate micrographs of outlet 1-6. Scale bars represent 200 μm.

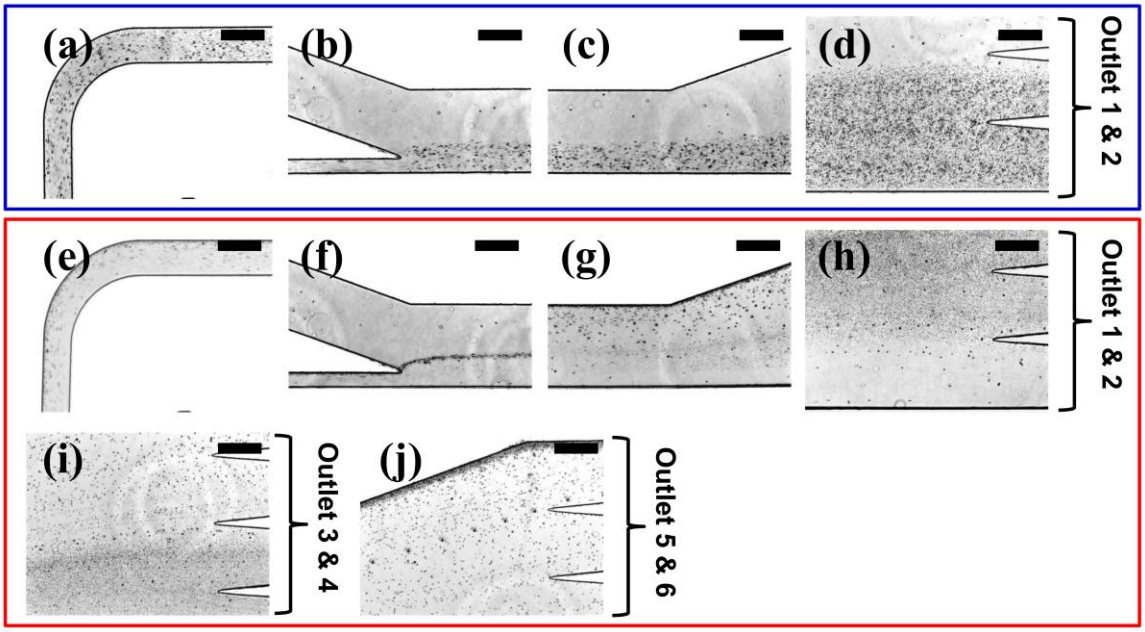

Figure 29. Micrographs of focusing and sorting process: (a)-(d) were superimposed micrographs of HeLa cells and mouse red blood cells in channel before magnetic field were applied; (e)-(h) were micrographs after magnetic fields were applied. (h)-(j) illustrate micrographs of outlet 1-6. Scale bars represent 200 μm.

2. Sorted cells analysis

After separation, microparticle and cell numbers at each outlet were counted with haemocytometer and analyzed for cells distribution. All the 15.5 μm particles were collected in outlet 6, while 5.8 μm particles were collected from outlet 3 to 5 as shown in Figure 30(a). Sample images from outlet 3 and outlet 6 were taken for better visualization with the help of cytospin and staining procedure. HeLa cell nucleus turns purple, cytoplasm is stained blue, and mouse red blood cell appears red as shown in Figure 31(a). 97.1% HeLa cells were collected in Outlet 6, the remaining smaller HeLa cells were collected in Outlet 5 as calculated by size distribution in Figure 30(c). From Figure 31(b),

debris of nucleus and cytoplasm exit along with large amount of mouse red blood cells into Outlet 3, larger intact HeLa cells were enriched into Outlet 6. The off chip analysis confirmed the optimized separation scheme are of high throughput and efficiency.

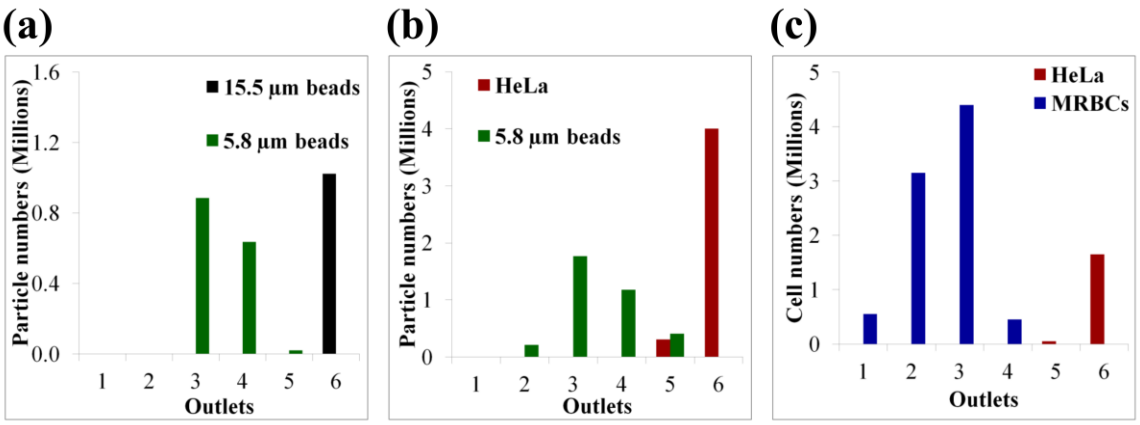

Figure 30. Separation efficiency verification by counting particle and cell numbers (/mL) from each outlet: (a) 5.8 μm particles and 15.5 μm particles; (b) 5.8 μm particles and HeLa cells; (c) Mouse red blood cells(MRBCs) and HeLa cells;

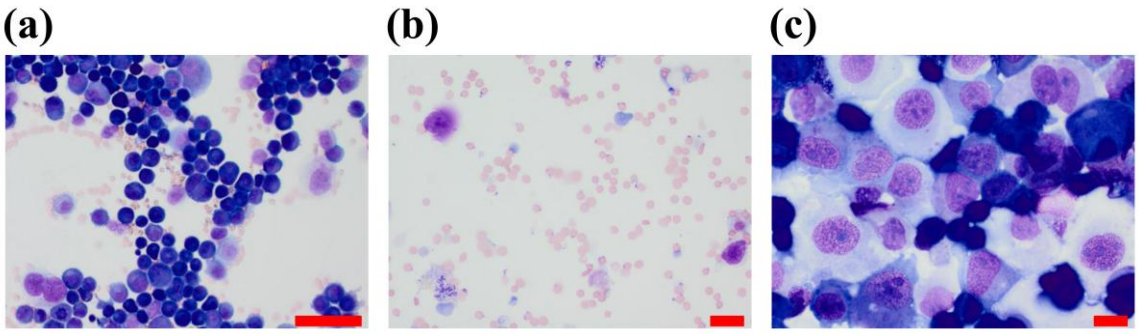

Figure 31. Images of MRBCs and HeLa cells prepared by Cytospin procedure: (a) MRBCs and HeLa cells mixture before separation (b) Cells collected from outlet 3; (c) Cells collected from outlet 6. Scale bars represent 20 μm.

CHAPTER 7

COMBINING POSITIVE AND NEGATIVE MAGNETOPHORESIS TO SEPARATE PARTICLES OF DIFFERENT MAGNETIC PROPERTIES

7.1. Introduction

In previous chapters, *Escherichia coli* and *Saccharomyces cerevisiae* (Baker's yeast) cells were separated from each other using a commercial ferrofluid with high throughput and efficiency in a continuous-flow fashion [67]. We were also able to demonstrate the mammalian cell sorting using a customized ferrofluid. In other studies, sorting of particles and cells in ferrofluids were developed using traveling-wave magnetic fields generated from microfabricated electrodes [48, 111] based on negative magnetophoresis. In most of these microfluidic applications, the study of manipulation specificity is predominately focused on the difference of size or volume between objects (e.g. cells or particles) in magnetic fluids. Few have paid attention to the difference of magnetic properties (e.g. initial susceptibility or magnetization) between objects and investigated them for the purpose of manipulation. To this end, we intend to combine positive and negative magnetophoresis with the goal of separating particles of different magnetic properties in a microfluidic system coupled with a permanent magnet.

Representative applications of positive magnetophoresis in microfluidics include manipulation and separation of paramagnetic beads or magnetically labeled cells under external fields. A typical example involves first labeling cells of interest with magnetic beads through either endocytosis or ligand-receptor interaction at their surfaces to render

the cell-beads conjugate magnetic. Because the magnetization of beads is usually larger than its surrounding medium (e.g. water), cell-beads conjugates are magnetized under external fields and therefore move towards the location of field maximum. As a result, cells of interest can be separated from the rest of the sample and manipulated remotely. Macroscopic positive magnetophoresis had been demonstrated in the past [139], and now, microfluidic positive magnetophoresis using permanent magnets has been developed to separate beads with different magnetic susceptibilities [22, 55], and cells with different distributions of magnetic nanoparticles [24, 140]. At the same time, microfabricated electromagnets were coupled to microfluidic devices to manipulate magnetic beads and cells with great precision [141-145]. Positive magnetophoresis uses magnetic beads for labeling in order to achieve specific manipulation and separation. The process of incubating cells with magnetic beads can take up to several hours and multiple washing steps are needed [24, 140], rendering the whole assay time-consuming and manually intensive. Furthermore, manipulation specificity of positive magnetophoresis depends on magnetic moment of beads or loading of magnetic nanoparticles in cells. Magnetic moments of beads, even from the same batch, can vary dramatically due to their manufacturing procedure [146-149]. In addtion, loading of magnetic nanoparticles in cells is greatly affected by their endocytotic capacities or ligand-receptor interactions and can vary among the same type of cells [24, 140, 150]. Therefore, it is highly beneficial to eliminate the labeling step associated with positive magnetophoresis and its application in cells manipulation.

The principle of negative magnetophoresis is exactly the opposite of positive magnetophoresis. A typical application of negative magnetophoresis in size-based cells

separation does not need any magnetic tags for labeling. Cells of different sizes were simply injected into a continuous-flow ferrofluid-filled microfluidic channel. Balanced by a diameter-dependent hydrodynamic viscous drag force, large cells experience more magnetic buoyancy force than smaller ones in ferrofluids, leading to a spatial separation between the two species at the end of the channel [66, 67].

The remainder of this chapter is organized as follows. First we will demonstrate the working mechanism of separating particles with different magnetic properties in ferrofluids and its feasibility through particle's trajectory simulation. We will then discuss experimental procedures including ferrofluids characterization and microfluidic experiments. Results and Discussion section starts with a first demonstration on separating magnetic and non-magnetic particles in a custom-made ferrofluid, followed by a second demonstration on separating particles with different magnetic properties in a commercial ferrofluid.

7.2. Working Mechanism

A general expression of the magnetic force on a magnetized body in a magnetic fluid under a magnetic field is displayed as Equation (1).[39] Here $\mu_0 = 4\pi \times 10^{-7}$ H/m is permeability of free space, V is volume of the magnetized body, typically a superparamagnetic microparticle impregnated with magnetite nanoparticles, $\vec{M}_p$ is its magnetization, $\vec{M}_f$ is magnetization of the magnetic fluid surrounding the body, and $\vec{H}$ is the magnetic field strength at the center of the body.

$$\vec{F} = \mu_0 V\left[\left(\vec{M}_p - \vec{M}_f\right)\cdot\nabla\right]\vec{H} \qquad (1)$$

In a weak magnetic field on the order of 10^3 A/m, such as the one generated by microfabricated electrodes, magnetizations of both the body $\vec{M}_p$ and the magnetic fluid $\vec{M}_f$ depend approximately linearly on the applied field, resulting in $\vec{M}_p = \chi_p \vec{H}$ and $\vec{M}_f = \chi_f \vec{H}$, where χ_p and c_f are the dimensionless initial magnetic susceptibilities of the body and the magnetic fluid, respectively. Therefore, magnetic force under weak field approximation takes the form as Equation (2) that is often cited in the literature,[23, 29, 30] here $\vec{B}$ is magnetic flux density.

$$\vec{F} = \frac{V\left(\chi_p - \chi_f\right)}{\mu_0}\left(\vec{B}\cdot\nabla\right)\vec{B} \tag{2}$$

In a magnetic field generated by a hand-held permanent magnet with its strength on the order of 10^6 A/m, Equation (2) is no longer valid as the magnetization of a superparamagnetic particle depends nonlinearly on the applied field, so does the magnetization of a ferrofluid, both of which can be modeled accurately by the classical Langevin theory. Langevin theory considers magnetic nanoparticles in a superparamagnetic microparticle and a ferrofluid as a collection of monodispersed and non-interacting magnetic dipoles.[39] This approach leads to the Langevin function of magnetization[39] in Equations (3) and (4). Here $\alpha_p = \mu_0 \pi M_{p,b} H d_p^3 / 6k_B T$ and $\alpha_f = \mu_0 \pi M_{f,b} H d_f^3 / 6k_B T$. ϕ_p and ϕ_f are volume fractions of the magnetic materials, $M_{p,b}$ and $M_{f,b}$ are saturation moments of the bulk magnetic materials, and d_p and d_f are diameters of nanoparticles in a superparamagnetic microparticle and a ferrofluid, respectively. k_B is the Boltzmann constant, *T* is temperature. Equation (1) in conjunction with Langevin function of magnetization (Equations (3) and (4)) applies to more general

cases than Equation (2) alone. We will use Equations (1), (3) and (4) in subsequent simulations.

$$\frac{\vec{M}_p}{\phi_p \vec{M}_{p,b}} = L(\alpha_p) = \coth(\alpha_p) - \frac{1}{\alpha_p} \tag{3}$$

$$\frac{\vec{M}_f}{\phi_f \vec{M}_{f,b}} = L(\alpha_f) = \coth(\alpha_f) - \frac{1}{\alpha_f} \tag{4}$$

In the case of positive magnetophoresis, magnetization of the superparamagnetic particle $\vec{M}_p$ is always larger than its surrounding fluid medium $\vec{M}_f$. Under a non-uniform magnetic field, the direction of magnetic force $\vec{F}$ on the particle is pointing towards field maxima. On the other hand, for negative magnetophoresis, magnetization of the particle or cell $\vec{M}_p$ is always less than its surrounding magnetic fluids $\vec{M}_f$, the direction of magnetic force $\vec{F}$ on the particle or cell is therefore pointing towards field minima. Both cases have been investigated extensively for their microfluidic applications, as they were reviewed in the Introduction section of this paper. However, few have considered the case where both magnetophoresis and negative magnetophoresis co-exist in one microfluidic system. In one of such cases, there exist two types of superparamagnetic particles with magnetizations of $\vec{M}_{p1}$ and $\vec{M}_{p2}$ in a magnetic fluid with magnetization of $\vec{M}_f$. Firstly, $\vec{M}_{p1}$ and $\vec{M}_{p2}$ being both larger than $\vec{M}_f$ will lead to a typical case of positive magnetophoresis while $\vec{M}_{p1}$ and $\vec{M}_{p2}$ being both less than will lead to negative magnetophoresis. In both cases, resulting magnetic forces depend not only on particles' magnetizations but also on their volumes. However, if $\vec{M}_f$ is between $\vec{M}_{p1}$ and $\vec{M}_{p2}$, *i.e.*, when the condition of $\vec{M}_{p1} > \vec{M}_f > \vec{M}_{p2}$ is met, magnetic force will attract particles Type 1

towards field maxima while pushes particles Type 2 away towards field minima, as shown in Figure 29(a). It should be noted here that the volume of particles now only affects the magnitude, but not the direction of magnetic forces. This way, particles can be distinguished and sorted solely based on their magnetizations in a simple microfluidic channel with a permanent magnet, as illustrated in Figure 29(b). The dynamics of particles in the microchannel is determined primarily by the balance of the magnetic force and the hydrodynamic viscous drag force.[69] The magnetic force scales with the volume of a particle, while the hydrodynamic drag force scales with the diameter of a particle. Therefore, the velocity of a particle moving towards or away from a magnetic field gradient depends on the square of the diameter.

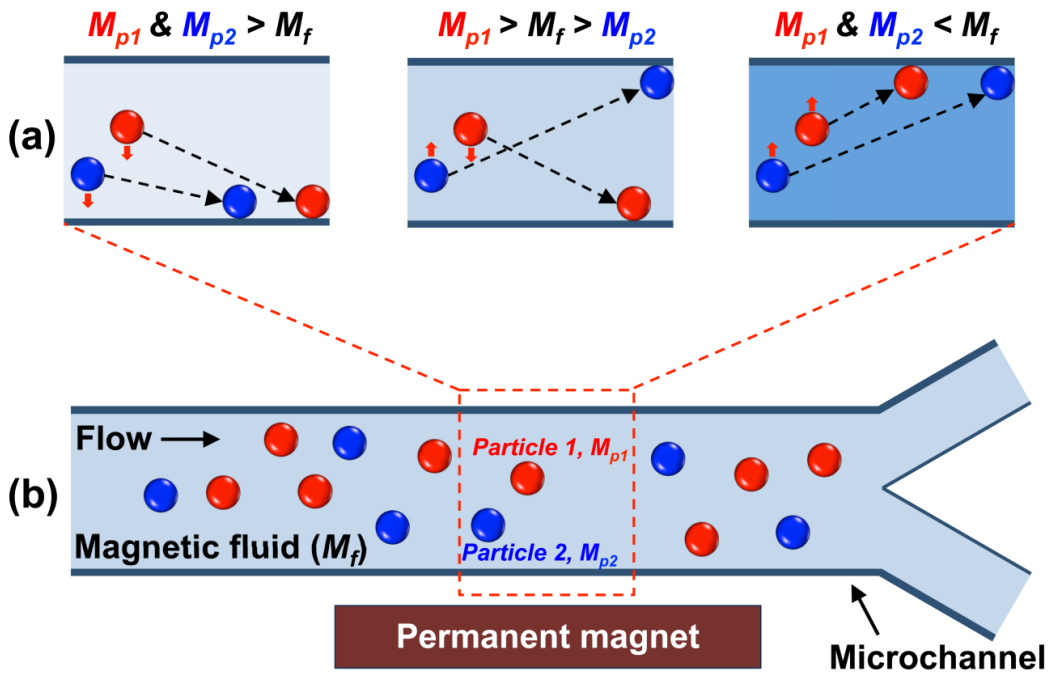

Figure 32. Schematic representation of combining positive and negative magnetophoresis in a ferrofluid to separate particles of different magnetic properties. (a) Particles with different magnetic properties experience either positive or negative

magnetophoresis and hence have different trajectories in a microfluidic device (b). Left illustration of (a) is the case where both types of particles experience positive magnetophoresis, right illustration of (a) is where both types of particles experience negative magnetophoresis. In middle illustration of (a), both positive and negative magnetophoresis exist.

7.3. Materials and Methods

Two types of ferrofluids are used in the microfluidic experiments. One of them is a water-based magnetite nanoparticle ferrofluid stabilized by sodium oleate surfactant. The nanoparticles are prepared through a chemical co-precipitation process,[151] which involves adding a mixture of iron(II)-chloride tetrahydrate and iron(III)-chloride hexahydrate into an ammoniumhydroxide solution. The gelatinous precipitate is washed, followed by the addition of sodium oleate solution and sonication. A second ferrofluid is a commercial water-based magnetite nanoparticle ferrofluid (EMG 408, Ferrotec Co., Bedford, NH) stabilized by proprietary anionic surfactants. Magnetization curves of both ferrofluids are measured using a Vibrating Sample Magnetometer (VSM). Two fluorescent polystyrene non-magnetic particles (green 4.2 μm diameter, Thermo Fisher Scientific Inc., Waltham, MA, and green 7.3 μm diameter, Bangs Laboratories Inc., Fishers, IN), and four fluorescent superparamagnetic particles (red 2.6 μm diameter, green 2.8 μm diameter, green 7.9 μm diameter, green 8.2 μm diameter, Bangs Laboratories Inc., Fishers, IN) are used in the experiments.

We measure the field-dependent direct current (DC) magnetizations of our ferrofluid samples using a vibrating sample magnetometer (VSM) on a Physical Property

Measurement System (PPMS) (Model P525, Quantum Design Inc., San Diego, CA). The ferrofluid sample is injected into a plastic cylindrical capsule using a syringe, sealed by a small amount of super glue, and then tested for sealing in vacuum. Sample mass is determined by differentiating the mass before and after filling the capsule. The mass is chosen to be between 10 and 15 mg to ensure both the intensity of magnetic signals and a small vertical sample size. Total mass of the ferrofluid sample and super glue are also checked before and after the sealing test. Magnetic signals of the empty capsule and super glue are confirmed to be negligible. Typically, two to three samples of the same nominal composition are prepared and measured to check the reproducibility of measurements. The measurements are conducted at 300 K and at a vibrating frequency of 40 Hz. The applied field sweeps between +/- 3,183 kA/m at a rate of 3,183 A/m per second.

The prototype polydimethylsiloxane (PDMS) microfluidic device is fabricated through a standard soft-lithography approach[152] and attached to a flat surface of another piece of PDMS, as shown in Figures 30(a) and (b). A mask of the device pattern is designed using AutoCAD 2008 (Autodesk Inc., San Rafael, CA) and printed by a commercial photo-plotting company (CAD/Art Services Inc, Bandon, OR). Dimensions of the microfluidic channel are listed in Figures 30(c) and (d). Thickness of the device is measured to be 38 μm by a profilometer (Dektak 150, Veeco Instruments Inc., Chadds Ford, PA). Before attachment, channel surface is treated with air plasma (PDC-32G plasma cleaner, Harrick Plasma, Ithaca, NY) at 11.2 Pa O_2 partial pressure with 18 W power for 1 minute. One neodymium-iron-boron (NdFeB) permanent magnets is embedded into the microchannel with its magnetization direction vertical to the channel

during PDMS curing stage. The magnet is 25.4 mm in length, 3.175 mm in width and 3.175 mm in thickness. The magnet is placed 2 mm away from the edge of the channel. Magnetic flux density at the center of magnet surface is measured to be 470 mT by a Gauss meter (Model 5080, Sypris, Orlando, FL) and an axial probe with 0.381 mm diameter of circular active area. Before experiments, the device is treated again with air plasma for 10 min and then washed with 1% Triton-X solution to render the microchannel surfaces hydrophilic and reduce particles' attachment.

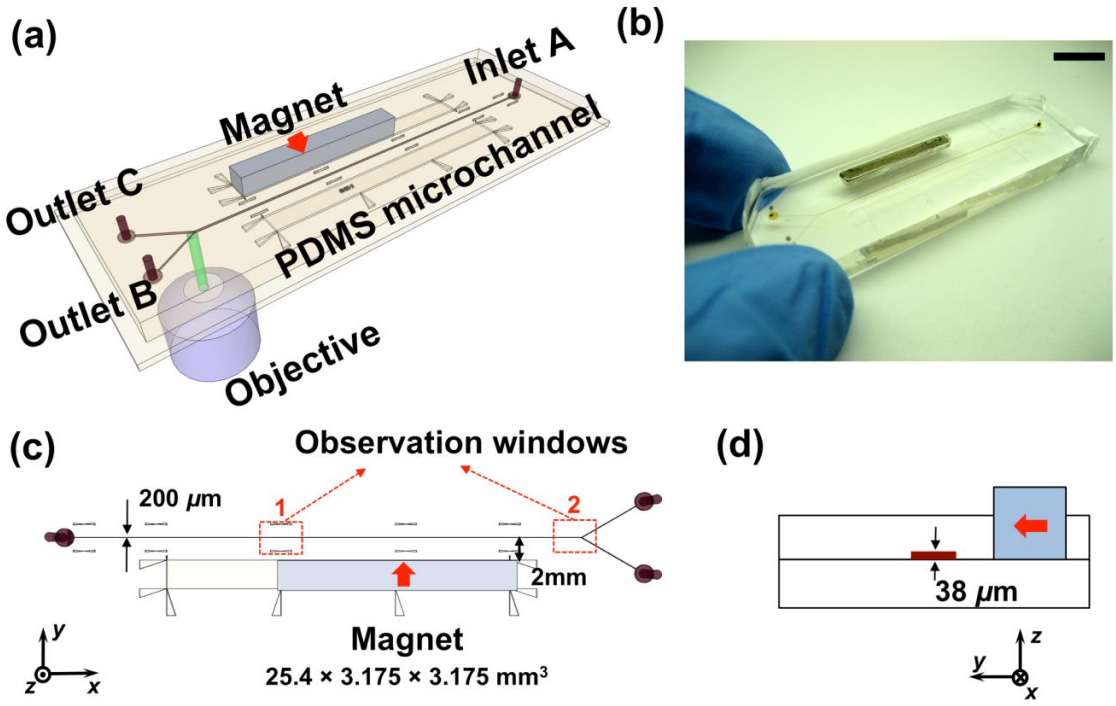

Figure 33. Device illustrations. (a) Schematic drawing of the microfludic device with a permanent magnet and a microchannel. (b) An image of prototype device. Scale bar is 10 mm. (c) Topview of the device and relevant dimensions. Red arrows indicate direction of magnets' magnetization. (d) Cross-section of the device.

Microfluidic experiments are conducted on the stage of an inverted microscope (Zeiss Axio Observer, Carl Zeiss Inc., Germany). A mixture of ferrofluids and particles are injected into a microchannel and maintained at a tunable flow rate using a syringe pump (Nexus 3000, Chemyx Inc., Stafford, TX). Micrographs of particles are recorded using bright-field mode and fluorescent mode through either a green fluorescent filter set (41001 FITC, Chroma Technology Corp., Rockingham, VT) or a red filter set (43HE, Carl Zeiss Inc., Germany), and a CCD camera (SPOT RT3, Diagnostic Instruments, Inc., Sterling Heights, MI).

In this chapter, we extend our two-dimensional analytical model of particles' transport in ferrofluids [69] to three dimensions in order to enable fast and accurate predictions for trajectories of microparticles with different magnetizations in a microfluidic system. We choose to use an analytical approach over numerical ones because of its advantages in simulation speed and accuracy.[69] We obtain three-dimensional particles' trajectories in microchannels by first calculating magnetic buoyancy force (Equation (1)) on particles using a three-dimensional analytical model of magnetic field distribution and a nonlinear magnetization model of ferrofluids (Equations (3) and (4)) inside the microchannel, then deriving and solving governing equations of motion for particles in laminar flow conditions using analytical expressions of magnetic buoyancy and hydrodynamic drag forces.

7.4. Results and Discussion

We start with simulation results in Figure 31 that depict distributions of magnetic fields and magnetic forces on a 4 μm diameter particle within the microchannel, as well as representative trajectories of that particle with different magnetizations in a ferrofluid

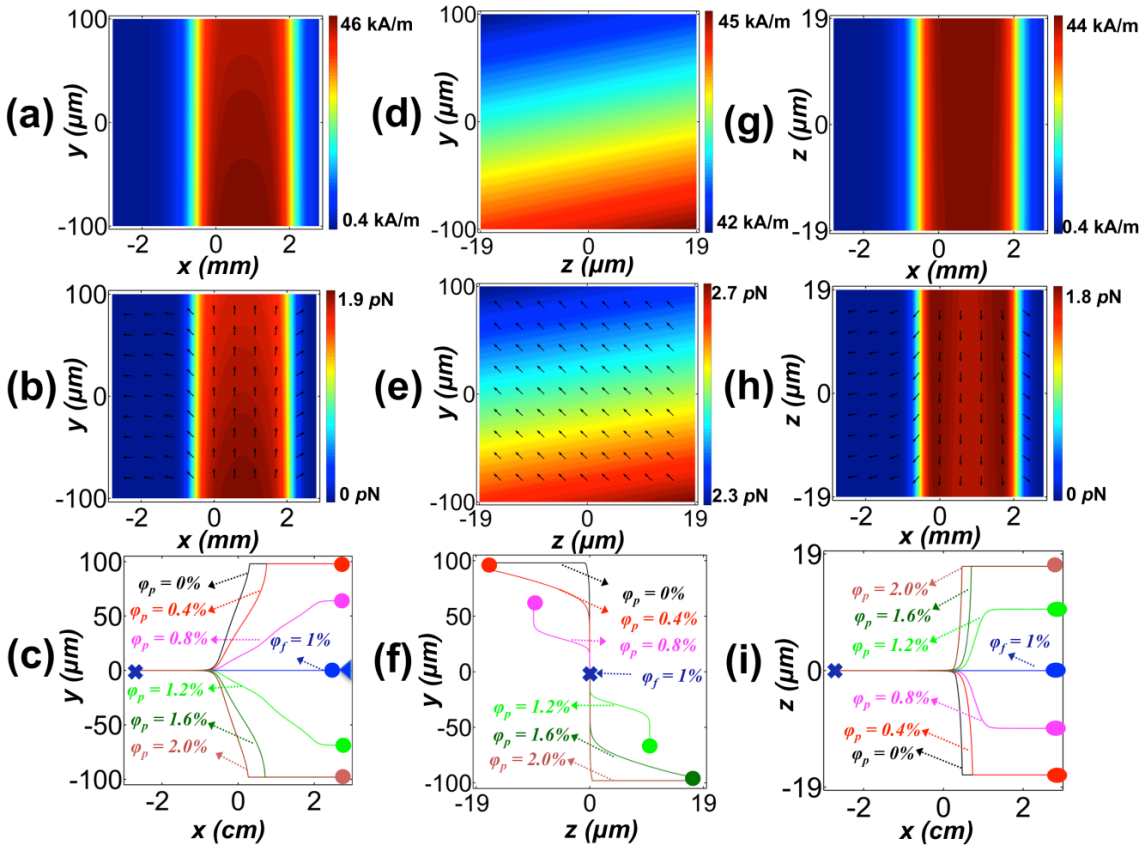

Figure 34. Analytical three-dimensional simulation of magnetic field and force distributions in microfluidic channel, and trajectories of 4 μm diameter particles with different magnetic volume fractions. (a)-(c) *x*-*y* plane (z = 0), (d)-(f) *y*-*z* plane (x = 0), (g)-(i) *x*-*z* plane (y = 0) of magnetic field strength (surface plot) (a, d, g), magnetic force (surface plot: force magnitude; arrow plot: force direction, both are calculated on a 4 μm diameter non-magnetic particle) (b, e, h), and particles' trajectories (c, f, i). Magnetic volume fraction of the ferrofluid is chosen to be 1%, while particles have 0%, 0.4%, 0.8%, 1%, 1.2%, 1.6% and 2% of magnetic volume fractions. Ferrofluid flow rate is 1.5 μL/min. Other simulation parameters match exact experimental conditions. Crosses indicate starting points, while solid circles indicate ending points of particles' trajectories. Blue triangle in (c) indicates boundary between outlets.

in all three dimensions. Figure 31(a) shows a surface plot of the magnitude of magnetic fields in the *x*-*y* plane at *z* = 0 within the channel. Magnetic fields decay quickly and form a gradient pointing towards the negative *y* direction. The gradient leads to a magnetic buoyancy force on the non-magnetic particle (ϕ_p = 0) pointing towards the positive *y* direction, as shown in Figure 31(b). Figure 31(c) shows the relationship between the particle's trajectory and its magnetic volume fractions. Here we fix the magnetic volume fraction of the ferrofluid at 1%, very close to the measured value of the EMG 408 commercial ferrofluid that will be used in later experiments. Based on the analysis before, a particle having a smaller magnetic volume fraction (<1%) than the surrounding fluid experiences negative magnetophoresis and is pushed away from the magnet; while a particle with a larger magnetic volume fraction (>1%) experiences positive magnetophoresis and is attracted towards the magnet. When the magnetic volume fractions of both the particle and the fluid match exactly ($\phi_p = \phi_f = 1\%$), the particle experiences so called "isomagnetophoresis"[153, 154] and retains its laminar flow path without deflection. Figures 31(d)-(f) illustrate distributions of magnetic field and force, as well as trajectories of the particle in the *y*-z plane at *x* = 0; Figures 31(g)-(i) illustrate the case for *x*-z plane at *y* = 0.

In order for positive and negative magnetophoresis to co-exist, the ferrofluid's magnetization $\vec{M}_f$ needs to be between the particles' magnetizations $\vec{M}_{p1}$ and $\vec{M}_{p2}$. Magnetic force will then attract one type of particles while repel the other and result in spatial separation of the two. It is therefore critical to determine the magnetization of ferrofluid and both particles at a specific magnetic field, most relevant to actual experimental conditions. Magnetization curves of superparamagnetic particles are

provided by the manufacturer and are shown in Figure 32(a). Saturation magnetization of both 2.6 μm and 2.8 μm particles (categorized as ~3 μm particles) is 10,019 A/m, while saturation magnetization of 7.9 μm and 8.2 μm particles (categorized as ~8 μm particles) is approximately 2,939 A/m. It should be noted that the magnetization is measured on a specific batch of sample containing many particles, then averaged per unit volume. It is an average property of a large number of particles, actual magnetization of individual particle may vary significantly within the same batch, and magnetization of one batch may vary from another. We only use the magnetization curve as a rough estimate for particles' magnetization in the following separation experiments. The magnetization curve for the ferrofluid stabilized by sodium oleate is characterized using a VSM, as shown in Figure 32(b). The saturation magnetization of the ferrofluid is 571 A/m, corresponding to a 0.1% magnetic material content within the ferrofluid, given the saturation magnetization of bulk magnetite is 4.46×10^5 A/m. The saturation magnetization of the EMG 408 commercial ferrofluid is measured to be 4,953 A/m, corresponding to a 1.1% magnetic material content.

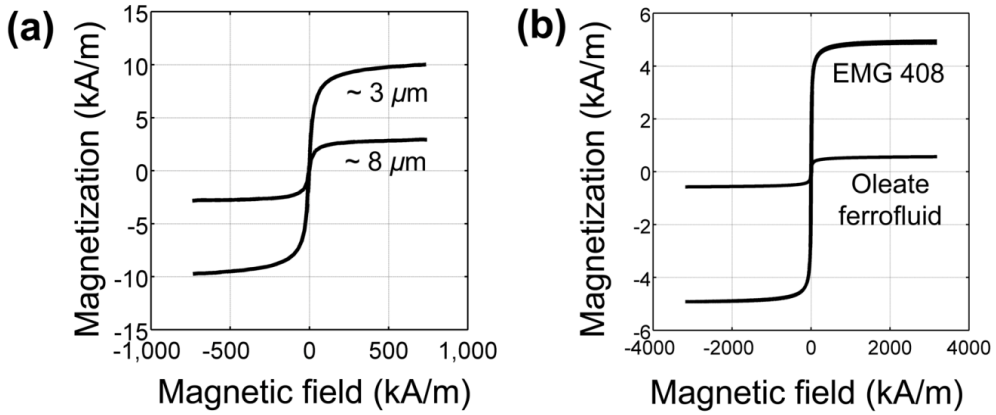

Figure 35. Direct current (DC) magnetization curve (quasistatic) of the magnetic particles (a) and ferrofluids (b).

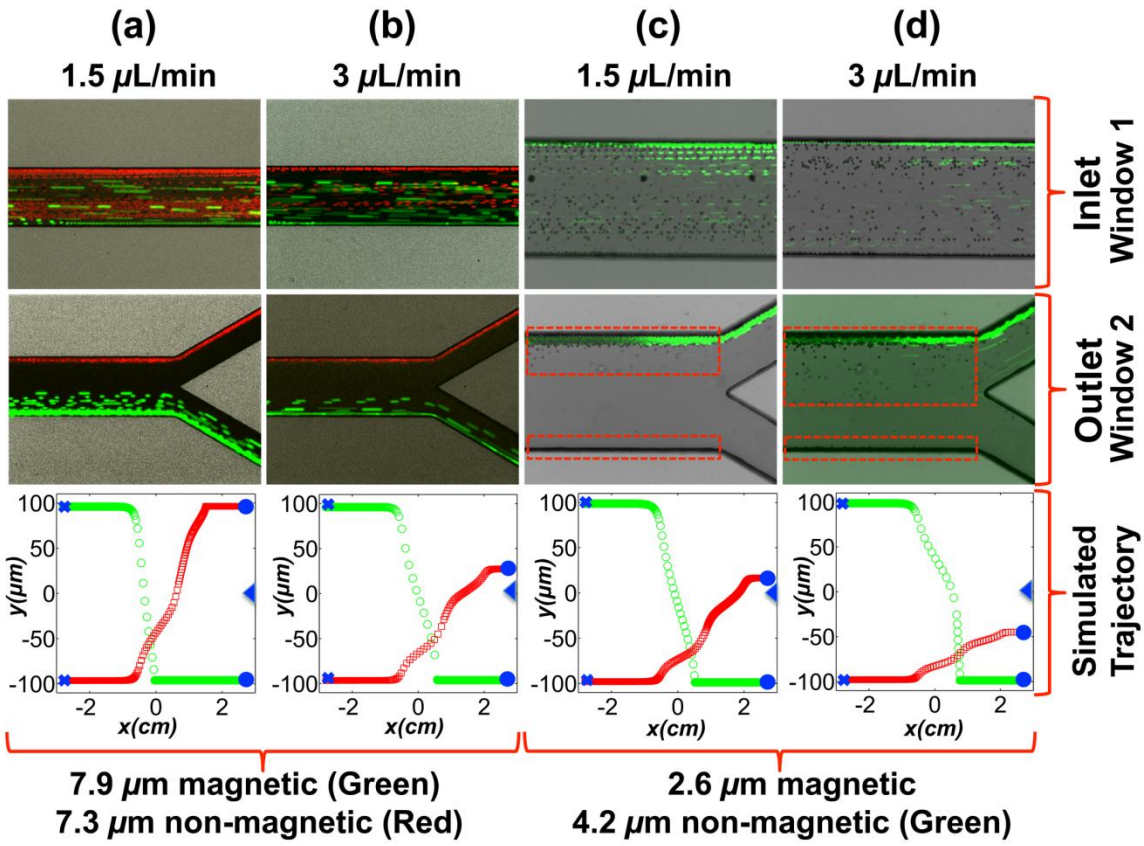

Figure 36. Experimental composite micrographs of the separation process between non-magnetic and magnetic particles and simulated particles' trajectories. (a) and (b) are mixture of 7.3 μm non-magnetic and 7.9 μm magnetic at flow rates of 1.5 μL/min and 3 μL/min, respecitvely. (c) and (d) are mixture of 4.2 μm non-magnetic and 2.6 μm magnetic at flow rates of 1.5 μL/min and 3 μL/min, respecitvely. Top image is at obervation window 1, middle image is at obervation window 2, and bottom plot is simulated trajectoy of the particles when magnetic fiels is present. Crosses indicate starting points, while solid circles indicate ending points of simulated particles' trajectories. Blue triangle in simulated trajectory plots indicates the boundary between outlets. Channel width is 200 μm.

The average magnetic field strength within the microchannel is estimated to be on the order of 10 kA/m, as shown in Figure 31. Under this field, the magnetization of the ferrofluid stabilized by sodium oleate falls between that of non-magnetic particles and magnetic particles, which enables us to separate them in this ferrofluid as a first demonstration of combining positive and negative magnetophoresis. Furthermore, the magnetization of the commercial EMG 408 ferrofluid falls between that of the magnetic particle with ~8 μm diameter and the magnetic particle with ~3 μm diameter. We will use them as a second demonstration to separate particles with different magnetic properties.

We first demonstrate the separation of 7.3 μm non-magnetic particles (red fluorescent) and 7.9 μm magnetic particles (green fluorescent) in the ferrofluid stabilized by sodium oleate, as shown in Figures 33(a) and (b). We introduce a ferrofluid/particle mixture into the microfluidic channel inlet A at a constant flow rate of 1.5 μl/min. An observation window is located at before the left edge of the magnet (window 1) ,and another at the outlets (window 2), as indicated in Figure 30(c). The top image of Figure 33(a) records particles' trajectories close to the inlet at window 1. Prior to window 1, the magnetic field and its gradient are present but significantly smaller than those of the area right on top of the magnet, resulting in a smaller magnitude of magnetic buoyancy forces in *y*-direction (vertical to the flow direction) on both non-magnetic and magnetic particles. Both particles are thus observed in fluorescent mode flowing together across the channel width. On the other hand, middle image of Figure 33(a) records particles' trajectories close to the outlets at window 2. Between windows 1 and 2, both particles experience significant magnetic buoyancy force on them because of the larger magnetic field and its gradient in *y*-direction. The force on non-magnetic particles is pointing in

positive *y*-direction (weaker field direction) due to negative magnetophoresis, while the force on magnetic particles is pointing in negative *y*-direction (stronger field direction) due to positive magnetophoresis. This leads to the spatial separation of two types of particles at the outlets, which is also confirmed by the simulation result in the bottom plot of Figure 33(a). Similar separation phenomenon still exists at an increased flow rate of 3 μl/min, as shown in Figure 33(b).

We then demonstrate the separation of 4.2 μm non-magnetic particles (green fluorescent) and 2.6 μm magnetic particles in the same ferrofluid. 2.6 μm magnetic particles are fluorescently red. However, since their fluorescence alone is weak and difficult to observe in our microscope setup, we instead choose to use a combination of both bright-field and fluorescent modes microscopy to record the separation process. Figures 33(c) and 33(d) record the process at windows 1 and 2 with flow rates of 1.5 and 3 μl/min. In both cases, magnetic particles are separated from non-magnetic particles. However at the increased flow rate of 3 μl/min, the width of the non-magnetic particle stream expands and some of non-magnetic particles exit the channel through the bottom outlet, which is predicted by the 3D simulation in the bottom plot of Figure 33(d).

We move onto the demonstration of separating of 8.2 μm magnetic particles (saturation magnetization ~2,939 A/m) and 2.8 μm magnetic particles (saturation magnetization ~10,019 A/m) in the EMG 408 ferrofluid (saturation magnetization 4,953 A/m), as shown in Figure 34. Again we emphasize that the magnetization values of particles are provided by the manufacturer and are measured on a specific batch of sample. Actual magnetization of the sample used in this experiment may vary from these values. A more precise way to obtain magnetization curves of these particles is to

measure them using VSM. However, because of the cost of the sample, we choose to use the manufacturer data and leave the VSM measurement to the time when precise magnetization curves are needed. The EMG 408 commercial ferrofluid has a saturation magnetization of 4,953 A/m that falls roughly halfway between the ones of 8.2 μm and 2.8 μm magnetic particles, making it ideal to separate them.

We introduce ferrofluids/particles mixture into the microfluidic channel inlet A at constant flow rates of 1.5, 3 and 4.5 μl/min. The trajectories of particles are recorded and compared at windows 1 and 2 between the cases when a magnetic field is and is not present. Figure 34(a) show the comparison at a 1.5 μl/min flow rate. When the magnetic field is not present, magnetic particles flow together in the microchannel and exit the channel through both outlets as expected. As soon as the magnetic field is present, a clear migration of 2.8 μm particles towards the stronger field direction and 8.2 μm particles towards the weaker field direction are observed. Streams of both particles are labeled with red dashed boxes on Figure 34(a). The migration of particles towards different directions is the evidence that both positive and negative magnetophoresis exist in this system, as confirmed by the simulation particle trajectory using our 3D model. We exploit it to separate magnetic particles solely based on their magnetic properties, regardless of their sizes. Figure 34(b) show the comparison case at a 3 μl/min flow rate where similar separation process is observed. Increasing the flow rate further to 4.5 μl/min results in shorter residual time of particles in the channel, which leads to the expansion of the width of 2.8 μm particles, as shown in Figure 34(c).

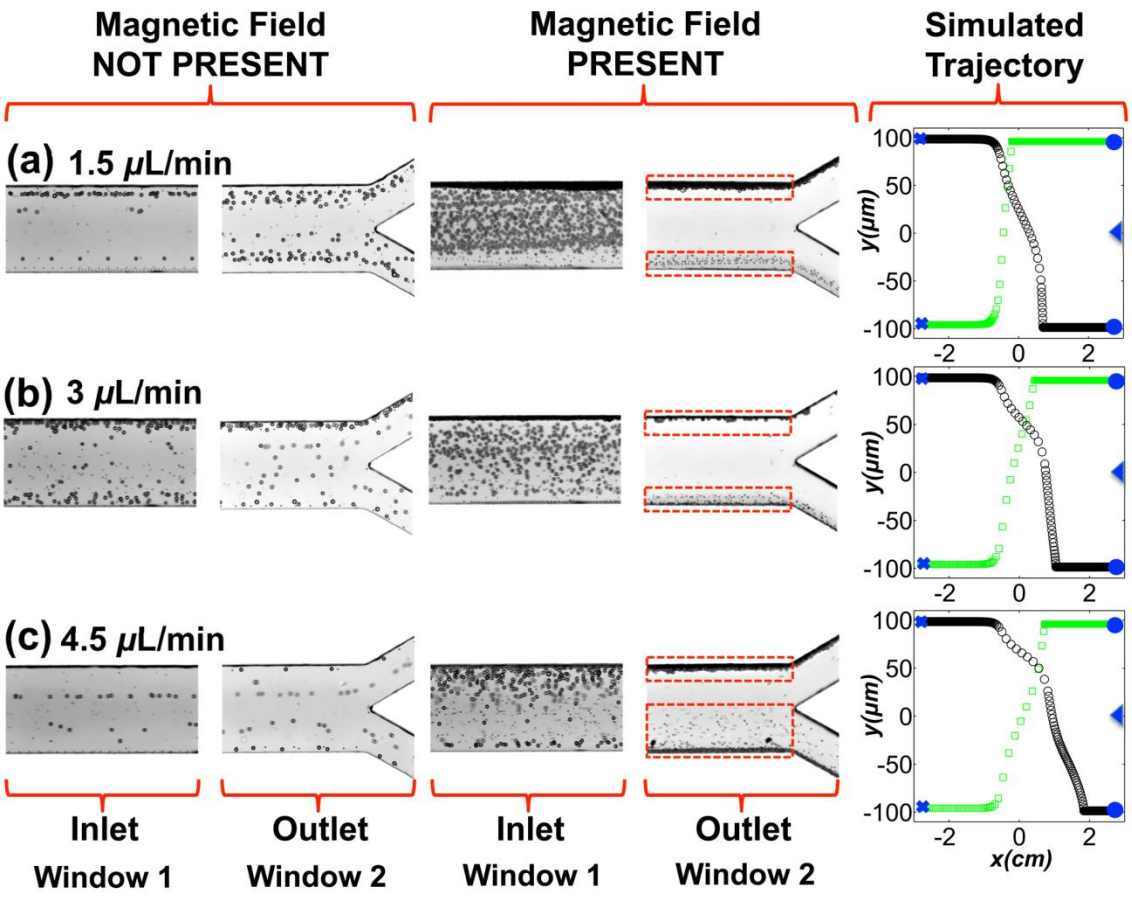

Figure 37. Experimental composite micrographs of the separation process between particles with different magnetic properties and simulated particles' trajectories. Mixture of 2.8 μm strongly magnetic and 8.2 μm weakly magnetic particles are recorded at flow rates of (a) 1.5 μL/min, (a) 3 μL/min and (a) 4.5 μL/min, respecitvely. Left images are at obervation windows 1 and 2 when magnetic fiels is not present, middle images are at obervation windows 1 and 2 when magnetic fiels is present, and right plot is simulated trajectoy of the particles when magnetic fiels is present. Crosses indicate starting points, while solid circles indicate ending points of simulated particles' trajectories. Blue triangle in simulated trajectory plots indicates the boundary between outlets. Channel width is 200 μm.

CHAPTER 8

CONCLUDING DISCUSSION

In this dissertation, we have developed a novel magnetic manipulation technique for non-magnetic microparticles transportation in a label free manner. The platform consists of a microchannel and permanent magnets. In chapter 2, we built an analytical model based on manipulation of non-magnetic particles in ferrofluids in a microfluidic system both theoretically and experimentally. The permanent magnet produced a spatially non-uniform magnetic field that gave rise to a magnetic buoyancy force on particles within the ferrofluid-filled microchannel. We derived the equations of motions for particles using analytical expressions for dominant magnetic buoyancy and hydrodynamic viscous drag forces. The results from the model indicated that the particles would be increasingly deflected in the direction that was perpendicular to the flow when the size of the particles increased, or when the flow rate in the microchannel decreased. "Wall effect" has shown significant consequence on the trajectories and overall deflections of particles. Experimental results confirmed the validity of our analytical model. The analytical model is simple, easy to implement, and useful for quick optimization of future separation and manipulation devices that are based on ferrofluids.

Then we applied this principle to microparticles focusing inside a microfluidic channel in chapter 3. In comparison to other particle focusing techniques, including hydrodynamic, electrokinetic, optical, dielectrophoretic and acoustic focusing, this method is simple, low-cost, and label-free. The construction of our device is extremely

simple, and we choose permanent magnet based device configurations because they eliminate complex microfabrication process and auxiliary power supply. The devices are easy to operate and do not generate heat. Microparticles do not require labeling steps because their surrounding media – ferrofluids – are magnetic by themselves. The ferrofluid used in this method are colloidal suspensions of iron oxide nanoparticles, which have reduced interferences with biological processes of samples compared to paramagnetic salt solutions. With recent developments of bio-compatible ferrofluids [48, 134, 155], this technique can also be applied towards cell focusing and manipulation.

Based on these findings, we have also designed a new size based microparticle separation approach using ferrofluids. We have shown label-free binary particles separation in a continuous flow microfluidic device with high throughput and efficiency. The results presented here demonstrate the potential of continuous separation of non-magnetic object inside ferrofluids within microfluidic devices. Separation of particles is also possible through existing techniques such as dielectrophoresis, optical force, and magnetic bead labeling methods. However, construction of our device is simple and low-cost; we choose to use permanent magnets instead of integrated electrodes to eliminate complex microfabrication process and auxiliary power supply.

This platform was further exploited for separating *Escherichia coli* and *Saccharomyces cerevisiae* cells in Chapter 4. Non-magnetic polystyrene microparticles of similar sizes were first used for calibration and testing. A commercial magnetite ferrofluid was used to separate particle and cell mixtures. Ferrofluids are opaque due to light diffraction from their high concentration of magnetic nanoparticles. Fluorescent cells need to be close to channel surface for microscopic recording. In order to address

this issue, ferrofluids with low solid content, as well as shallow microfluidic channel, are favored for cell manipulation. In addition, magnetic fields can be used to push cells onto channel surface, increasing visibility of cells in fluorescent mode. In this study, we use a combination of both bright-field and fluorescent modes microscopy to circumvent the opaqueness issue. Cells were readily visible in a shallow channel in bright field micrographs. Current sorting throughput is 10^7 cells/hour, and sorting efficiency is close to 100%. We envision this device can achieve up to two orders higher throughput while still maintaining current sorting efficiency.

The same principle can also be used for mammalian cells sorting and enrichment. To meet the stringent requirement of maintaining mammalian cell viability, we developed a novel ferrofluids that can maintain the cancer cell viability for hours. Then we extended this methodology to cancer cells separation, particularly human specimens such as blood and other bodily fluids, exfoliated neoplastic cells, and tumor aspirates.

To further extend the capabilities of the ferrohydrodynamic platform, we develop a new separation method based on particles' magnetic properties through combining positive and negative magnetophoresis in a ferrofluid in chapter 7. The principle of this method is to use a ferrofluid with its magnetization between that of the particles, which leads to particles with larger magnetization being attracted and the ones with smaller magnetization being pushed away from the maxima of magnetic fields. Using this method, we demonstrate the separation of magnetic and non-magnetic particles in a custom-made ferrofluid. We also demonstrate the separation of particles with different magnetic properties in a commercial ferrofluid. We picture this method can be used to separate particles or cells with smaller difference in their magnetic properties than the

case demonstrated in this paper using ferrofluids of tunable concentrations. A potential application as well as a future work of this method is to apply it as a miniaturized measurement platform for characterizing magnetizations of microparticles or cells. In such a platform, particles or cells with different magnetizations will be introduced into a microchannel where a linear gradient of ferrofluids is created across the channel width. Under a non-uniform magnetic field, they will keep migrating across the channel width because of the magnetic buoyancy force until their magnetization equals the surrounding ferrofluid and the resulting magnetic buoyancy force vanishes. As a result, the steady-state position of the particles and cells reveals their magnetization under a specific magnetic field. By varying the field strength, a series of magnetization values can be obtained and used to construct a magnetization curve for these particles or cells. We envision such a platform providing a low-cost and fast alternative to traditional macro-scale magnetization measurement systems.

The ferrohydrodynamic cell sorting scheme offers the potential for high throughput (~10^7 cells/hour in this study and ~10^9 cells/hour in theory) and high separation efficiency (~100%) that are comparable to existing microfluidic sorting techniques but without the use of labels. Sorting specificity of this approach is not limited to size difference only; it is also sensitive to cells' shape and deformability [48]. In adapting it to miniaturized flow cytometry, ferrohydrodynamic manipulation can first focus cells into single cell streams before sorting, eliminating needs for excessive sheath flow and preventing sample dilution [112]. Compared to paramagnetic solution based sorting, ferrofluid offers much higher magnetic susceptibility, eliminating needs for either

microfabricated ferromagnetic structures to enhance field gradient or hypertonic concentrations of paramagnetic salts that are not biocompatible for live cell manipulation.

REFERENCES

1. Li, J.; Zhang, Z.; Rosenzweig, J.; Wang, Y. Y.; Chan, D. W., Proteomics and Bioinformatics Approaches for Identification of Serum Biomarkers to Detect Breast Cancer. *Clinical Chemistry* **2002,** *48*, 1296-1304.

2. Nagrath, S.; Sequist, L. V.; Maheswaran, S.; Bell, D. W.; Irimia, D.; Ulkus, L.; Smith, M. R.; Kwak, E. L.; Digumarthy, S.; Muzikansky, A.; Ryan, P.; Balis, U. J.; Tompkins, R. G.; Haber, D. A.; Toner, M., Isolation of rare circulating tumour cells in cancer patients by microchip technology. *Nature* **2007,** *450*, 1235-U10.

3. Toner, M.; Irimia, D., Blood-on-a-chip. *Annu Rev Biomed Eng* **2005,** *7*, 77-103.

4. Yung, C. W.; Fiering, J.; Mueller, A. J.; Ingber, D. E., Micromagnetic-microfluidic blood cleansing device. *Lab on a Chip* **2009,** *9*, 1171-1177.

5. Easley, C. J.; Karlinsey, J. M.; Bienvenue, J. M.; Legendre, L. A.; Roper, M. G.; Feldman, S. H.; Hughes, M. A.; Hewlett, E. L.; Merkel, T. J.; Ferrance, J. P.; Landers, J. P., A fully integrated microfluidic genetic analysis system with sample-in–answer-out capability. *Proceedings of the National Academy of Sciences* **2006,** *103*, 19272-19277.

6. Cho, Y.-K.; Lee, J.-G.; Park, J.-M.; Lee, B.-S.; Lee, Y.; Ko, C., One-step pathogen specific DNA extraction from whole blood on a centrifugal microfluidic device. *Lab on a Chip* **2007,** *7*, 565-573.

7. Pamme, N., Continuous flow separations in microfluidic devices. *Lab on a Chip* **2007,** *7*, 1644-1659.

8. Tsutsui, H.; Ho, C. M., Cell separation by non-inertial force fields in microfluidic systems. *Mech Res Commun* **2009,** *36*, 92-103.

9. Gossett, D. R.; Weaver, W. M.; Mach, A. J.; Hur, S. C.; Tse, H. T. K.; Lee, W.; Amini, H.; Di Carlo, D., Label-free cell separation and sorting in microfluidic systems. *Anal Bioanal Chem* **2010,** *397*, 3249-3267.

10. Bonner, W. A.; Hulett, H. R.; Sweet, R. G.; Herzenberg, L. A., Fluorescence activated cell sorting. *Rev Sci Instrum* **1972,** *43*, 404-9.

11. Miltenyi, S.; Muller, W.; Weichel, W.; Radbruch, A., High gradient magnetic cell separation with MACS. *Cytometry* **1990,** *11*, 231-8.

12. Label-free cell separation and sorting in microfluidic systems. *Anal Bioanal Chem* **2010**.

13. Yamada, M.; Nakashima, M.; Seki, M., Pinched flow fractionation: Continuous size separation of particles utilizing a laminar flow profile in a pinched microchannel. *Anal. Chem.* **2004,** *76*, 5465-5471.

14. Yamada, M.; Seki, M., Hydrodynamic filtration for on-chip particle concentration and classification utilizing microfluidics. *Lab Chip* **2005,** *5*, 1233-9.

15. Huang, L. R.; Cox, E. C.; Austin, R. H.; Sturm, J. C., Continuous particle separation through deterministic lateral displacement. *Science* **2004,** *304*, 987-90.

16. Davis, J. A.; Inglis, D. W.; Morton, K. J.; Lawrence, D. A.; Huang, L. R.; Chou, S. Y.; Sturm, J. C.; Austin, R. H., Deterministic hydrodynamics: taking blood apart. *Proc Natl Acad Sci U S A* **2006,** *103*, 14779-84.

17. Di Carlo, D., Inertial microfluidics. *Lab on a Chip* **2009,** *9*, 3038-3046.

18. Laurell, T.; Petersson, F.; Nilsson, A., Chip integrated strategies for acoustic separation and manipulation of cells and particles. *Chem Soc Rev* **2007,** *36*, 492-506.

19. Petersson, F.; Åberg, L.; Swärd-Nilsson, A.-M.; Laurell, T., Free Flow Acoustophoresis: Microfluidic-Based Mode of Particle and Cell Separation. *Anal Chem* **2007,** *79*, 5117-5123.

20. Voldman, J., Electrical forces for microscale cell manipulation. *Annu Rev Biomed Eng* **2006,** *8*, 425-54.

21. MacDonald, M. P.; Spalding, G. C.; Dholakia, K., Microfluidic sorting in an optical lattice. *Nature* **2003,** *426*, 421-4.

22. Pamme, N.; Manz, A., On-chip free-flow magnetophoresis: Continuous flow separation of magnetic particles and agglomerates. *Anal Chem* **2004,** *76*, 7250-7256.

23. Pamme, N., Magnetism and microfluidics. *Lab on a Chip* **2006,** *6*, 24-38.

24. Pamme, N.; Wilhelm, C., Continuous sorting of magnetic cells via on-chip free-flow magnetophoresis. *Lab on a Chip* **2006,** *6*, 974-980.

25. Schüler, D.; Frankel, R. B., Bacterial magnetosomes: microbiology, biomineralization and biotechnological applications. *Appl Microbiol Biotechnol* **1999,** *52*, 464-473.

26. Zborowski, M.; Ostera, G. R.; Moore, L. R.; Milliron, S.; Chalmers, J. J.; Schechter, A. N., Red blood cell magnetophoresis. *Biophys J* **2003,** *84*, 2638-2645.

27. Han, K.-H.; Bruno Frazier, A., Continuous magnetophoretic separation of blood cells in microdevice format. *J Appl Phys* **2004,** *96*, 5797-5802.

28. Lee, H.; Purdon, A. M.; Chu, V.; Westervelt, R. M., Controlled assembly of magnetic nanoparticles from magnetotactic bacteria using microelectromagnets arrays. *Nano Lett* **2004,** *4*, 995-998.

29. Liu, C. X.; Stakenborg, T.; Peeters, S.; Lagae, L., Cell manipulation with magnetic particles toward microfluidic cytometry. *J Appl Phys* **2009,** *105*.

30. Gijs, M. A. M.; Lacharme, F.; Lehmann, U., Microfluidic Applications of Magnetic Particles for Biological Analysis and Catalysis. *Chem Rev* **2010,** *110*, 1518-1563.

31. Hafeli, U.; Schutt, W.; Teller, J.; Zborowski, M., *Scientific and clinical applications of magnetic carriers*. Springer: New York, 1997.

32. Miller, M. M.; Sheehan, P. E.; Edelstein, R. L.; Tamanaha, C. R.; Zhong, L.; Bounnak, S.; Whitman, L. J.; Colton, R. J., A DNA array sensor utilizing magnetic microbeads and magnetoelectronic detection. *J. Magn. Magn. Mater.* **2001,** *225*, 138-144.

33. Rife, J. C.; Miller, M. M.; Sheehan, P. E.; Tamanaha, C. R.; Tondra, M.; Whitman, L. J., Design and performance of GMR sensors for the detection of magnetic microbeads in biosensors. *Sensors and Actuators a-Physical* **2003,** *107*, 209-218.

34. Mihajlovic, G.; Aledealat, K.; Xiong, P.; Von Molnar, S.; Field, M.; Sullivan, G. J., Magnetic characterization of a single superparamagnetic bead by phase-sensitive micro-Hall magnetometry. *Applied Physics Letters* **2007,** *91*, -.

35. Shevkoplyas, S. S.; Siegel, A. C.; Westervelt, R. M.; Prentiss, M. G.; Whitesides, G. M., The force acting on a superparamagnetic bead due to an applied magnetic field. *Lab Chip* **2007,** *7*, 1294-1302.

36. Kitchener, H. C.; Blanks, R.; Dunn, G.; Gunn, L.; Desai, M.; Albrow, R.; Mather, J.; Rana, D. N.; Cubie, H.; Moore, C.; Legood, R.; Gray, A.; Moss, S., Automation-assisted versus manual reading of cervical cytology (MAVARIC): a randomised controlled trial. *Lancet Oncol* **2011,** *12*, 56-64.

37. Anttila, A.; Pokhrel, A.; Kotaniemi-Talonen, L.; Hakama, M.; Malila, N.; Nieminen, P., Cervical cancer patterns with automation-assisted and conventional cytological screening: a randomized study. *Int J Cancer* **2011,** *128*, 1204-12.

38. Nieminen, P.; Kotaniemi, L.; Hakama, M.; Tarkkanen, J.; Martikainen, J.; Toivonen, T.; Ikkala, J.; Luostarinen, T.; Anttila, A., A randomised public-health trial on automation-assisted screening for cervical cancer in Finland: performance with 470,000 invitations. *Int J Cancer* **2005,** *115*, 307-11.

39. Rosensweig, R. E., *Ferrohydrodynamics*. Cambridge University Press: Cambridge, 1985.

40. Odenbach, S.; Editor, *Ferrofluids: Magnetically Controllable Fluids and Their Applications*. 2002; p 251 pp.

41. Odenbach, S., *Colloidal magnetic fluids - basics, development and applications of ferrofluids*. Springer: Berlin, 2009.

42. Odenbach, S., *Magnetoviscous Effects in Ferrofluids*. 2002; p No pp given.

43. Skjeltorp, A. T., One- and two-dimensional crystallization of magnetic holes. *Phys. Rev. Lett.* **1983,** *51*, 2306-9.

44. Skjeltorp, A. T., Ordering phenomena of particles dispersed in magnetic fluids. *J. Appl. Phys.* **1985,** *57*, 3285-90.

45. Fannin, P. C.; Charles, S. W.; Skjeltorp, A. T., Apparent superdiamagnetism of diamagnetic spheres in ferrofluids. *J. Magn. Magn. Mater.* **1999,** *201*, 113-115.

46. Skjeltorp, A. T.; Akselvoll, J.; de Lange Kristiansen, K.; Helgesen, G.; Toussaint, R.; Flekkoey, E. G.; Cernak, J., Self-assembly and dynamics of magnetic holes. *Los Alamos National Laboratory, Preprint Archive, Condensed Matter* **2006**, 1-15, arXiv:cond-mat/0611008.

47. Helgesen, G.; Svaasand, E.; Skjeltorp, A. T., Nanoparticle induced self-assembly. *Journal of Physics: Condensed Matter* **2008,** *20*, 204127/1-204127/6.

48. Kose, A. R.; Fischer, B.; Mao, L.; Koser, H., Label-free cellular manipulation and sorting via biocompatible ferrofluids. *P Natl Acad Sci USA* **2009,** *106*, 21478-21483.

49. Zhu, T., Marrero, F., Mao, L.,, Continuous separation of non-magnetic particles inside ferrofluids. *Microfluid Nanofluid* **2010,** *9*, 1003-1009.

50. Krebs Melissa, D.; Erb Randall, M.; Yellen Benjamin, B.; Samanta, B.; Bajaj, A.; Rotello Vincent, M.; Alsberg, E., Formation of ordered cellular structures in suspension via label-free negative magnetophoresis. *Nano Lett* **2009,** *9*, 1812-7.

51. Zhu, T.; Cheng, R.; Mao, L., Focusing Microparticles in a Microfluidic Channel with Ferrofluids. *Microfluidics and Nanofluidics* **2011**.

52. Rosensweig, R. E., Fluidmagnetic buoyancy. *AIAA Journal* **1966,** *4*, 1751-1758.

53. Jones, T. B., *Electromechanics of Particles*. Cambridge University Press: Cambridge, 1995.

54. Krebs, M. D.; Erb, R. M.; Yellen, B. B.; Samanta, B.; Bajaj, A.; Rotello, V. M.; Alsberg, E., Formation of Ordered Cellular Structures in Suspension via Label-Free Negative Magnetophoresis. *Nano Lett* **2009,** *9*, 1812-1817.

55. Rodriguez-Villarreal, A. I.; Tarn, M. D.; Madden, L. A.; Lutz, J. B.; Greenman, J.; Samitier, J.; Pamme, N., Flow focussing of particles and cells based on their intrinsic properties using a simple diamagnetic repulsion setup. *Lab on a Chip* **2011,** *11*, 1240-1248.

56. Peyman, S. A.; Kwan, E. Y.; Margarson, O.; Iles, A.; Pamme, N., Diamagnetic repulsion—A versatile tool for label-free particle handling in microfluidic devices. *Journal of Chromatography A* **2009,** *1216*, 9055-9062.

57. Zhu, J. J.; Liang, L. T.; Xuan, X. C., On-chip manipulation of nonmagnetic particles in paramagnetic solutions using embedded permanent magnets. *Microfluid Nanofluid* **2012,** *12*, 65-73.

58. Tarn, M. D.; Peyman, S. A.; Pamme, N., Simultaneous trapping of magnetic and diamagnetic particle plugs for separations and bioassays. *RSC Advances* **2013,** *3*, 7209-7214.

59. Tarn, M. D.; Hirota, N.; Iles, A.; Pamme, N., On-chip diamagnetic repulsion in continuous flow. *Sci Technol Adv Mat* **2009,** *10*.

60. Vojtíšek, M.; Tarn, M.; Hirota, N.; Pamme, N., Microfluidic devices in superconducting magnets: on-chip free-flow diamagnetophoresis of polymer particles and bubbles. *Microfluid Nanofluid* **2012,** *13*, 625-635.

61. Winkleman, A.; Perez-Castillejos, R.; Gudiksen, K. L.; Phillips, S. T.; Prentiss, M.; Whitesides, G. M., Density-based diamagnetic separation: Devices for detecting binding events and for collecting unlabeled diamagnetic particles in paramagnetic solutions. *Analytical Chemistry* **2007,** *79*, 6542-6550.

62. Mirica, K. A.; Shevkoplyas, S. S.; Phillips, S. T.; Gupta, M.; Whitesides, G. M., Measuring Densities of Solids and Liquids Using Magnetic Levitation: Fundamentals. *J Am Chem Soc* **2009,** *131*, 10049-10058.

63. Kauffmann, P.; Ith, A.; O'Brien, D.; Gaude, V.; Boue, F.; Combe, S.; Bruckert, F.; Schaack, B.; Dempsey, N. M.; Haguet, V.; Reyne, G., Diamagnetically trapped arrays of living cells above micromagnets. *Lab on a Chip* **2011,** *11*, 3153-3161.

64. Shen, F.; Hwang, H.; Hahn, Y. K.; Park, J. K., Label-Free Cell Separation Using a Tunable Magnetophoretic Repulsion Force. *Anal Chem* **2012,** *84*, 3075-3081.

65. Andres, U. T., Magnetic liquids. *Materials Science and Engineering* **1976,** *26*, 269-275.

66. Zhu, T. T.; Marrero, F.; Mao, L. D., Continuous separation of non-magnetic particles inside ferrofluids. *Microfluid Nanofluid* **2010,** *9*, 1003-1009.

67. Zhu, T. T.; Cheng, R.; Lee, S. A.; Rajaraman, E.; Eiteman, M. A.; Querec, T. D.; Unger, E. R.; Mao, L. D., Continuous-flow ferrohydrodynamic sorting of particles and cells in microfluidic devices. *Microfluid Nanofluid* **2012,** *13*, 645-654.

68. Zhu, T.; Cheng, R.; Mao, L., Focusing microparticles in a microfluidic channel with ferrofluids. *Microfluid Nanofluid* **2011,** *11*, 695-701.

69. Zhu, T. T.; Lichlyter, D. J.; Haidekker, M. A.; Mao, L. D., Analytical model of microfluidic transport of non-magnetic particles in ferrofluids under the influence of a permanent magnet. *Microfluid Nanofluid* **2011,** *10*, 1233-1245.

70. Yellen Benjamin, B.; Hovorka, O.; Friedman, G., Arranging matter by magnetic nanoparticle assemblers. *Proc Natl Acad Sci U S A* **2005,** *102*, 8860-4.

71. Xia, Y.; Whitesides, G. M., Soft lithography. *Annu Rev Mater Sci* **1998,** *28*, 153-184.

72. Pankhurst, Q. A.; Connolly, J.; Jones, S. K.; Dobson, J., Applications of magnetic nanoparticles in biomedicine. *Journal of Physics D: Applied Physics* **2003**, R167.

73. Pham, P.; Massé, P.; Berthier, J., Numerical modeling of superparamagnetic sub-micronic particles trajectories under the coupled action of 3D force fields. *The European Physical Journal - Applied Physics* **2000,** *12*, 211-216.

74. Smistrup, K.; Hansen, O.; Bruus, H.; Hansen, M. F., Magnetic separation in microfluidic systems using microfabricated electromagnets—experiments and simulations. *J Magn Magn Mater* **2005,** *293*, 597-604.

75. Gassner, A.-L.; Abonnenc, M.; Chen, H.-X.; Morandini, J.; Josserand, J.; Rossier, J. S.; Busnel, J.-M.; Girault, H. H., Magnetic forces produced by rectangular permanent magnets in static microsystems. *Lab on a Chip* **2009,** *9*, 2356-2363.

76. Furlani, E. P., Analysis of particle transport in a magnetophoretic microsystem. *J Appl Phys* **2006,** *99*, -.

77. Furlani, E. P.; Sahoo, Y., Analytical model for the magnetic field and force in a magnetophoretic microsystem. *J Phys D Appl Phys* **2006,** *39*, 1724-1732.

78. Ganatos, P.; Pfeffer, R.; Weinbaum, S., A Strong Interaction Theory for the Creeping Motion of a Sphere between Plane Parallel Boundaries .2. Parallel Motion. *Journal of Fluid Mechanics* **1980,** *99*, 755-783.

79. Krishnan, G. P.; Leighton, D. T., Inertial Lift on a Moving Sphere in Contact with a Plane Wall in a Shear-Flow. *Physics of Fluids* **1995,** *7*, 2538-2545.

80. Wirix-Speetjens, R.; Fyen, W.; Kaidong, X.; De Boeck, J.; Borghs, G., A force study of on-chip magnetic particle transport based on tapered conductors. *Magnetics, IEEE Transactions on* **2005,** *41*, 4128-4133.

81. Leighton, D.; Acrivos, A., The lift on a small sphere touching a plane in the presence of a simple shear flow. *Z. angew. Math. Phys.* **1985,** *36*, 174-178.

82. A., E., *Investigations on the Theory of Brownian Motion*. Dover: New York, 1956.

83. WM, D., Analysis of transport phenomena. *Oxford University Press, New York* **1998**.

84. Brody, J. P.; Yager, P.; Goldstein, R. E.; Austin, R. H., Biotechnology at low Reynolds numbers. *Biophys J* **1996,** *71*, 3430-3441.

85. Ichikawa, N.; Hosokawa, K.; Maeda, R., Interface motion of capillary-driven flow in rectangular microchannel. *Journal of Colloid and Interface Science* **2004,** *280*, 155-164.

86. Whitesides, G. M., The origins and the future of microfluidics. *Nature* **2006,** *442*, 368-373.

87. Pamme, N., Continuous flow separations in microfluidic devices. *Lab Chip* **2007,** *7*, 1644-1659.

88. Lee, G. B.; Chang, C. C.; Huang, S. B.; Yang, R. J., The hydrodynamic focusing effect inside rectangular microchannels. *J Micromech Microeng* **2006,** *16*, 1024-1032.

89. Kummrow, A.; Theisen, J.; Frankowski, M.; Tuchscheerer, A.; Yildirim, H.; Brattke, K.; Schmidt, M.; Neukammer, J., Microfluidic structures for flow cytometric

analysis of hydrodynamically focussed blood cells fabricated by ultraprecision micromachining. *Lab on a Chip* **2009,** *9*, 972-981.

90. Xuan, X. C.; Li, D. Q., Focused electrophoretic motion and selected electrokinetic dispensing of particles and cells in cross-microchannels. *Electrophoresis* **2005,** *26*, 3552-3560.

91. Zhao, Y. Q.; Fujimoto, B. S.; Jeffries, G. D. M.; Schiro, P. G.; Chiu, D. T., Optical gradient flow focusing. *Opt Express* **2007,** *15*, 6167-6176.

92. Wang, L.; Flanagan, L. A.; Jeon, N. L.; Monuki, E.; Lee, A. P., Dielectrophoresis switching with vertical sidewall electrodes for microfluidic flow cytometry. *Lab on a Chip* **2007,** *7*, 1114-1120.

93. Zhu, J. J.; Xuan, X. C., Dielectrophoretic focusing of particles in a microchannel constriction using DC-biased AC flectric fields. *Electrophoresis* **2009,** *30*, 2668-2675.

94. Petersson, F.; Nilsson, A.; Holm, C.; Jonsson, H.; Laurell, T., Continuous separation of lipid particles from erythrocytes by means of laminar flow and acoustic standing wave forces. *Lab on a Chip* **2005,** *5*, 20-22.

95. Shi, J. J.; Mao, X. L.; Ahmed, D.; Colletti, A.; Huang, T. J., Focusing microparticles in a microfluidic channel with standing surface acoustic waves (SSAW). *Lab on a Chip* **2008,** *8*, 221-223.

96. Huh, D.; Gu, W.; Kamotani, Y.; Grotberg, J. B.; Takayama, S., Microfluidics for flow cytometric analysis of cells and particles. *Physiological Measurement* **2005,** *26*, R73-R98.

97. Chung, T. D.; Kim, H. C., Recent advances in miniaturized microfluidic flow cytometry for clinical use. *Electrophoresis* **2007,** *28*, 4511-4520.

98. Xuan, X. C.; Zhu, J. J.; Church, C., Particle focusing in microfluidic devices. *Microfluid Nanofluid* **2010,** *9*, 1-16.

99. Afshar, R.; Moser, Y.; Lehnert, T.; Gijs, M. A. M., Three-Dimensional Magnetic Focusing of Superparamagnetic Beads for On-Chip Agglutination Assays. *Anal Chem* **2011,** *83*, 1022-1029.

100. Pamme, N., Magnetism and microfluidics. *Lab Chip* **2006,** *6*, 24-38.

101. Liu, C.; Stakenborg, T.; Peeters, S.; Lagae, L., Cell manipulation with magnetic particles toward microfluidic cytometry. *J. Appl. Phys.* **2009,** *105*, 102014-11.

102. Adair, R. K., Constraints on Biological Effects of Weak Extremely-Low-Frequency Electromagnetic-Fields. *Phys Rev A* **1991,** *43*, 1039-1048.

103. Pankhurst, Q. A.; Thanh, N. K. T.; Jones, S. K.; Dobson, J., Progress in applications of magnetic nanoparticles in biomedicine. *J Phys D Appl Phys* **2009,** *42*, -.

104. Krishnan, K. M., Biomedical Nanomagnetics: A Spin Through Possibilities in Imaging, Diagnostics, and Therapy. *IEEE Trans. Magn.* **2010,** *46*, 2523-2558.

105. Yellen, B. B.; Hovorka, O.; Friedman, G., Arranging matter by magnetic nanoparticle assemblers. *Proc. Natl. Acad. Sci. U. S. A.* **2005,** *102*, 8860-8864.

106. Staben, M. E.; Zinchenko, A. Z.; Davis, R. H., Motion of a particle between two parallel plane walls in low-Reynolds-number Poiseuille flow. *Physics of Fluids* **2003,** *15*, 1711-1733.

107. Gerber, R.; Takayasu, M.; Friedlaender, F., Generalization of HGMS theory: The capture of ultra-fine particles. *IEEE Trans. Magn.* **1983,** *19*, 2115-2117.

108. Peyman, S. A.; Iwan, E. Y.; Margarson, O.; Iles, A.; Pamme, N., Diamagnetic repulsion-A versatile tool for label-free particle handling in microfluidic devices. *Journal of Chromatography A* **2009,** *1216*, 9055-9062.

109. Liang, L. T.; Zhu, J. J.; Xuan, X. C., Three-dimensional diamagnetic particle deflection in ferrofluid microchannel flows. *Biomicrofluidics* **2011,** *5*.

110. Shen, F.; Hwang, H.; Hahn, Y. K.; Park, J.-K., Label-Free Cell Separation Using a Tunable Magnetophoretic Repulsion Force. *Anal. Chem.* **2012**.

111. Kose, A. R.; Koser, H., Ferrofluid mediated nanocytometry. *Lab on a Chip* **2012,** *12*, 190-196.

112. Zhu, T. T.; Cheng, R.; Mao, L. D., Focusing microparticles in a microfluidic channel with ferrofluids. *Microfluid Nanofluid* **2011,** *11*, 695-701.

113. Kaya, T.; Koser, H., Characterization of Hydrodynamic Surface Interactions of Escherichia coli Cell Bodies in Shear Flow. *Phys. Rev. Lett.* **2009,** *103*.

114. Jorgensen, P.; Nishikawa, J. L.; Breitkreutz, B. J.; Tyers, M., Systematic identification of pathways that couple cell growth and division in yeast. *Science* **2002,** *297*, 395-400.

115. Kitchener, H. C.; Castle, P. E.; Cox, J. T., Chapter 7: Achievements and limitations of cervical cytology screening. *Vaccine* **2006,** *24 Suppl 3*, S3/63-70.

116. Stoler, M. H.; Schiffman, M., Interobserver reproducibility of cervical cytologic and histologic interpretations: realistic estimates from the ASCUS-LSIL Triage Study. *JAMA* **2001,** *285*, 1500-5.

117. Mayrand, M. H.; Duarte-Franco, E.; Rodrigues, I.; Walter, S. D.; Hanley, J.; Ferenczy, A.; Ratnam, S.; Coutlee, F.; Franco, E. L., Human papillomavirus DNA versus Papanicolaou screening tests for cervical cancer. *N Engl J Med* **2007,** *357*, 1579-88.

118. Naucler, P.; Ryd, W.; Tornberg, S.; Strand, A.; Wadell, G.; Elfgren, K.; Radberg, T.; Strander, B.; Johansson, B.; Forslund, O.; Hansson, B. G.; Rylander, E.; Dillner, J., Human papillomavirus and Papanicolaou tests to screen for cervical cancer. *N Engl J Med* **2007,** *357*, 1589-97.

119. Mostert, B.; Sleijfer, S.; Foekens, J. A.; Gratama, J. W., Circulating tumor cells (CTCs): detection methods and their clinical relevance in breast cancer. *Cancer Treat Rev* **2009,** *35*, 463-74.

120. Caraway, N. P.; Katz, R. L., A review on the current state of urine cytology emphasizing the role of fluorescence in situ hybridization as an adjunct to diagnosis. *Cancer Cytopathol 118*, 175-83.

121. Kraemer, P. S.; Sanchez, C. A.; Goodman, G. E.; Jett, J.; Rabinovitch, P. S.; Reid, B. J., Flow cytometric enrichment for respiratory epithelial cells in sputum. *Cytometry A* **2004,** *60*, 1-7.

122. Fenton, K. N.; Richardson, J. D., Diagnosis and management of malignant pleural effusions. *Am J Surg* **1995,** *170*, 69-74.

123. Mitchell, H.; Medley, G., Differences between Papanicolaou smears with correct and incorrect diagnoses. *Cytopathology* **1995,** *6*, 368-75.

124. Renshaw, A. A.; Henry, M. R.; Birdsong, G. G.; Wang, E.; Haja, J.; Hughes, J. H., Cytologic features of squamous cell carcinoma in conventional smears: comparison of cases that performed poorly with those that performed well in the College of American

Pathologists Interlaboratory Comparison Program in cervicovaginal cytology. *Arch Pathol Lab Med* **2005,** *129*, 1097-9.

125. Renshaw, A. A.; Dubray-Benstein, B.; Haja, J.; Hughes, J. H.; Pathologists, C. A., Cytologic features of low-grade squamous intraepithelial lesion in ThinPrep Papanicolaou test slides and conventional smears - Comparison of cases that performed poorly with those that performed well in the College of American Pathologists Interlaboratory Comparison Program in Cervicovaginal Cytology. *Archives of Pathology & Laboratory Medicine* **2005,** *129*, 23-25.

126. Ransdell, J. S.; Davey, D. D.; Zaleski, S., Clinicopathologic correlation of the unsatisfactory Papanicolaou smear. *Cancer* **1997,** *81*, 139-43.

127. Moriarty, A. T.; Clayton, A. C.; Zaleski, S.; Henry, M. R.; Schwartz, M. R.; Eversole, G. M.; Tench, W. D.; Fatheree, L. A.; Souers, R. J.; Wilbur, D. C., Unsatisfactory reporting rates: 2006 practices of participants in the college of american pathologists interlaboratory comparison program in gynecologic cytology. *Arch Pathol Lab Med* **2009,** *133*, 1912-6.

128. Frable, W. J., Error reduction and risk management in cytopathology. *Semin Diagn Pathol* **2007,** *24*, 77-88.

129. Sun, J.; Li, M.; Liu, C.; Zhang, Y.; Liu, D.; Liu, W.; Hu, G.; Jiang, X., Double spiral microchannel for label-free tumor cell separation and enrichment. *Lab on a Chip* **2012,** *12*, 3952-3960.

130. VanDelinder, V.; Groisman, A., Perfusion in Microfluidic Cross-Flow: Separation of White Blood Cells from Whole Blood and Exchange of Medium in a Continuous Flow. *Anal Chem* **2007,** *79*, 2023-2030.

131. Massart, R., Preparation of aqueous magnetic liquids in alkaline and acidic media. *Magnetics, IEEE Transactions on* **1981,** *17*, 1247-1248.

132. Geraldes, C. F. G. C.; Laurent, S., Classification and basic properties of contrast agents for magnetic resonance imaging. *Contrast Media & Molecular Imaging* **2009,** *4*, 1-23.

133. Willard, M. A.; Kurihara, L. K.; Carpenter, E. E.; Calvin, S.; Harris, V. G., Chemically prepared magnetic nanoparticles. *International Materials Reviews* **2004,** *49*, 125-170.

134. Bajaj, A.; Samanta, B.; Yan, H. H.; Jerry, D. J.; Rotello, V. M., Stability, toxicity and differential cellular uptake of protein passivated-Fe3O4 nanoparticles. *Journal of Materials Chemistry* **2009,** *19*, 6328-6331.

135. Pankhurst, Q. A.; Connolly, J.; Jones, S. K.; Dobson, J., Applications of magnetic nanoparticles in biomedicine. *J Phys D Appl Phys* **2003,** *36*, R167-R181.

136. Martínez-Mera, I.; Espinosa-Pesqueira, M. E.; Pérez-Hernández, R.; Arenas-Alatorre, J., Synthesis of magnetite (Fe3O4) nanoparticles without surfactants at room temperature. *Materials Letters* **2007,** *61*, 4447-4451.

137. Sun, S.; Zeng, H.; Robinson, D. B.; Raoux, S.; Rice, P. M.; Wang, S. X.; Li, G., Monodisperse MFe2O4 (M = Fe, Co, Mn) Nanoparticles. *J Am Chem Soc* **2003,** *126*, 273-279.

138. Huang, S.-B.; Wu, M.-H.; Lin, Y.-H.; Hsieh, C.-H.; Yang, C.-L.; Lin, H.-C.; Tseng, C.-P.; Lee, G.-B., High-purity and label-free isolation of circulating tumor cells (CTCs) in a microfluidic platform by using optically-induced-dielectrophoretic (ODEP) force. *Lab on a Chip* **2013,** *13*, 1371-1383.

139. Miltenyi, S.; Muller, W.; Weichel, W.; Radbruch, A., High-Gradient Magnetic Cell-Separation with Macs. *Cytometry* **1990,** *11*, 231-238.

140. Robert, D.; Pamme, N.; Conjeaud, H.; Gazeau, F.; Iles, A.; Wilhelm, C., Cell sorting by endocytotic capacity in a microfluidic magnetophoresis device. *Lab on a Chip* **2011,** *11*, 1902-1910.

141. Lee, C. S.; Lee, H.; Westervelt, R. M., Microelectromagnets for the control of magnetic nanoparticles. *Appl Phys Lett* **2001,** *79*, 3308-3310.

142. Inglis, D. W.; Riehn, R.; Austin, R. H.; Sturm, J. C., Continuous microfluidic immunomagnetic cell separation. *Appl Phys Lett* **2004,** *85*, 5093-5095.

143. Liu, C. X.; Lagae, L.; Borghs, G., Manipulation of magnetic particles on chip by magnetophoretic actuation and dielectrophoretic levitation. *Appl Phys Lett* **2007,** *90*.

144. Yellen, B. B.; Erb, R. M.; Son, H. S.; Hewlin, R.; Shang, H.; Lee, G. U., Traveling wave magnetophoresis for high resolution chip based separations. *Lab on a Chip* **2007,** *7*, 1681-1688.

145. Lee, H.; Liu, Y.; Ham, D.; Westervelt, R. M., Integrated cell manipulation system - CMOS/microfluidic hybrid. *Lab on a Chip* **2007,** *7*, 331-337.

146. Shevkoplyas, S. S.; Siegel, A. C.; Westervelt, R. M.; Prentiss, M. G.; Whitesides, G. M., The force acting on a superparamagnetic bead due to an applied magnetic field. *Lab on a Chip* **2007,** *7*, 1294-1302.

147. Tarn, M. D.; Peyman, S. A.; Robert, D.; Iles, A.; Wilhelm, C.; Pamme, N., The importance of particle type selection and temperature control for on-chip free-flow magnetophoresis. *J Magn Magn Mater* **2009,** *321*, 4115-4122.

148. Mihajlovic, G.; Aledealat, K.; Xiong, P.; Von Molnar, S.; Field, M.; Sullivan, G. J., Magnetic characterization of a single superparamagnetic bead by phase-sensitive micro-Hall magnetometry. *Appl Phys Lett* **2007,** *91*.

149. van Ommering, K.; Nieuwenhuis, J. H.; van IJzendoorn, L. J.; Koopmans, B.; Prins, M. W. J., Confined Brownian motion of individual magnetic nanoparticles on a chip: Characterization of magnetic susceptibility. *Appl Phys Lett* **2006,** *89*.

150. Jing, Y.; Mal, N.; Williams, P. S.; Mayorga, M.; Penn, M. S.; Chalmers, J. J.; Zborowski, M., Quantitative intracellular magnetic nanoparticle uptake measured by live cell magnetophoresis. *Faseb J* **2008,** *22*, 4239-4247.

151. Massart, R., Preparation of Aqueous Magnetic Liquids in Alkaline and Acidic Media. *Ieee T Magn* **1981,** *17*, 1247-1248.

152. Xia, Y. N.; Whitesides, G. M., Soft lithography. *Annu Rev Mater Sci* **1998,** *28*, 153-184.

153. Hahn, Y. K.; Park, J. K., Versatile immunoassays based on isomagnetophoresis. *Lab on a Chip* **2011,** *11*, 2045-2048.

154. Kang, J. H.; Choi, S.; Lee, W.; Park, J. K., Isomagnetophoresis to discriminate subtle difference in magnetic susceptibility. *J Am Chem Soc* **2008,** *130*, 396-+.

155. Krebs, M. D.; Erb, R. M.; Yellen, B. B.; Samanta, B.; Bajaj, A.; Rotello, V. M.; Alsberg, E., Formation of Ordered Cellular Structures in Suspension via Label-Free Negative Magnetophoresis. *Nano letters* **2009,** *9*, 1812-1817.